
**Nanoscale Optical Absorption Spectroscopy by HR-EELS
&
Valence Band Engineering as a Possible Route to Solve p-doping
Problem in ZnO**

A Thesis
Submitted for the Degree of
DOCTOR OF PHILOSOPHY
in the Faculty of Science

by

Dileep Krishnan



**CHEMISTRY AND PHYSICS OF MATERIALS UNIT
INTERNATIONAL CENTRE FOR MATERIALS SCIENCE
JAWAHARLAL NEHRU CENTRE FOR ADVANCED SCIENTIFIC RESEARCH
Bangalore - 560064, INDIA.
JANUARY 2016**

Dedicated to

My Family

DECLARATION

I hereby declare that the thesis entitled “**Nanoscale optical absorption spectroscopy by HR-EELS and valence band engineering as a possible route to solve *p*-doping problem in ZnO**” is an authentic record of research work carried out by me at the Chemistry and Physics of Materials Unit, Jawaharlal Nehru Centre for Advanced Scientific Research, Bangalore, India under the supervision of Professor **Dr. Ranjan Datta** and that it has not been submitted elsewhere for the award of any degree or diploma.

In keeping with the general practice in reporting scientific observations, due acknowledgment has been made whenever the work described is based on the findings of other investigators. Any omission that might have occurred due to oversight or error in judgment is regretted.

Dileep Krishnan

CERTIFICATE

Certified that the work described in this thesis titled “**Nanoscale optical absorption spectroscopy by HR-EELS and valence band engineering as a possible route to solve *p*-doping problem in ZnO**” has been carried out by Mr. **Dileep Krishnan** at the Chemistry and Physics of Materials Unit, Jawaharlal Nehru Centre for Advanced Scientific Research, Bangalore, India under my supervision and that it has not been submitted elsewhere for the award of any degree or diploma.

Dr. Ranjan Datta
(Research Supervisor)

Acknowledgements

I take this opportunity to sincerely thank my research supervisor Dr. Ranjan Datta for his constant motivation, excellent guidance and encouragement throughout my Ph.D. His valuable instructions, comments and suggestions in preparing research manuscripts and for oral and poster presentations at various conferences and for colloquium have helped me immensely. His endless enthusiasm for science and hardworking nature has inspired and motivated me at various times.

I sincerely thank Prof. C. N. R. Rao for creating world class facilities at International Centre for Materials Science (ICMS). I specially thank him for providing aberration corrected transmission electron microscope facility and pulsed laser deposition crystal growth facility at this centre which gave me an excellent opportunity to learn and carry out research using advanced microscopy techniques.

I thank the past and present chairman of Chemistry and Physics of Materials Unit, Prof. G. U. Kulkarni and Prof. S. Balasubramanian for all their invaluable support.

I would like to express my gratitude to Prof. Arunava Gupta for enthusiastic scientific collaborations, inputs and suggestions which helped me immensely in improving the quality of work and providing us high quality epitaxial magnetic spinel oxide thin films that greatly helped my research.

I also thank Prof. Umesh V. Waghmare for collaboration, helping me in performing DFT simulations and generously providing computational facility. Also, I have great gratitude to Dr. Hembram for helping me learn the basics of DFT calculations.

I am grateful to Dr. Sebastian Peter for collaboration, for providing high quality ReS_2 powders and for fruitful discussions. Also, I thank Dr. Ujjal Gautam for collaboration and useful discussions. I thank Dr. K. Biswas for helping me in carrying out experiments.

I would like to specially thank all the fellow student researchers, Dr. S. V. Bhat, Dr. L. S. Panchakarla, Dr. Claudy Dr. Pranab, Dr. Vasu, Dr. Shipra, Dr. Nitesh, Dr. P. Silwal, Dr. N. Pachauri, Dr. M. Kesaria, Dr. S. Shetty, Mr. V. Keerthi, Ms. R. Moumita, Mr. C. Manjeet, Dr. K. K. Nagaraja, Mr. Sumanta S. for collaborating, helping us during various experiments and for their valuable discussions.

I extend my gratitude to Dr. Jay Ghatak, for useful discussions and invaluable assistance during TEM experiments and data analysis. I also would like to thank Dr. Karthick Balasubramanian and Kannan Dhandapani from ICON for assistance during TEM experiments.

I would like to take this opportunity to specially thank all the professors who offered me courses on various subjects, starting from Prof. S. Balasubramanian, Prof. G. U. Kulkarni, Prof. K. S. Narayan, Prof. T. K. Maji, Prof. A. Sundaresan, Prof. S. Easwaramoorthy, Prof. N. Chandrabhas, Prof. N. S. Vidyadhiraja, Prof. S. K. Pati, Prof. U.V. Waghmare and Prof. Shobhana Narasimhan for their excellent teaching and the courses they have offered.

I would like to thank the entire faculty at JNCASR for being a constant source of inspiration with their advanced research. I take this opportunity to thank all my past teachers at school and college level for sharing their knowledge, providing their support and encouragement without which it is impossible for me to be here.

I take this opportunity to thank my past and present labmates, Dr. Loukya, Ms. Sowjanya, Ms. Sireesha, Mr. Devendra, Mr. Rajib Mr. Badri and Ms. Usha for their useful discussions and creating a cheerful environment.

I would like to thank Department of Science and Technology, India for the International Travel Grant to attend 'XV international conference of Electron microscopy' at Krakow, Poland that gave me a new scientific exposure. I also thank the JNCASR centre for providing me JRF/SRF fellowship for carrying out my Ph.D research and also for funding me to attend various national/international conferences.

I extend my gratitude to all the efficient staff at the Library, Academic and Administration sections for their timely help and cooperation.

I acknowledge and thank all my friends from the integrated PhD 2008 batch - Arpan, Pandu, Sharma, Rana, Chidu, Gayatri, Varun and Sudeshna. I also thank all the friends I made in JNCASR while at recreation and sports, Sandeep, Malli, Debabrata and Bhadram, to name a few. I gratefully recall the vernacular leisure I enjoyed with Dr. Reji, Dr. Neenu, Dr. Priya, Selvi, Krishna, Amogh, Navaneeth, Ashar, Vasu, Sonu, Raghu and Dhanya.

I finally acknowledge and thank all my family members for their unconditional love, support and encouragement.

Synopsis

There are two different topics addressed in the present thesis.

Chapter one is divided into two parts. **The first part** introduces high resolution electron energy loss spectroscopy (HR-EELS) with gun monochromator (energy resolution < 0.18 eV) and how it can be exploited to measure optical band gap values and their types at nanoscale from different classes of materials. In principle, the technique can provide information at one atom resolution. High energy electrons transfer both energy and momentum unlike photon and thus yields information on both direct and indirect transitions across the band gap. However, Cherenkov loss was known to restrict the information obtainable, but our work showed how to overcome the difficulty.

The Second part of chapter one introduces the *p*-type doping problem in ZnO and our approach towards solving this through valence band engineering with S alloying at the O site in epitaxial thin film form.

In **chapter two and three** we have successfully used HR-EELS for obtaining optical band gaps and their types at nanoscale from *A*-site cation vacancies, any variation from ideal inverse spinel configuration and the effect of magnetic order on optical band gaps in epitaxial thin films of various magnetic spinel oxide systems, NiFe₂O₄, CoFe₂O₄ and NiCo₂O₄. **Findings:** Optical band gap measurement by HR-EELS along with DFT based cohesive energy calculations show that NiFe₂O₄ is close to ideal inverse spinel structure and partial inversion is observed in CoFe₂O₄. NiCo₂O₄ shows different electrical and magnetic properties depending on the growth temperature. In NiCo₂O₄, band gaps are significantly higher for the magnetically ordered phase as compared to non-magnetic phase. *A*-site cation vacancy regions are found abundantly and they are found to affect local band gap in these systems. In NiCo₂O₄, *A*-site cation vacancies are also responsible for the observation of saturation magnetization values less than the expected value of $2 \mu_B/f. u.$

In **chapter four**, we have extended the technique for MoS₂ and distorted 1T-ReS₂ TMDCs where layer specific optical absorption spectra has been studied and distinction has been made in analyzing the spectra from simple systems like ZnO.

Findings: Twin exciton peaks corresponding to the direct transition at the K-point in the Brillouin zone could be observed as well as indirect to direct cross-over has been observed for monolayer MoS₂. No such transition has been observed in distorted 1T-ReS₂.

Chapter five is our understanding of native point defects in ZnO by HR-EELS. We have used a set of tools, such as core-loss EELS, valence EELS, cathodoluminescence (CL) and compared the experimental results with electronic structure simulation by Wien2k and multiple scattering theory calculation by FEFF software to correctly assign the native point defect responsible for the defect related green luminescence in ZnO.

Findings: We have learnt from our experience that low-loss EELS/optical band gap measurement is a very sensitive and effective tool to identify the types of various point defects and related complexes in ZnO along with the mBJGGA band gap calculation compared to core-loss EELS/ELNES which is the technique of first choice.

Chapter six deals with our approach towards solving the *p*-type doping problem in ZnO through valence band engineering with S alloying at the O site.

Findings: So far we could incorporate 17 at. % S in ZnO as single phase epitaxial thin film which gives a valence band shift of ~0.2 eV. We also found that Ag and Li are not good dopants but *off-stoichiometric* BN_{1+x} is a good dopant for *p*-type conductivity in ZnO.

Chapter seven is conclusions based on present work and future perspective. The future of HREELS is very bright. 9 meV resolution has been recently demonstrated (Krivanek *et al.*, Microscopy **62**, 3 (2013)). With this, not only the very fine features of optical transitions, but also another important aspect of crystal, that is, phonon modes will also be accessible at atomic and near atomic scale. For example single particle specific or a single point/line defect specific vibrational spectroscopy can also be performed. This opens a new avenue to understand the materials at atomic and nanoscale.

Also, BN_{1+x} is found to be a good dopant and gave rise to *p*-conductivity in ZnO. Further work needs to be focused with the combination through valence band engineering along with *off-stoichiometric* BN_{1+x} doping in order to improve the carrier concentration and mobility in order to fabricate any bipolar device.

List of Publications

Publications relevant to the thesis

1. **K. Dileep**, R. Sahu, S. Sarkar, Sebastian C. Peter and R. Datta, Layer specific optical band gap measurement at nanoscale in MoS₂ and ReS₂ van der Waals compounds by high resolution electron energy loss spectroscopy, **manuscript submitted**.
2. **K. Dileep**, B. Loukya, P. Silwal, A. Gupta, and R. Datta, Probing optical band gaps at nanoscale from tetrahedral cation vacancy defects and variation of cation ordering in NiCo₂O₄ epitaxial thin films, **Journal of Physics D: Applied Physics** 47, 405001 (2014).
3. **K. Dileep**, B. Loukya, N. Pachauri, A. Gupta and R. Datta, Probing optical band gaps at nanoscale in NiFe₂O₄ and CoFe₂O₄ epitaxial films by high resolution electron energy loss spectroscopy, **Journal of Applied Physics** 116, 103505 (2014).
4. **K. Dileep**, R. Sahu, K. K. Nagaraja and R. Datta, Crystallographic phase separation and band gap of ZnO_{1-x}S_x (x = 0.1-0.3) alloy thin films grown by pulsed laser deposition, **Journal of Crystal Growth** 402, 124 (2014).
5. **K. Dileep** and R. Datta, Phase separation and electronic structure of ZnS_{0.3}O_{0.7} alloy thin film with and without (Ag, Li) co-doping, **Journal of Alloys and Compounds** 586, 499 (2014).
6. **K. Dileep**, L. S. Panchakarla, K. Balasubramanian, U. V. Waghmare, and R. Datta, Electron energy loss spectroscopy of ZnO nanocrystals with different oxygen vacancy concentrations, **Journal of Applied Physics** 109, 063523 (2011).
7. R. Sahu, H. Gholap, G. Mounika, **K. Dileep**, B. Vishal, S. Ghara, and R. Datta, Stable p-type conductivity in B and N co-doped ZnO epitaxial thin film, **Physica Status Solidi B**, 1–5 (2015)/ DOI 10.1002/pssb.201552625.
8. R. Sahu, **K. Dileep**, D. S. Negi, K. K. Nagaraja, and R. Datta, Ambipolar behavior of Te and its effect on the optical emission of ZnO:Te epitaxial thin film, **Physica Status Solidi (b)** 252, 1743 (2015).

9. R. Sahu, **K. Dileep**, D. S. Negi, K. K. Nagaraja, S. Shetty, and R. Datta, Structural and optical property characterization of epitaxial ZnO:Te thin films grown by pulsed laser deposition, *Journal of Crystal Growth* 410, 69 (2015).

Publications NOT relevant to the thesis

10. B. Loukya, D. S. Negi, **K. Dileep**, N. Pachauri, A. Gupta, and R. Datta, Effect of Bloch wave electron propagation and momentum resolved signal detection on the quantitative and site-specific electron magnetic chiral dichroism of magnetic spinel oxide thin films, *Phys. Rev. B* 91, 134412 (2015).
11. S. R. Lingampalli, **K. Dileep**, R. Datta, and U. K. Gautam, Tuning the oxygen Release Temperature of Metal Peroxides over a Wide Range by Formation of Solid Solutions, *Chemistry of Materials* 26, 2720 (2014).
12. D. S. Negi, A. Roy, B. Loukya, **K. Dileep**, S. Shetty, N. Kumar, P.S. Anil Kumar, Ranjan Datta, Epitaxial Co metal thin film grown by pulsed laser deposition using oxide target, *Journal of Crystal Growth* 394, 112 (2014).
13. R. Sahu, **K. Dileep**, B. Loukya, and Ranjan Datta, Native defects affecting the Li atom distribution tune the optical emission of ZnO:Li epitaxial thin film, *Applied Physics Letters* 104, 051908 (2014).
14. D. S. Negi, B. Loukya, **K. Dileep**, R. Sahu, S. Shetty, N. Kumar, J. Ghatak, N. Pachauri, A. Gupta, and Ranjan Datta, Structural and magnetic characterization of mixed valence Co (II, III)_xZn_{1-x}O epitaxial thin films, *Journal of Magnetism and Magnetic Materials* 354, 39 (2014).
15. D. S. Negi, B. Loukya, **K. Dileep**, R. Sahu, K. K. Nagaraja, N. Kumar, and Ranjan Datta, Robust room temperature ferromagnetism in epitaxial CoO thin film, *Applied Physics Letters* 103, 242407 (2013).
16. D. S. Negi, B. Loukya, **K. Dileep**, M. Kesaria, N. Kumar, Ranjan Datta, Characterization of structure and magnetism in Zn_{1-x}(Co_x/Mn_x)O epitaxial thin films as a function of composition, *Superlattices and Microstructures* 63, 289 (2013).

17. B. Loukya, D. S. Negi, **K. Dileep**, N. Kumar, J. Ghatak, Ranjan Datta, Giant coercivity in ferromagnetic Co doped ZnO single crystal thin film, *Journal of Magnetism and Magnetic Materials* 345, 159 (2013).
18. B. Loukya, P. Sowjanya, **K. Dileep**, R. Shipra, S. Kanuri, L. S. Panchakarla and Ranjan Datta, Controlling structural quality of ZnO thin film on c-plane sapphire during pulsed laser deposition, *Journal of Crystal Growth* 329, 20 (2011).
19. M. Rana, P. K. Patil, M. Chhetri, **K. Dileep**, R. Datta, and U. K. Gautam, Pd-Pt alloys nanowires as support-less electrocatalist with high synergistic enhancement in efficiency for methanol oxidation in acidic medium, *Journal of Colloid and Interface Science* 463, 99 (2016).

Contents

Acknowledgements.....	v
Synopsis.....	vii
List of Publications.....	ix
1 Part I - Optical Absorption Nanoscopy by HR-EELS.....	1
1.1 Electron Energy Loss Spectroscopy (EELS) in a Transmission Electron Microscope.....	2
1.2 High Resolution Electron Energy Loss Spectroscopy Using a Gun Monochromator.....	4
1.3 Importance of Optical Absorption Spectroscopy at Nanoscale Using HR-EELS.....	5
1.4 Experimental Aspects of HR-EELS using gun monochromator.....	8
1.5 Challenges in Band Gap Measurement by HR-EELS – Cherenkov Loss.....	9
1.6 Data Analysis.....	12
1.6.1 Zero Loss Peak Removal.....	12
1.6.2 Kramers-Kronig Analysis.....	13
1.7 Overview of the Thesis Based on Part I.....	14
1 Part II – Valence Band Engineering, A Possible Route to Overcome p-type doping Problem In ZnO.....	17
1.8 Introduction to <i>p</i> -type Doping Problem.....	18
1.9 Epitaxial Thin Film Growth of ZnO on Highly Lattice Mismatched (16%) c-plane Sapphire Substrate.....	21
1.10. Overview of the Thesis Based on Part II.....	23
1.11Bibliography.....	24
2 Probing Optical Bandgaps at Nanoscale in NiFe₂O₄ and CoFe₂O₄ Epitaxial Films by High Resolution Electron Energy Loss Spectroscopy.....	27
2.1 Introduction.....	28
2.2 Experimental Details.....	28
2.3 Computational Details and Results.....	30
2.4 Results of Optical Absorption Spectroscopy at nanoscale in NiFe ₂ O ₄	34
2.5 Results of Optical Absorption Spectroscopy at nanoscale in CoFe ₂ O ₄	36
2.6 Lattice parameters and Energetics.....	36

2.7	Magnetics.....	37
2.8	Conclusions.....	38
2.9	Bibliography.....	38
3	Probing Optical Bandgaps at Nanoscale from Tetrahedral Cation Vacancy Defects and Variation of Cation Ordering in NiCo₂O₄ Epitaxial Thin films.....	41
3.1	Introduction.....	42
3.2	Magnetic and Electric Properties of NiCo ₂ O ₄ Epitaxial Film on MgAl ₂ O ₄ Substrate Grown by PLD.....	43
3.3	Experimental Details.....	43
3.4	Computational Details and Results.....	44
3.5	High Resolution Imaging of NiCo ₂ O ₄	46
3.6	Results of Optical Absorption Spectroscopy at nanoscale in NiCo ₂ O ₄	46
3.7	Origin of Variation in Cation Ordering.....	48
3.8	Influence of A-site Cation Vacancies in Magnetization in This System.....	49
3.9	Co-existence of Two Extreme Classes of Transition Metal Oxide Semiconductor Systems.....	50
3.10	Conclusions.....	51
3.11	Bibliography.....	51
4	Layer Specific Optical Bandgap Measurement at Nanoscale in MoS₂ and ReS₂ van der Waals Compounds by High Resolution Electron Energy Loss Spectroscopy.....	55
4.1	Introduction.....	56
4.2	Experimental Details.....	57
4.3	Theoretical electronic structure and optical property calculation using WIEN2k code.....	59
4.4	High resolution imaging of MoS ₂ and ReS ₂	61
4.5	Layer specific band gap measurement by HREELS.....	62
4.6	Calculated and experimental energy loss functions.....	65
4.7	Conclusions.....	67
4.8	Bibliography.....	67
5	Understanding Native Point Defects in ZnO by HR-EELS.....	69
5.1	Introduction.....	70

5.2	Experimental details.....	71
5.3	Calculation Details.....	71
5.4	Preliminary results based on core-loss EELS/ELNES.....	72
5.5	Accurate assignment of the defect responsible for green luminescence by low-loss EELS..	74
5.6	Conclusions.....	75
5.7	Bibliography.....	75
6	Valence Band Engineering of ZnO by S alloying.....	77
6.1	Introduction.....	78
6.2	Experimental Details.....	79
6.3	Calculation Methods.....	79
6.4	Results and Discussions.....	80
6.5	Conclusions.....	87
6.6	Bibliography.....	88
7	Conclusions and Future Perspectives.....	89
7.1	Future of HR-EELS.....	91
7.2	Preliminary success in <i>p</i> -type doping of ZnO	92
7.3	Summary of the thesis.....	93
7.4	Bibliography.....	94

Chapter 1

Part I

Optical absorption nanoscopy by HR-EELS

The first part in chapter 1 gives a brief introduction on Electron Energy Loss Spectroscopy (EELS) in a Transmission Electron Microscope along with an overview of the thesis on using low-loss EELS on measuring optical band gaps in various materials at nanoscale.

1.1 Electron energy loss spectroscopy (EELS) in a TEM

The interaction between fast electrons and materials in a TEM can be broadly classified into two categories; elastic and inelastic interaction [1-6]. In elastic interaction there is no exchange in energy but only momentum and for inelastic interaction there is both exchange of energy and momentum between the fast electrons and atomic constituents namely, nucleus and surrounding electrons. In EELS, the elastically scattered electrons form a peak of highest intensity known as the ‘zero loss peak’ (ZLP) and the inelastically scattered electrons form a spectrum spanning up to 2000 eV accessible through the spectrometer (figure 1.1 (b)). There are various inelastic interactions possible and we will mostly be concerned with two varieties, first type is the low loss signal within few eVs from the ZLP which gives information on the band gap (figure 1.1 (c)) and their types in the material and the second type, core loss spectra e.g., O K edge (figure 1.1 (d)) which provides information on the density of unoccupied states. The low-loss EELS contains intensity due to excitation of weakly bound outer-shell electrons of the atoms. Core-loss EELS contains transitions from the core level of atoms to the unoccupied levels above the Fermi level (E_F) of the absorbing atom. The spectrum till ~50 eV from any core loss absorption onset is known as electron energy loss near edge structure (ELNES) and the spectra beyond 50 eV is known as electron energy loss extended fine structure (EXELFS). ELNES provides information on the surrounding electronic structure of the absorbing atoms and EXELFS provides information on the bonding environment and co-ordination. Both ELNES and EXELFS has counterpart in X-ray absorption (XAS) based techniques as XANES and EXAFS, respectively routinely performed in a synchrotron. Both the techniques have their own merits and demerits. While XAS provides information mostly from near the surface of the material and energy loss events over a wide energy range can be accessible with brilliant signal; on the other hand, EELS provides information from the bulk of the sample and both energy and momentum are transferred during an inelastic events with uncontenting superior spatial resolution at individual atom. For a detailed description of various atomic absorption processes and associated techniques based on EELS can be found in Ref. 2.

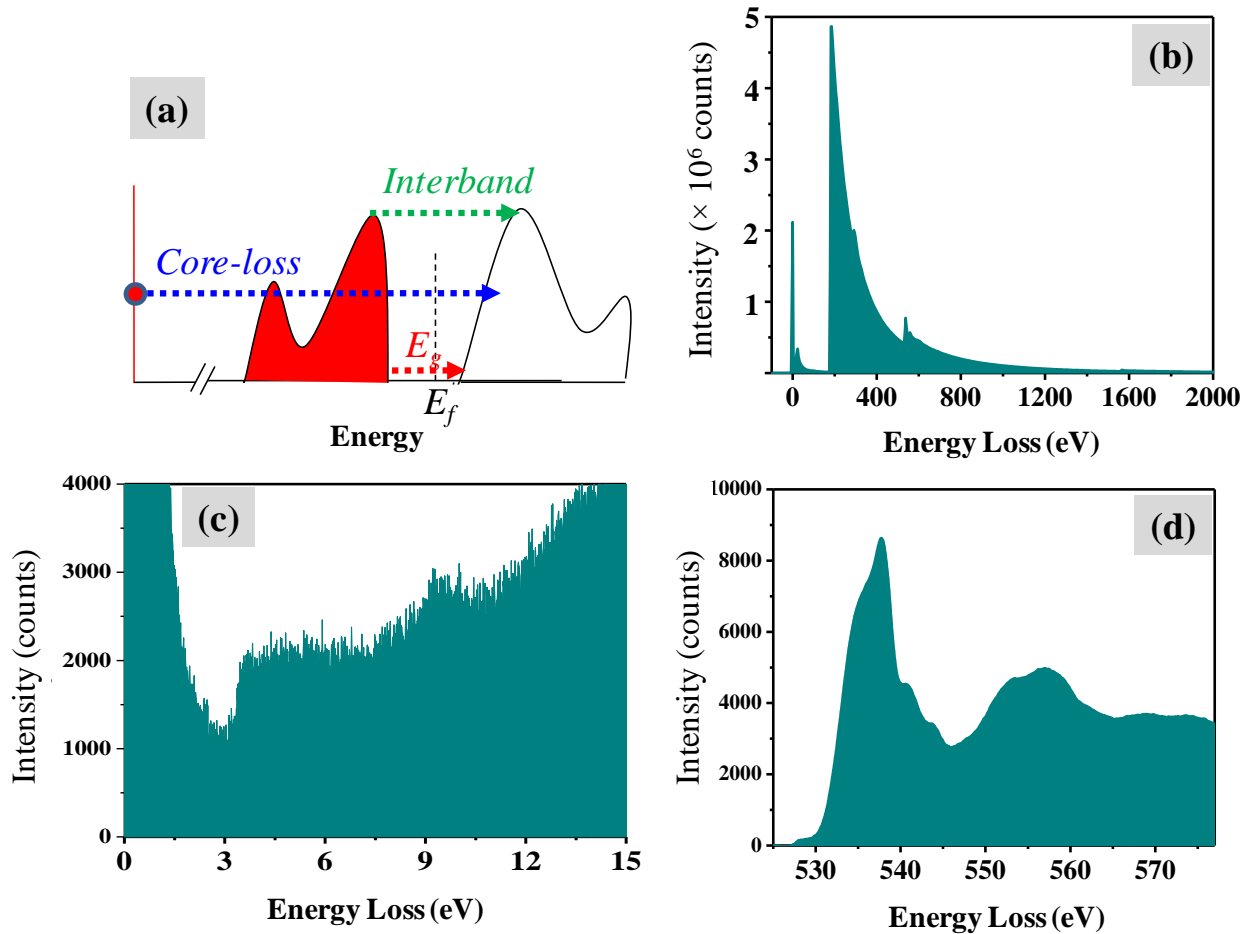


Figure 1.1. (a) Schematic energy level diagram of absorption phenomena in EELS showing various electronic transitions like band gap, interband and core-loss absorption. (b) Spectra displayed till 2000 eV for Al_2O_3 . The intensity is blown up by $\times 350$ times after 178 eV to highlight fine features. (c) EELS in the low-loss region and (d) core loss EELS for O K from ZnO .

However, conventional TEM/EELS provides an energy resolution of ~ 0.7 eV (as measured as the full width at half maxima) with a Schottky field emission gun, which can further be improved to 0.3 eV by using a cold field emission source. This poor energy resolution is not suitable for the low loss signal and fine feature study of the core loss absorption spectra. Therefore, a monochromated electron source is required for the acquisition of spectra with high energy resolution and subsequent extraction and interpretation of the information. Monochromated-EELS is also known as high resolution electron energy loss spectroscopy (HR-EELS).

1.2 High resolution electron energy loss spectroscopy using a gun monochromator

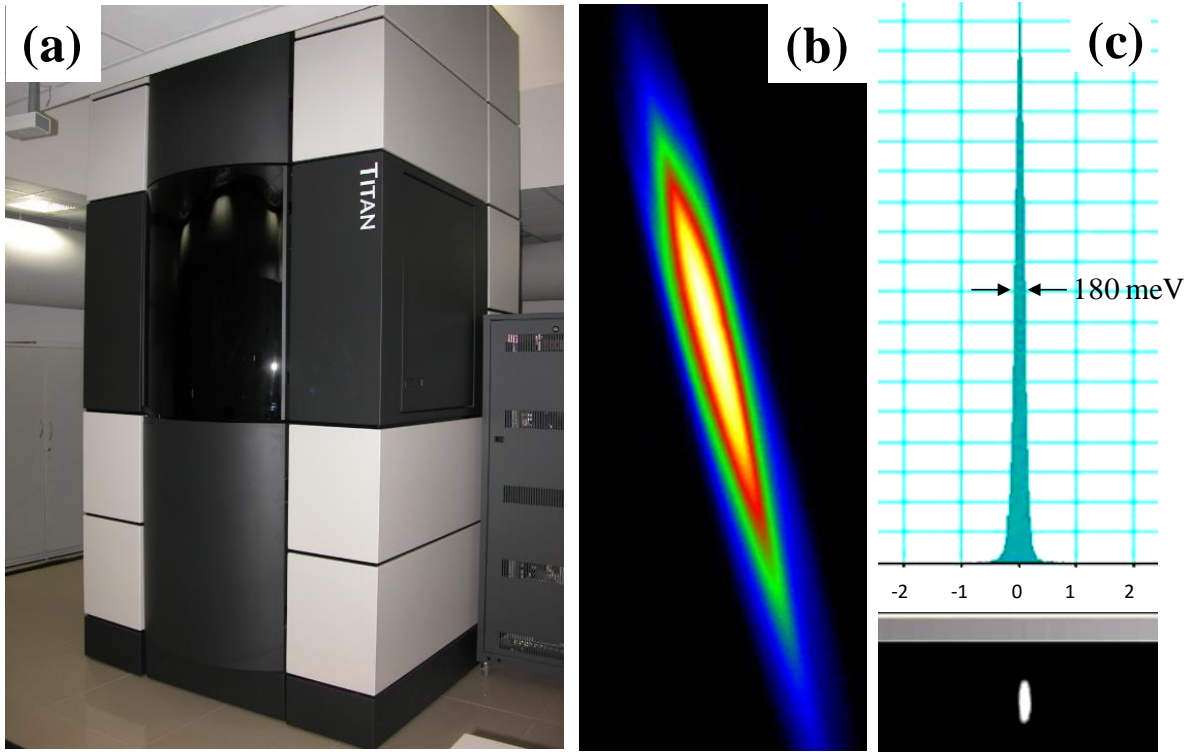


Figure 1.2. (a) FEI TITAN^{3TM} 80-300 kV double aberration corrected transmission electron microscope (b) Monochromated beam after mono-excitation to a value of 1.8. (c) Zero loss peak after monochromatization gives FWHM of 0.18 eV which is a measure of the energy resolution.

FEI TITAN^{3TM} 80-300 kV TEM is equipped with a ‘single Wien filter’ gun monochromator for HR-EELS experiments [7]. Gun monochromator is essential for HR-EELS experiments. A ‘single Wien filter gun monochromator’ essentially acts as a lens that has constant electric and magnetic field perpendicular to each other and perpendicular to the optic axis [7]. Electrons experience both an electric force $= -eE$ (e is the electronic charge; E is the electric field) and a magnetic force $= -evB$ (v is the velocity of electron; B is the magnetic field). Electrons with velocity $v_0 = E/B$ are not deflected while that have velocity higher/lower are deflected either side of the v_0 by the combined E and B so that the central beam with velocity v_0 have very narrow energy spread. The monochromator disperses the electron beam in a single direction. High electron beam currents and highest resolution can be obtained by intercepting the center of the electron beam through slits for any experimental measurements.

Figure 1.2 (a) shows the double aberration corrected FEI TITAN³™ 80-300 kV transmission electron microscope which is equipped with a Cs corrector, which gives a spatial resolution < 0.8 Å and a gun monochromator system that can give an energy resolution of < 180 meV. Figure 2 (b) shows the electron beam after monochromator excitation to a value of 1.8. The ZLP after monochromatization is shown in figure 2 (c) showing a resolution of 180 meV as measured from the FWHM of the ZLP.

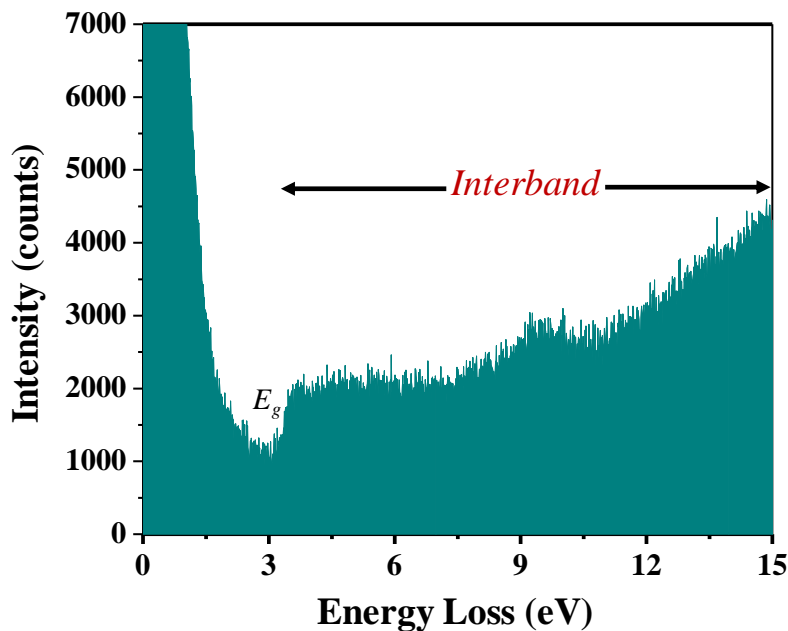


Figure 1.3. Low-loss spectrum of ZnO acquired with a monochromated probe. The band gap onset (E_g) and the features in the spectrum due to interband transitions have been shown.

Figure 1.3 shows an example low loss spectrum of ZnO with a mono-probe. Other than band gap at 3.37 eV, the features due to the interband transitions are also visible. Another important point to be noted is that as the signal is extremely high at low loss regions of the spectra, therefore requires extremely small exposure time typically 1-2 seconds which has added benefit of acquiring spectra without sample damage.

1.3 Importance of optical absorption spectroscopy at nanoscale using HR-EELS

There are two primary motivations which guided us to utilize HR-EELS as nanoscale optical absorption spectroscopy tool. These are described in the two ensuing paragraphs.

In modern information and computing technology, there is a continuous drive for miniaturization of electronic devices, with a particular focus on transistors which is the building block of logic systems [8-10]. One of many possible ways to achieve this is by exploiting two dimensional layered materials e.g., transition metal dichalcogenides (TMDCs) which is considered to be the next generation platform for the development of atomically thin devices [10]. These materials show interesting properties in monolayer form, for example, MoS₂ undergoes indirect to direct band gap crossover from bilayers to monolayer form [11-13]. Traditionally, optical absorption spectra in semiconductors are measured with optical methods which offer a very high energy resolution (~2 meV) but a very poor spatial resolution (~0.2 μm) [14]. However, it is sometimes challenging to synthesize such nano-dimensional material over large sheet area and control the number of layers in order to use such macro scale optical techniques without any cross signals from unwanted areas. Hence, there is a demand for alternative band gap measurement techniques at nanoscale with both high spatial and energy resolution. Electrons have the advantage over photons in terms of transfer of both energy and momentum simultaneously to the crystal electrons thus yields valuable information on the optical properties of the materials. One more advantage is that one can observe and choose an area for such measurement and cross signal can completely be avoided. With the development of electron monochromators, low-loss EELS has now become a powerful tool for measuring optical absorption spectra at nano and atomic scale. In chapter 4, layer specific optical absorption spectroscopy has been performed in two important TMDC, MoS₂ and ReS₂. The technique can be extended to obtain such information due to edges, defects from such materials with high precisions.

The second motivation is to determine and understand the optical properties due to nano scale domains of A-site cation vacancy defects present in the technologically important magnetic spinel oxide systems e.g., NiFe₂O₄ (NFO), CoFe₂O₄ (CFO) and NiCo₂O₄ (NCO). Previous strain contrast and HRTEM microscopy revealed the dark diffused contrast areas in these oxide systems and these are correlated with the either antiphase domains (APBs) (figure 1.4 and ref. 15) or A-site cation defects (figure 1.5 and ref. 16). In cross sectional sample geometry, one can observe the projection of superimposed lattice from two antiphase domains in the HRTEM image in figure 1.4 (f) along the viewing direction ($\langle 100 \rangle$). The A-site cations are translated to

another A-site by the translation vector $\frac{1}{4}\langle 110 \rangle$ in one of the domains. In projection along $\langle 100 \rangle$ both types of A sites will appear as filled. The A-site cation defects will have influence on the opto-electronic property of such materials and it is important to know how they alter the property. Recently, innovation in growth and choice of substrate helped to overcome the APBs [17] but elimination of A site cation defects remains challenging.

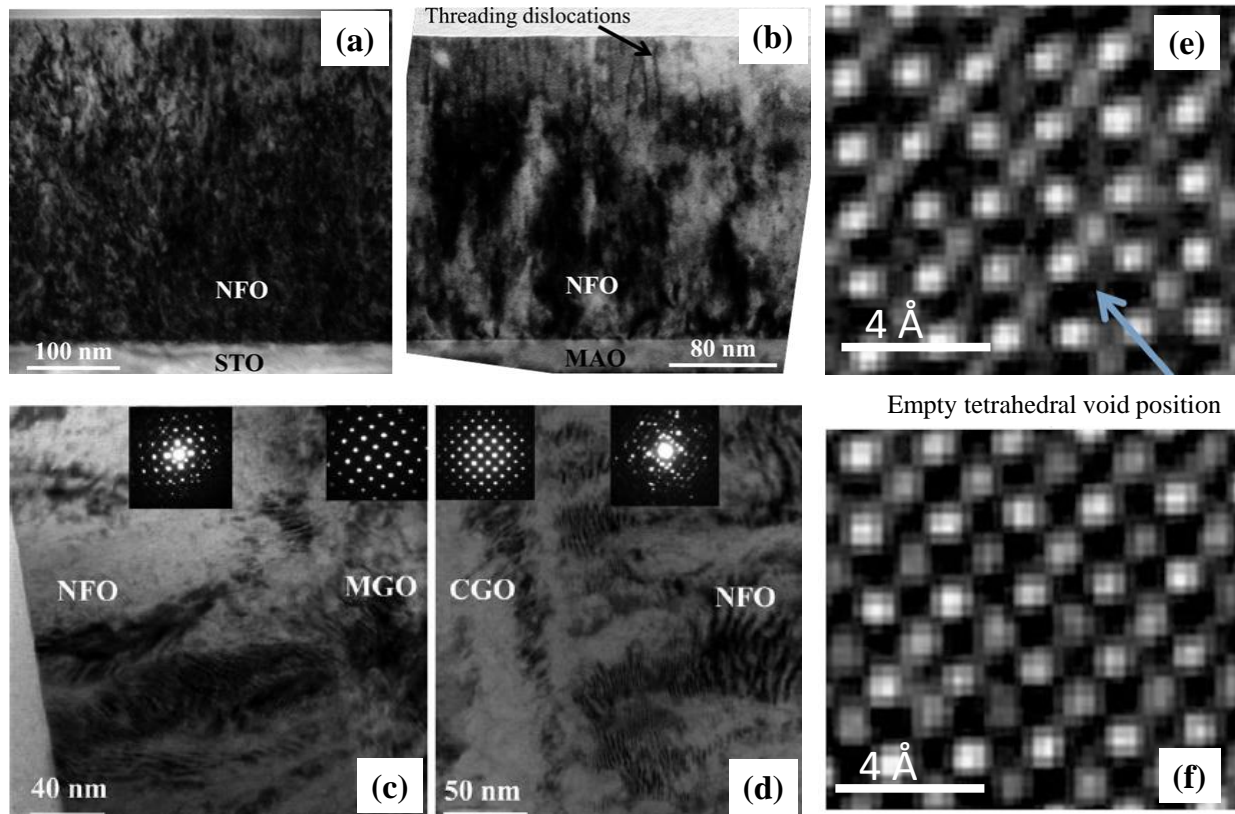


Figure 1.4. TEM x-section diffraction contrast image of NFO on (a) SrTiO_3 (STO – perovskite - lattice mismatch = 6.35%), (b) MgAl_2O_4 (MAO - spinel - lattice mismatch = -3.17%), (c) MgGa_2O_4 (MGO-spinel - lattice mismatch = -0.64) and (d) CoGa_2O_4 (CGO - spinel - lattice mismatch = -0.17%) HRTEM image of NFO with (e) spinel configuration, and (f) projection of superimposed anti-phase domains. Copyright (2010) by American Institute of Physics [15].

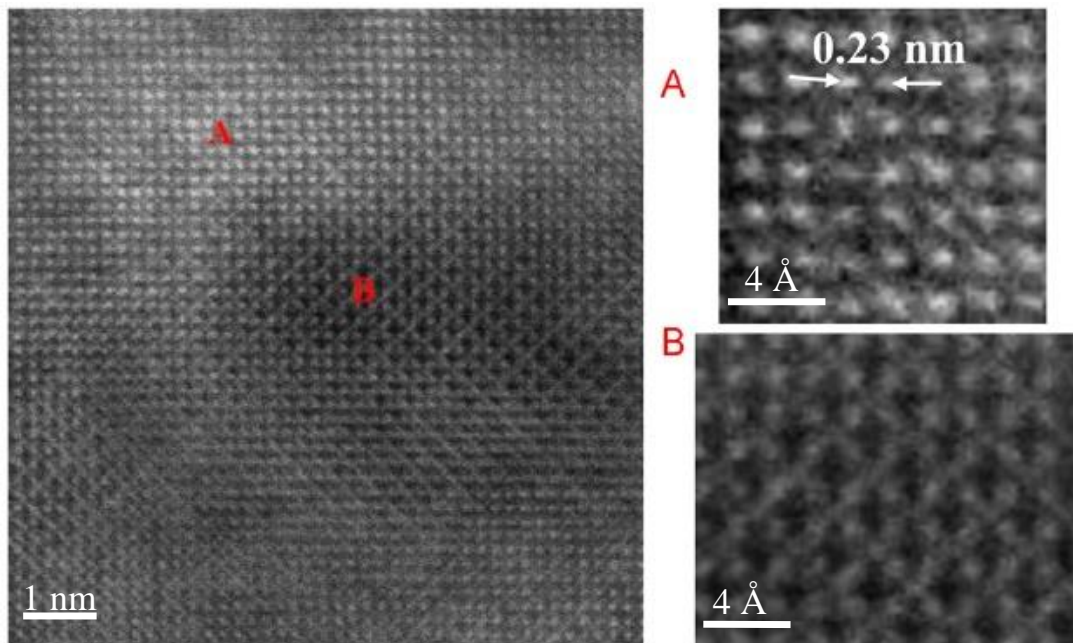


Figure 1.5. STEM-HAADF image of NFO grown on PZN-PT. Two different regions with two different atomic arrangements have been identified and marked as A and B. Copyright (2010) by Elsevier [16].

1.4 Experimental aspects of HR-EELS using gun monochromator

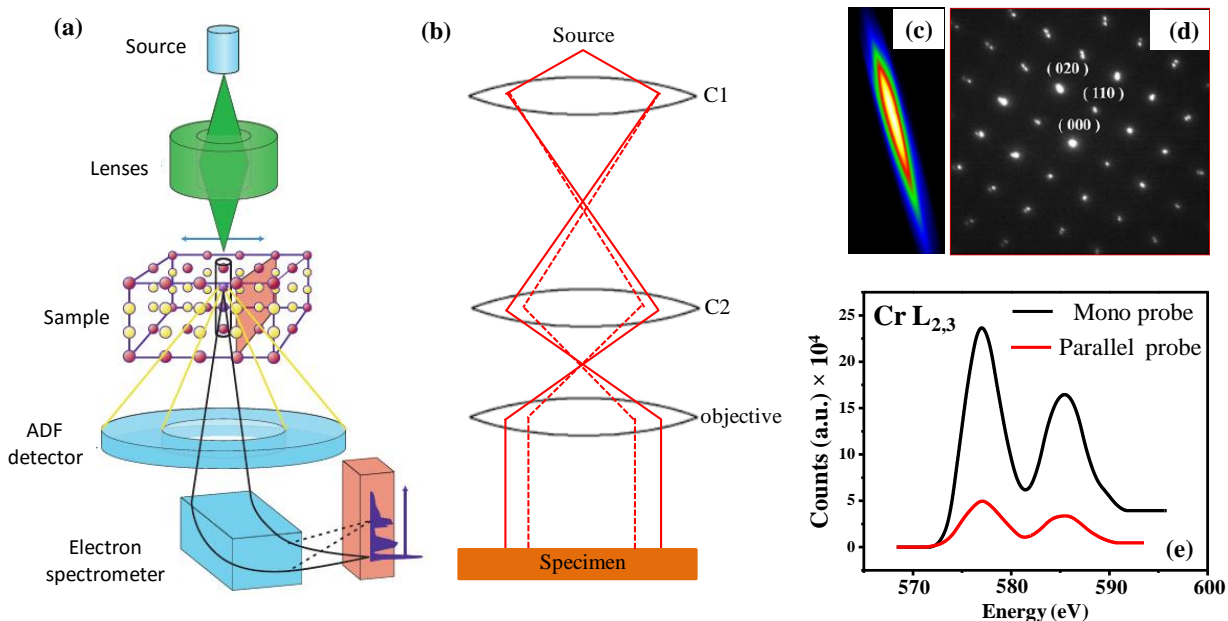


Figure 1.6. Geometry of the HREELS experiment (a) in STEM mode Copyright (2009) by Nature Publishing Group [18], (b) in conventional TEM mode, (c) Mono-probe after excitation is focused below mono-aperture but is found to retain (d) parallel illumination. This results in increase in signal as demonstrated for (e) the Cr $L_{3,2}$ of CrO_2 . Copyright (2012) by Elsevier [19].

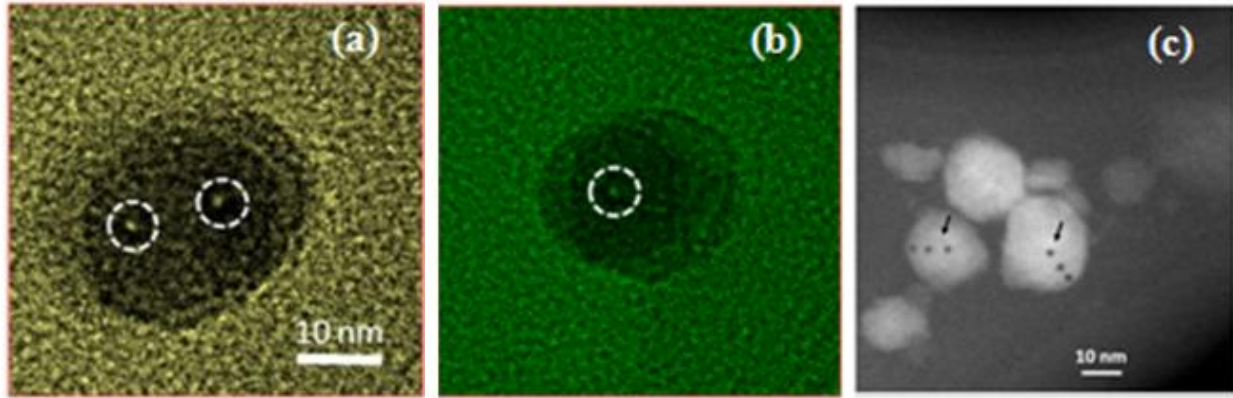


Figure 1.7. (a) & (b) Beam damage under converged probe for a dwell time of less than a minute with spot size 9 in regular TEM mode. The hole formed by the electron probe is marked with white dotted circles. (c) With STEM probe the damage will be more rapid as a result of the higher current density due to stronger beam convergence. The hole regions in the images are marked with white dotted circles. Copyright (2015) by American Institute of Physics [21].

The question is how to perform a HR-EELS experiment at high spatial resolution and with high signal to noise ratio. The obvious choice will be scanning transmission electron microscopy (STEM) in combination with mono-probe. However, it is extremely difficult to employ mono-beam in conjunction with highly converged probe in STEM mode. There are other difficulties. High beam current of the STEM probe risks the possibility of beam damage and contamination (figure 1.7 and ref. 21). Moreover, STEM broadens the Bragg spot which consequently broadens the angular distribution of Cherenkov radiation and subsequent removal of the Cherenkov radiation (see section 1.5) will be almost impossible. Additionally, since STEM yields probe position dependent EELS involving the interaction of the local electronic environment of atomic columns with the probe [20]. This will require new simulation approach and invoking usual periodic approach may not be appropriate [20]. Therefore, we have designed our experiment by utilizing mono-probe, magnification and GIF entrance aperture to obtain nanoscale spatial resolution. Magnification reduces the signal but demagnifying mono-probe on sample plane can compensate this and with this method we now can now achieve one atomic plane spatial resolution without sample damage [21].

1.5 Challenge in band gap measurement using HR-EELS – Cherenkov Losses

The velocity of 300 kV electron is $\sim 0.8 c$ where c is the velocity of light in vacuum. When the velocity of a charged particle exceeds the velocity of light in a medium, the electron

undergoes energy losses in the optical range known as Cherenkov radiation. Generally, Cherenkov losses appear in the optical range and modulate the signal. However, for very thin specimen the Cherenkov intensity will be negligible.

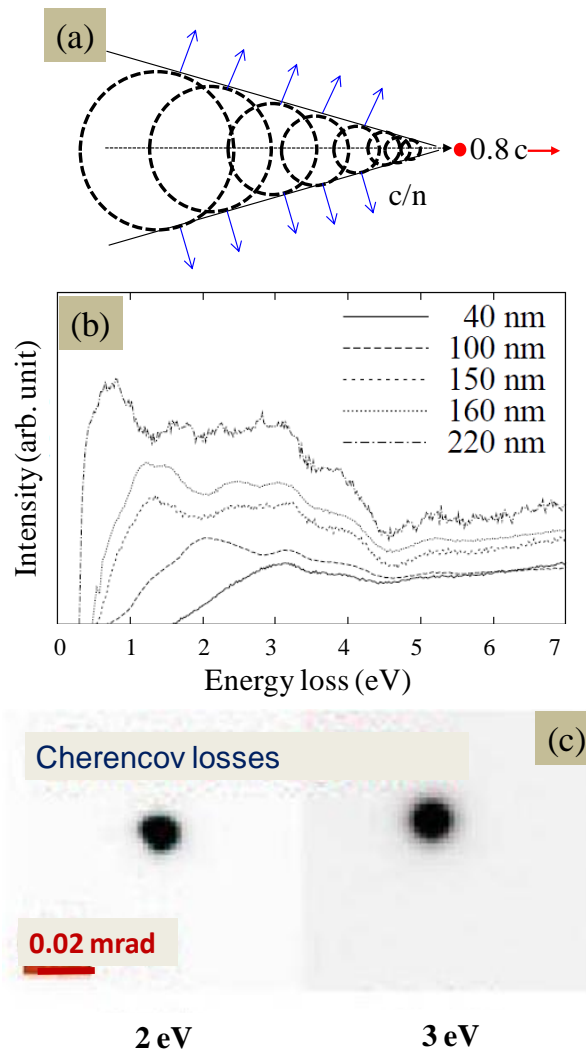


Figure 1. 8. (a) Schematic diagram of generation of Cherenkov radiation in a medium. When a charged particle (electron) travels in the direction shown by red arrow faster than the velocity of light in a medium, Cherenkov radiation is generated along the direction shown by blue arrows, with a velocity $= c/n$, where c is the velocity of light and n is the refractive index of the medium. They are coherent shock-waves generated by the inelastic relaxation of electric dipoles produced by the fast charged particle. (b) Low-loss EELS for Si with a monochromated TEM. The appearance of peaks in the low-loss EELS spectra is due to Cherenkov radiation. Its intensity increases and the onset shifts to lower energies with sample thickness. (c) The energy filtered central diffraction spots for Si which shows that the angular and energy dependence of Cherenkov radiation is $<20\mu\text{rad}$. (Copyright (2006) by Elsevier [24]).

This is because the intensity of Cherenkov radiation is proportional to the thickness [2, 22-24]. Also, the energy onset of the Cherenkov radiation is inversely proportional to the thickness. This can be understood as the coupling of the incident electrons with the guided modes within the sample. Larger the thickness, the sample can support guided modes with larger wavelengths and the onset of the Cherenkov radiation red shifts [22, 23]. So, the direct band gap measurement can be done at sufficiently low thicknesses where the onset of the Cherenkov radiation is beyond the band gap onset. Gu et al. have found that, for hexagonal GaN, band gap could be measured accurately for thickness $< 0.5 \lambda$, where λ is the mean free path of energy loss electron [25]. We have avoided Cherenkov effects by performing measurements at thicknesses $0.2 \lambda < t < 0.4 \lambda$. Indirect band gap transition involves momentum transfer. But, the intensity of Cherenkov radiation is restricted to very low scattering angles ($< 20 \mu\text{rad}$) [26]. So, it is possible to block away signal from very low scattering angles in diffraction plane.

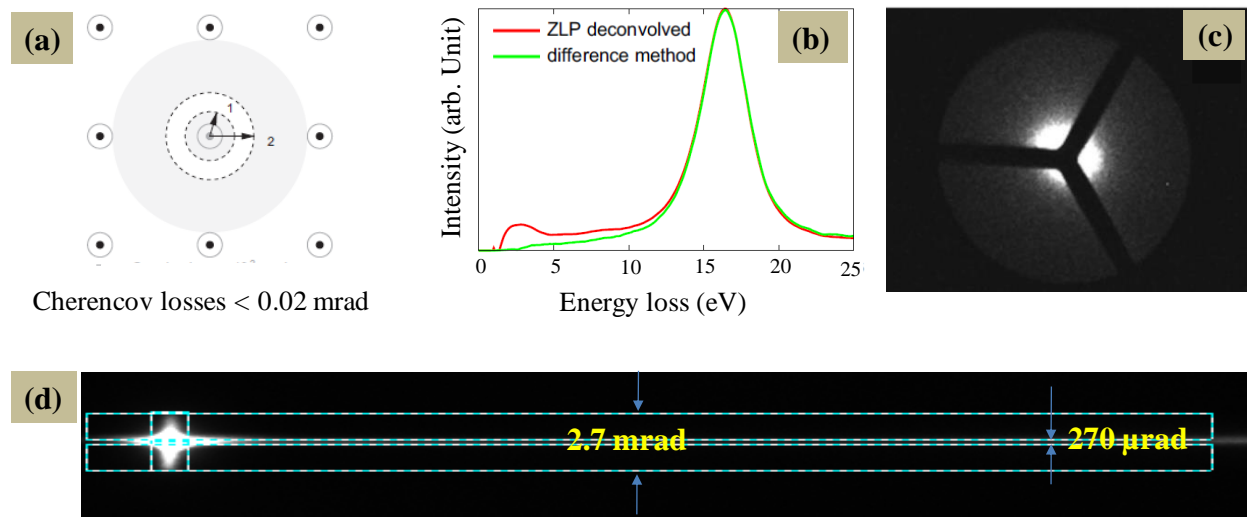


Figure 1.9. (a) Stoger-Pollach's method of removing the contribution of Cherenkov radiation [26] (b) The spectrum before (red curve) and after (green curve) removing Cherenkov radiation by Stoger-Pollach's method. Copyright (2007) by Elsevier [26]. (c) Star shaped aperture proposed by Gu et al. Copyright (2007) by American Physical Society [25] and (d) the post-acquisition removal of Cherenkov proposed by us.

Stoger-pollach et al. have removed Cherenkov radiation by measuring at high collection angle (0.25 mrad) and low collection angle (0.09 mrad) using two different sized objective aperture and subtracting them [26]. Gu et al. used a star shaped GIF entrance aperture to remove the Cherenkov radiation which requires the modification of the instrument [25]. We designed our own method to remove the Cherenkov radiation by digital means. We measured a spectrum

image of the diffraction pattern using GIF camera and removed the low scattering angles post-acquisition in *Digital MicrographTM*. The Cherenkov radiation is confined to low scattering angles ($< 20 \mu\text{rad}$). So we removed the signal from nearly $270 \mu\text{rad}$ from the centre of the diffraction pattern as shown in figure 1.9 (d).

1.6 Data analysis

1.6.1 Zero-loss peak removal

There are several zero-loss peak (ZLP) removal routines in *digital micrographTM* software. We used two of the most commonly used routines in our experiments,

- (a) Reflected Tail method – This is one of the most robust and fast method. Its algorithm essentially removes the ZLP by reflecting the negative side of the zero loss peak to the positive side and subtracting from the total signal.
- (b) Fitted Logarithm Tail method – This is a simple model which fits and extrapolates a logarithmic function to the positive side of zero-loss tail. It is a very versatile and robust method.

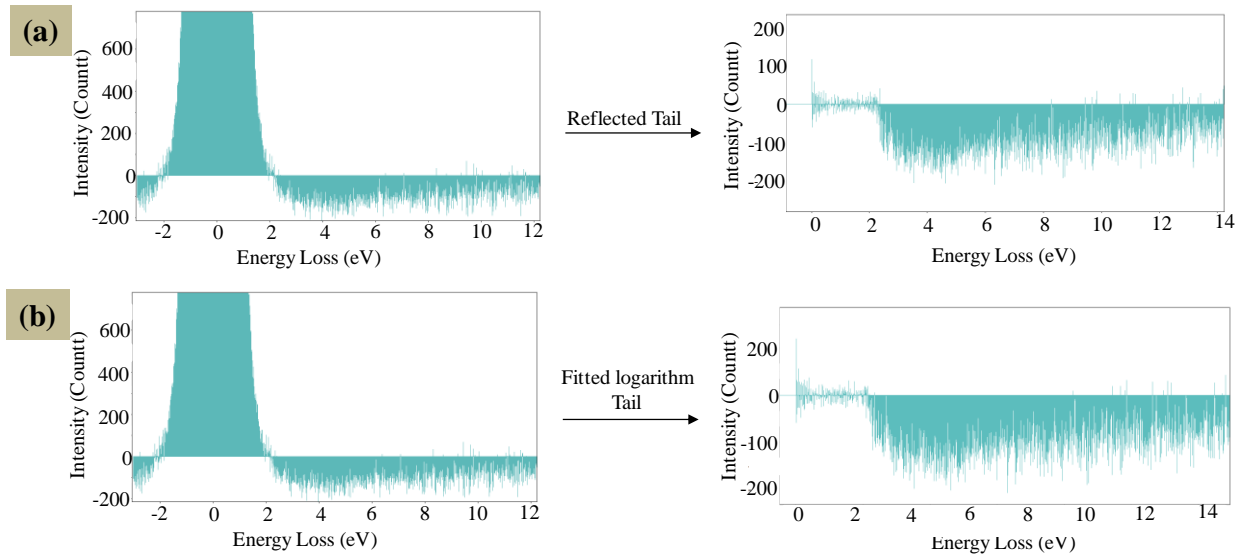


Figure 1.10. Demonstration of zero loss peak removal by (a) reflected tail method and (b) fitted logarithm tail method for spectra collected from vacuum. The spectra show some dark current noise.

As demonstrated in the figure 1.10 (a), with the monochromated beam the tail of the zero loss peak extends only up to 2 eV energy loss and is symmetric about the Y-axis. So, if one is using the reflected tail method he/she has to make sure that the spectrum is acquired to -2 eV or

lesser in the negative side of the ZLP. For logarithm tail method, signal can be obtained by fitting the positive part of the ZLP for a range with an end value lesser than the signal onset.

1.6.2 Kramers-Kronig analysis

Kramers-Kronig analysis is performed to obtain the real (ε_1) and imaginary (ε_2) parts of the dielectric function (ε) from single scattering distribution, which is required for calculating various optical properties such as optical absorption coefficient (α).

For Kramers-Kronig analysis, the following steps are performed,

1. Single scattering distribution is obtained after zero loss removal
2. Single scattering distribution ($S(E)$) is related to the energy loss function (ELF)

$\left(\text{Im} \left[\frac{-1}{\varepsilon(E)} \right] \right)$ by the following equation.

$$S(E) = K \text{Im} \left[\frac{-1}{\varepsilon(E)} \right] \ln \left[1 + \frac{\beta^2}{\theta_E^2} \right]$$

Where K is a proportionality constant and β and θ_E are the effective collection angle and characteristic scattering angle respectively.

3. $\text{Re} \left[\frac{1}{\varepsilon(E)} \right]$ can be calculated from $\text{Im} \left[\frac{-1}{\varepsilon(E)} \right]$ Kramers-Kronig transformation

$$\text{Re} \left[\frac{1}{\varepsilon(E)} \right] = 1 - \frac{2}{\pi} P \int_0^{\infty} \text{Im} \left[\frac{-1}{\varepsilon(E')} \right] \frac{E dE'^2}{E'^2 - E^2}$$

Where P is *Cauchy principal value*

4. From $\text{Im} (-1/\varepsilon)$ and $\text{Re} (1/\varepsilon)$, the real (ε_1) and imaginary (ε_2) parts of the dielectric function can be calculated,

$$\varepsilon(E) = \varepsilon_1(E) + i\varepsilon_2(E) = \frac{\text{Re} \left[\frac{1}{\varepsilon(E)} \right] + i \text{Im} \left[\frac{-1}{\varepsilon(E)} \right]}{\left\{ \text{Re} \left[\frac{1}{\varepsilon(E)} \right] \right\}^2 + \left\{ \text{Im} \left[\frac{-1}{\varepsilon(E)} \right] \right\}^2}$$

5. The optical absorption coefficient (α) can be calculated from ε_1 and ε_2 .

$$\alpha(E) = \frac{E}{\hbar c} \left[2 \left(\varepsilon_1^2 + \varepsilon_2^2 \right)^{\frac{1}{2}} - 2\varepsilon_1 \right]^{\frac{1}{2}}$$

With the knowledge of α , one can obtain direct and indirect band gaps by Tauc plots [27], where the X intercepts of $(\alpha.E)^2$ gives the direct band gap value and $(\alpha.E)^{0.5}$ gives indirect band gap values [28].

1.7 Overview of the thesis based on part 1

In chapter 2-4, we have used the optical absorption spectroscopy at nanoscale to measure band gaps and their types in different classes of materials such as magnetic spinel oxides, transition metal dichalcogenides etc. To begin with, we performed optical nanoscopy of magnetic spinel oxide of NiFe_2O_4 (NFO) and CoFe_2O_4 (CFO) to measure directly band gap from A site cation defects and any deviation from the inverse spinel configurations which we found the technique is extremely sensitive. NFO shows band gaps due to ideal inverse spinel configuration but CFO showed considerable deviation in the band gap values due to various kinds of departures from the ideal inverse spinel structure. A site cation vacancies are observed in both systems by HRTEM imaging. Direct probing of these regions in both systems shows significantly smaller band gap values. The experimental results are supported by density functional theory based mBJGGA calculated band gap values for the different cation configurations.

We probed the optical band gaps at the nanoscale in epitaxial NiCo_2O_4 (NCO) thin films with different structural order (cation/charge). Nanoscale regions with unoccupied tetrahedral A site cations are observed using high resolution transmission electron microscopy (HRTEM) in all the samples and direct measurement from such areas reveal significantly low band gap values ($< 1\text{eV}$). Experimental values of band gaps have been found to be in agreement with the theoretical mBJGGA calculated band gaps for various cation ordering and consideration of A site cation vacancy defects. Origin of rich variation in cation ordering in this system is also discussed. The observation of total magnetic moment of $< 2 \mu_{\text{B}}/\text{f. u.}$ has been assigned to A site cation defects, which was previously assigned to cation mixing [29].

Subsequently, we moved on to the novel quasi two dimensional transition metal dichalcogenides (TMDCs). Layer specific direct measurement of optical band gaps of two important van der Waals compounds, MoS_2 and ReS_2 are performed at nanoscale by HREELS. For monolayer MoS_2 , the twin exciton peaks at 1.8 and 1.95 eV originating at the K point of the

Brillouin zone have been observed. Indirect to direct band gap crossover is observed which is consistent with previously reported strong photoluminescence from the monolayer MoS₂. For ReS₂ the band gap is direct and a value of 1.52 and 1.42 eV are obtained for the monolayer and multilayers, respectively. The energy loss function is dominated by features due to high density of states at both the valence and conduction band edges and the difference in analyzing band gap with respect to ZnO is highlighted. 1T ReS₂ forms two dimensional chains like superstructure due to the clustering of four Re atoms. The overall results demonstrate the power of HREELS technique as a nanoscale optical absorption spectroscopy tool.

In the chapters 5, we attempted to understand native point defects in ZnO and to address the ‘*p*-type doping problem’ in ZnO. To begin with, we addressed the issue of native defects responsible for the broad green luminescence in ZnO nanoparticles whose intensity reduces when annealed in oxygen atmosphere at high temperature. We have found pre-edge peaks in Zn L_{3,2} in ZnO samples that show green luminescence. FEFF9 based multiple scattering theory calculation shows that oxygen vacancies (V_O), Zn antisites (Zn_O), Schottky defect (V_{Zn} + V_O) type I and Frenkel defect (V_O + O_i) can introduce pre-edge peaks in Zn L_{3,2} in ZnO. Later we found out that band gap measurement by low loss EELS and in combination of band gap calculations using mBJGGA for a particular defect is more sensitive and effective way to assign the secondary emission to a particular defect type. Band gap measurement by EELS and cathodoluminescence (CL) match with the type (direct/indirect) and value predicted for Schottky defect (V_{Zn} + V_O) type I by mBJGGA calculated band gap.

Chapter 1

Part II

Valence band engineering, a possible route to overcome doping asymmetry problem in ZnO

This chapter provides a brief introduction to epitaxial thin film growth of ZnO on highly lattice mismatched sapphire ($\alpha\text{-Al}_2\text{O}_3$) substrate by pulsed laser deposition technique. A brief introduction is also provided to 'p-type doping problem' in ZnO along with one of the approaches towards overcoming the p-type doping issue by Valence band engineering.

1.8 Introduction to *p*-type doping problem

ZnO is a direct and wide band gap semiconductor with a band gap of 3.37 eV [30]. ZnO offers itself a cheaper alternative to the GaN based technology [31]. GaN is the most important semiconductor material after silicon [32]. It has already found application in general lighting; which is important to reduce the greenhouse gas emission, in energy generation, faster (HEMTs) and high temperature and high frequency devices. The size of the lighting industry will amount to ~120 billion by 2020 (www.ledsmagazine.com). If ZnO based technology can be realized then this huge lighting industry can be accessible. However, one of the major obstacles to realize ZnO based bipolar devices is the stable *p*-type conductivity [33]. Several attempts to achieve *p*-conductivity failed and to overcome the problem requires deeper insight on the role of native defects in this system. Our approach towards this problem is primarily understanding and controlling native defects in this system in epitaxial thin film of ZnO and exploring valence band engineering to solve the problem. We have grown our films in epitaxial form so that any success can be translated immediately to device fabrication stage.

This *p*-doping issue in ZnO is also known as ‘doping asymmetry problem’. There are 3 major obstacles identified to *p*-type doping problem in ZnO based on literature and our experience; (1) limited solubility of acceptor dopants and the formation of precipitates, (2) deep acceptor levels which remain unionized in the device operating temperatures and (3) spontaneous formation of compensating native point defects [33]. From our experience we can add to the list one more issue i.e., formation of dopant complexes between substitutional and interstitial species which we will use at the end to distinguish between ‘good dopant’ and ‘bad dopant’.

Figure 1.11 (a) demonstrates schematically the dependence of formation energy of defects as a function of Fermi level (E_F) position. When one is trying to dope *p*-type (n-type) by moving E_F toward the valence band maximum E_{VBM} (conduction band minimum E_{CBM}), the donor (acceptor) defect formation energies become lower leading to spontaneous formation of compensating defects.

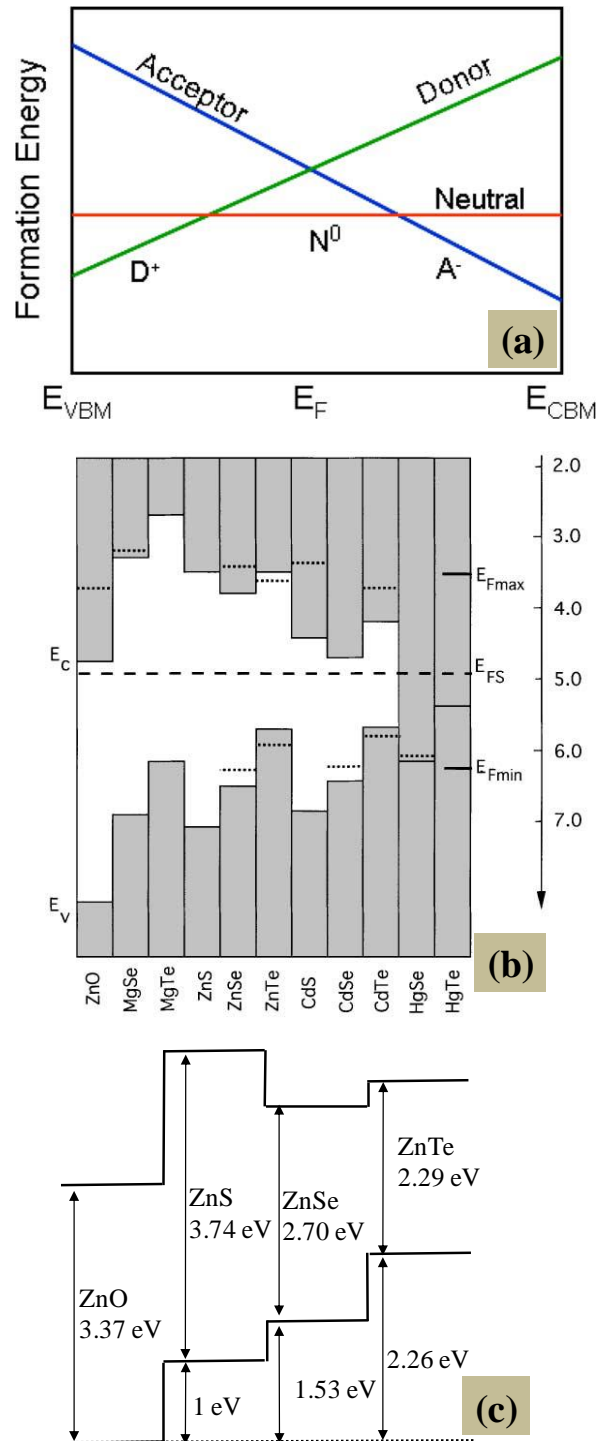


Figure 1.11. (a) Schematic diagram showing the dependence of defect formation energy as function of Fermi level (E_F) position Copyright (2010) by IEEE [33]. (b) Band offsets and the Fermi level stabilization energy, E_{FS} , in II-VI compounds and (d) Band offsets of ZnX (O, S, Se, Te) compounds. Copyright (2010) by Elsevier [34]. The valence band offset progressively shifts toward vacuum level as O is replaced with S, Se and Te [35].

Walukiewicz with his ‘amphoteric defect model’ has argued that for sufficiently high defect density (when the properties of materials are fully controlled by native point defects), Fermi energy becomes ‘stabilized’ to a level called as ‘Fermi level stabilization energy’ (E_{FS}) and becomes insensitive to any further damage [34]. An undoped material with high defect density will have E_F pinned to E_{FS} . When acceptor (donor) impurities are introduced, donor (acceptor) intrinsic defects are spontaneously formed resulting in shift of E_F back towards E_{FS} because of the amphoteric nature of these defects. Amphoteric means defects can reversibly transform between acceptor and donor type depending on Fermi level position. Figure 1.11 (b) shows the schematic energy band offsets with respect to E_{FS} for various II-VI semiconductors. The dotted lines represent position of the Fermi energy corresponding to the highest electron/hole concentration reported in these materials.

As one can see in figure 1.11 (b), ZnO has its E_{VBM} deep down in the energy compared to E_{FS} . This very low value of E_{VBM} is because of the high electronegativity of O atom which makes p -type doping extremely difficult in ZnO. This is why O. Maksimov in his review came up with the idea of improving the p -type dopability through anion substitution with less electronegative group VI elements such as S, Se and Te [35]. This will shift valence band higher in energy and brings E_{VBM} closer to E_{FS} and also will make deep acceptor levels shallow.

Persson et al. studied the E_{VBM} and E_{CBM} as a function of S content in $ZnO_{1-x}S_x$ both by experiment (by ultraviolet photoemission spectroscopy (UPS) on atomic layer deposition (ALD) grown samples) and by simulations (density functional theory (DFT)) [36]. They found that for $ZnS_{0.28}O_{0.72}$ alloy, the valence band offset is 0.55 eV higher in energy than in un-doped ZnO. So an alloy with a composition of $ZnS_{0.3}O_{0.7}$ may be a suitable candidate to ionize both Li (ionization energy, IE = 0.09 eV) and Ag (IE = 0.4 eV) leading to stable p -type conductivity [37, 38].

The primary aim of our effort related to this topic is to grow a single crystalline, single phase $ZnO_{1-x}S_x$ alloy which will ensure best performance and allow ionization of Ag and Li dopants to realize p -type doping of ZnO on highly lattice mismatched sapphire (~18% for ZnO on c -plane Al_2O_3) [39]. This demands systematic microscopic study of the kinetics of epitaxial

thin film growth of ZnO and its dependence on other growth parameters such as nucleation condition, pressure, temperature etc.

1.9 Epitaxial thin film growth of ZnO on highly lattice mismatched (18%) *c*-plane sapphire substrate

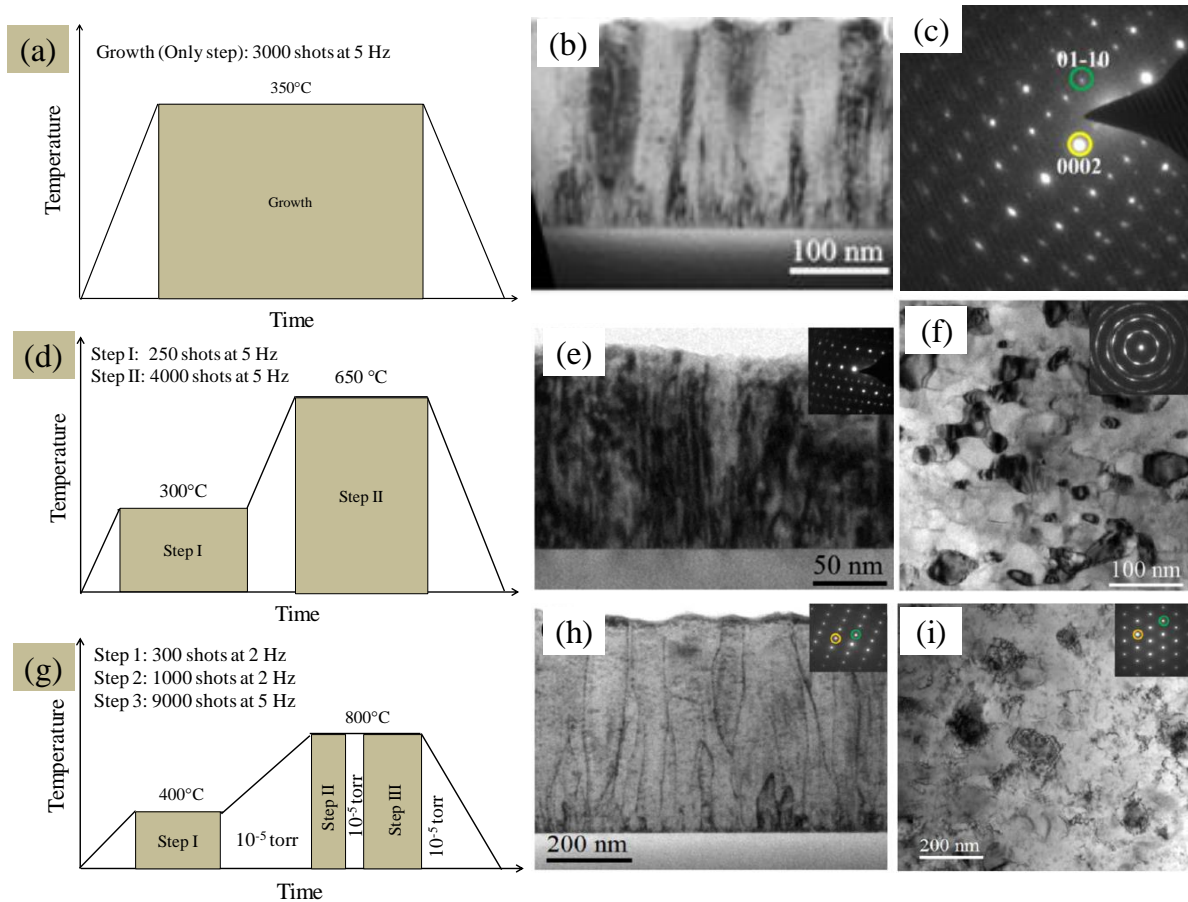


Figure 1.12. Growth scheme for (a) one step, (d) two step and (g) three step growths. (b) TEM cross sectional image and (c) diffraction pattern from sample grown with one step. (e) Cross sectional image and (f) plan view image of two-step grown sample. (h) Cross sectional image and (i) plan view image of two-step grown sample. Copyright (2010) by Elsevier [41].

The *p*-type doping problem in ZnO is similar to the *p*-type doping issue the scientific community faced during the early research and development of GaN. Suji Nakamura, with solely materials science based approach, solved the three major challenges for realizing GaN based technology which were (1) epitaxial thin film growth on highly lattice mismatched substrate, (2) activation of *p*-type dopant and (3) establishing external contacts to the *pn* junction. The first one

was the epitaxial thin film growth of GaN on highly lattice mismatched (16%) sapphire substrate. Based on a *two-step* growth approach he could grow epitaxial thin film of GaN on sapphire using metal organic chemical vapor deposition (MOCVD) [40].

When GaN was grown on sapphire at 1000 °C for 60 minutes, three dimensional island growth was observed [40]. When a *two-step* growth is employed, a nucleation layer of GaN directly on sapphire at 600 °C for 90 seconds ensured complete wetting of the substrate which when followed by annealing and a subsequent growth for 60 minutes at 1000 °C ensured an optically flat and smooth film with mirror-like finish where subsequent growth of active quantum well layers will be effective [40].

Our strategy was to extend the same idea to the growth of ZnO on sapphire by pulsed laser deposition (PLD). PLD system is comparatively faster growth technique than MOCVD. *Our group* systematically studied the effect of various growth parameters such as nucleation layer temperature, nucleation layer growth kinetics, final growth temperature and pressure, number of steps of deposition and annealing duration for depositing high quality epitaxial thin film of ZnO on highly lattice mismatched sapphire substrate [41]. We have found the kinetic control of nucleation/buffer layer is crucial to obtain epitaxial ZnO thin film on ‘c’ plane sapphire without misoriented crystallites. Figure 1.12 (f) shows the presence of misorientated grains if the buffer layer is grown at 5 Hz ablation frequency and the misoriented grains can completely be removed if the buffer layer is grown at 1 Hz ablation frequency (figure 1.12 (h) & (i)). This slower kinetics of buffer layer growth essentially helps establishing epitaxial relationship between ZnO and sapphire almost for the entire contact areas. The details of the growth can be found in ref. 41.

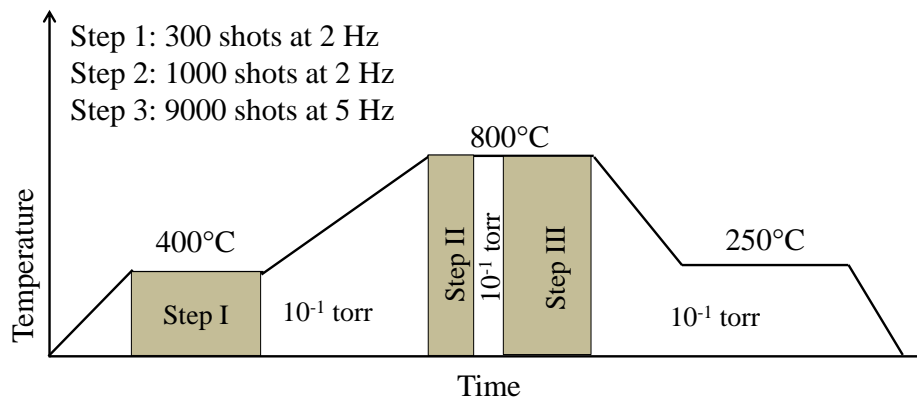


Figure 1.13. Schematic diagram of the resistive type or r-type growth

The three step growth under conditions as mentioned above gave spontaneous *n-type* conductivity with a carrier concentration $\sim 10^{19} \text{ cm}^{-3}$ and a resistivity $\sim 0.3 \text{ } \Omega\cdot\text{cm}$. This growth scheme will henceforth be addressed as *n-type growth*. We have also designed another growth scheme as an extension of the three step growth with extensive annealing in between growth with a scheme as given in figure 1.13. Here, in contrast to the *n-type growth* (see Ref. 41 for details of the growth procedure), the annealing after the first step was increased to 90 minutes (ramp to 800 °C in 50 minutes and stay at 800 °C for 40 minutes) in $\sim 7 \times 10^{-1}$ Torr of O₂ atmosphere. During the growth a pressure of $\sim 1 \times 10^{-5}$ Torr was maintained. This is very important because if the growth is performed under high O₂ pressure, the crystalline quality deteriorates. After the growth the film was cooled down to 250 °C in $\sim 7 \times 10^{-1}$ Torr in one hour. Also, a post-growth annealing was performed at 250 °C for 90 minutes under the same O₂ pressure before cooling down to room temperature. With this growth scheme, while retaining the crystalline quality, we obtained a carrier concentration of $\sim 10^{16} \text{ cm}^{-3}$ and a resistivity $\sim 3000 \text{ } \Omega\cdot\text{cm}$. This growth scheme will henceforth be addressed as *r-type growth*.

We have used the experience and the success of this work in growing high quality epitaxial, single crystalline Ag and Li doped ZnO_{1-x}S_x thin films described in chapter 6.

1.10 Overview of the thesis based on part 2

In chapter 6, we systematically studied crystallographic phase separation and optical properties of ZnO_{1-x}S_x ($x = 0.1-0.3$) alloy thin films grown by pulsed laser deposition (PLD) on *c*-plane sapphire substrate with and without using ZnO buffer layer between the film and substrate. We chose ZnO_{1-x}S_x ($x = 0.1-0.3$) alloy system as a possible candidate for valence and engineering to facilitate *p*-type carriers in ZnO. ZnO buffer layer assists in lattice matching of the alloy thin film and influences the phase separation and incorporation of S in this system. ZnO_{0.7}S_{0.3} thin film separated into four different phases when directly grown on *c*-plane sapphire compared to two when grown using $\sim 8 \text{ nm}$ thick ZnO buffer layer. ZnO_{0.88}S_{0.12} thin film showed a single phase with tilt between crystallites but forms epitaxial film without any tilt on ZnO buffer layer. Incorporation of S is closer to the targeted value for the films grown with the buffer layer. With the help of buffer layer we have been able to grow epitaxial film up to 17 at.% S. Band gap for each alloy phase has been determined by low loss electron energy loss

spectroscopy and a band bowing parameter of ~ 5 eV is obtained. The Ag and Li dopants are incorporated both in the interstitial and substitutional positions forming donor-acceptor complexes, rendering Ag and Li not ‘good dopants’ for obtaining stable *p*-type conductivity in ZnO.

1.11 Bibliography

- [1] D. B. Williams and C. B. Carter, Transmission Electron Microscopy; A Text Book for Materials Science, (Springer Science + Business Media LLC, 2009).
- [2] R. F. Egerton, Electron Energy Loss Spectroscopy in the Electron Microscope, (2nd edn. Plenum, New York, 1996).
- [3] P.W. Hawkes and J.C. Spence, Science of Microscopy, (Springer Science + Business Media LLC, 2007).
- [4] S. J. Pennycook and P. D. Nellist, Scanning Transmission Electron Microscopy (Springer Science + Business Media LLC, 2011).
- [5] R. Brydson, Electron Energy Loss Spectroscopy (Garland Science, first edition, 2001).
- [6] R. Brydson, Aberration Corrected Analytical Transmission Electron Microscopy, (John Wiley & Sons, Ltd., 2011).
- [7] P. C. Tiemeijer, J. H. A. van Lin, and A. F. de Jong, *Microsc. Microanal.* **7**, 1130 (2001).
- [8] G. E. Moore, *Electronics*, **38**, 114 (1965).
- [9] D. Jariwala, V. K. Sangwan, L. J. Lauhon, T. J. Marks, and M. C. Hersam, *ACS Nano* **8**,1102 (2014).
- [10] K. S. Novoselov, V. I. Falko, L. Colombo, P. R. Gellert, M. G. Schwab, and K. Kim, *Nature* **490**, 192 (2012).
- [11] H. S. S. R Matte, A Gomathi, A. K Manna, D. J. Late, R. Datta, S. K Pati, and CNR Rao, *Angew. Chem. Int. Ed.* **49**, 4059 (2010).
- [12] K. Mak, C. Lee, J. Hone, J. Shan, and T. F. Heinz, *Phys. Rev. Lett.* **105**, 136805 (2010).
- [13] A. Splendiani, L. Sun, Y. Zhang, T. Li, J. Kim, C-Y Chim, G. Galli, and F. Wang, *Nano Lett.* **10**, 1271(2010).
- [14] L. H. G. Tizei, Y-C. Lin, M. Mukai, H. Sawada, A-Y Lu, L-J Li, K. Kimoto, and K. Suenaga, *Phys. Rev. Lett.* **114**, 107601 (2015).

- [15] R. Datta, S. Kanuri, S. V. Karthik, D. Mazumdar, J. X. Ma and A. Gupta, Appl. Phys. Lett. **97**, 071907 (2010).
- [16] R. Datta, B. Loukya, N. Li and A. Gupta, J. Crys. Growth **345**, 44 (2012).
- [17] N. Li, Y.H.A. Wang, M.N. Iliev, T.M. Klein, A. Gupta, Chem. Vap. Deposition **17**, 261 (2011).
- [18] D. A. Muller, Nature Mat. **8**, 263 (2009).
- [19] B. Loukya, X. Zhang, A. Gupta, and R. Datta, J. Magn. Magn. Mater. **324**, 3754 (2012).
- [20] M. P. Prange, M. P. Oxley, M. Varela, S. J. Pennycook, and S. T. Pantelides, Phys. Rev. Lett. **109**, 246101 (2012).
- [21] D. S. Negi, B. Loukya, K. Ramasamy, A. Gupta, and R. Datta, Appl. Phys. Lett. **106**, 182402 (2015).
- [22] A. Yurtsever, M. Couillard, and David A. Muller, Phys. Rev. Lett. **100**, 217402 (2008).
- [23] E. Kroger, Z. Phys. **216**, 115 (1968).
- [24] M. Stoger-Pollach, H. Franco, P. Schattschneider, S. Lazar, B. Schaffer, W. Grogger, H.W. Zandbergen, Micron, **37**, 396 (2006).
- [25] L. Gu, V. Srot, W. Sigle, C. Koch, P. van Aken, F. Scholz, S. B. Thapa, C. Kirchner, M. Jetter, and M. Rühle, Phy. Rev. B **75**, 195214 (2007).
- [26] M. Stoger-Pollach and P. Schattschneider, Ultramicroscopy 107, 1178 (2007).
- [27] J. Tauc, Mat. Res. Bulletin **3**, 37 (1968).
- [28] B. S. Holinsworth, D. Mazumdar, H. Sims, Q.-C. Sun, M. K. Yurtisigi, S. K. Sarker, A. Gupta, W. H. Butler, and J. L. Musfeldt, Appl. Phys. Lett. **103**, 082406 (2013).
- [29] P. D. Battle, A. K. Cheetam and J. B. Goodenough Mat. Res. Bull. **14**, 1013 (1979).
- [30] W.W. Wenas, A. Yamada, K. Takahashi, M. Yoshino, M. Konagai, J. Appl. Phys. **70**, 7119 (1991).
- [31] U. Ozgur, Ya.I. Alivov, C. Liu, A. Teke, M.A. Reshchikov, S. Dogan, V. Avrutin, S.J.Cho, H. Morkoc, J. Appl. Phys. **98**, 041301 (2005).
- [32] C. J. Humphreys, MRS Bulletin, **33**, 459 (2008).
- [33] V. Avrutin and H. Morkoc, Proc. IEEE **98**, 1269 (2010).
- [34] W. Walukiewicz, Physica B **302**, 123 (2001).
- [35] O. Maksimov, Rev. Adv. Mater. Sci. **24**, 26 (2010).

-
- [36] C. Persson, C.P. Bjorkman, J. Malmstrom, T. Torndahl, M. Edoff, Phys. Rev. Lett. **97**, 146403 (2006).
- [37] Y. Yan, M.M.A. Jassim, Su-H. Wei, J. Appl. Phys. **89**, 181912 (2006).
- [38] C.H. Park, S.B. Zhang, S. Wei, Phys. Rev. B **66**, 073202 (2002).
- [39] Z. H. Feng, Handbook of Zinc Oxide and Related Materials (CRC Press, Taylor & Francis 2012).
- [40] S. Nakamura, J. J. Appl. Phys. **30**, 1705 (1991).
- [41] B. Loukya, P. Sowjanya, K. Dileep, R. Shipra, S. Kanuri, L. S. Panchakarla, and R. Datta, J. Cryst. Growth **329**, 20 (2011).

Chapter 2

Probing optical band gaps at nanoscale in NiFe_2O_4 and CoFe_2O_4 epitaxial films by high resolution electron energy loss spectroscopy

This chapter presents our results on probing the optical band gaps at the nanoscale in epitaxial NiFe_2O_4 (NFO) and CoFe_2O_4 (CFO) thin films with different structural order (cation/charge) using high resolution electron energy loss spectroscopy (HREELS). Nanoscale regions with unoccupied tetrahedral A site cations are additionally observed. Origin of rich variation in cation ordering in this system is also discussed.

*This work is published in Journal of Applied Physics **116**, 103505 (2014).*

2.1 Introduction

Spinel oxides such as NiFe_2O_4 (NFO) and CoFe_2O_4 (CFO) are being investigated extensively for their potential applications in spintronics [1-12]. These are ferrimagnetic semiconductors with high Curie temperature around 850K and 800K, respectively. They also have very large exchange splitting and tunnel magnetoresistance. So, they are a candidate material for microwave integrated devices, magnetoelectric coupling heterostructures and active barrier material for spin filters. Innovation in large area epitaxial thin film growth technology, particularly direct liquid injection chemical vapor deposition (DLI-CVD), has made it possible to grow these materials with stoichiometric composition and physical properties close to bulk crystals [13]. The stable structure is inverse spinel (space group 216, F-43m), where the unit cell consists of 8 formula units of O sublattice. Out of the 64 tetrahedral (T_d) voids in the unit cell, only 8 are filled and out of the 32 octahedral voids, only 16 are filled. Because of the large open structure the cations have freedom to arrange themselves in different configurations under various growth conditions.

2.2 Experimental details

The NFO and CFO epitaxial thin films investigated were grown on $\langle 100 \rangle$ oriented MgAl_2O_4 (MAO) substrate at 690 °C and 800 °C temperatures, respectively, by direct liquid injection chemical vapor deposition (DLI-CVD) technique developed at the University of Alabama [13]. Transmission electron microscopy (TEM) samples were prepared by mechanical polishing followed by Ar^+ ion milling for perforation to generate large electron transparent thin areas.

Different steps involved in the TEM sample preparation are given in figure 2.1. First step is the face-to-face gluing of films and preparing a sandwich. The assembly is then mounted on a brass block with a temporary mounting wax having melting point of 135 °C. The second step involves mechanical polishing along the cross-sectional direction in order to shape it to fit within the Cu grid of diameter 3 mm and reduce the thickness below 80 μm . Mechanical polishing was done using SiC polishing papers. In the next step, the thickness is further reduced to $< 20 \mu\text{m}$ using diamond polishing sheets of varying grit sizes from 30 to 6 μm . The sample is then mounted on to a copper grid and milled in the precision Ar^+ ion polishing system to perforation.

The beam settings used were $+7^\circ$ and -7° angles for left and right guns with double modulation and with 4 keV of energy. The ion beam energy was reduced to 3 keV in the end to remove any surface amorphous layer.

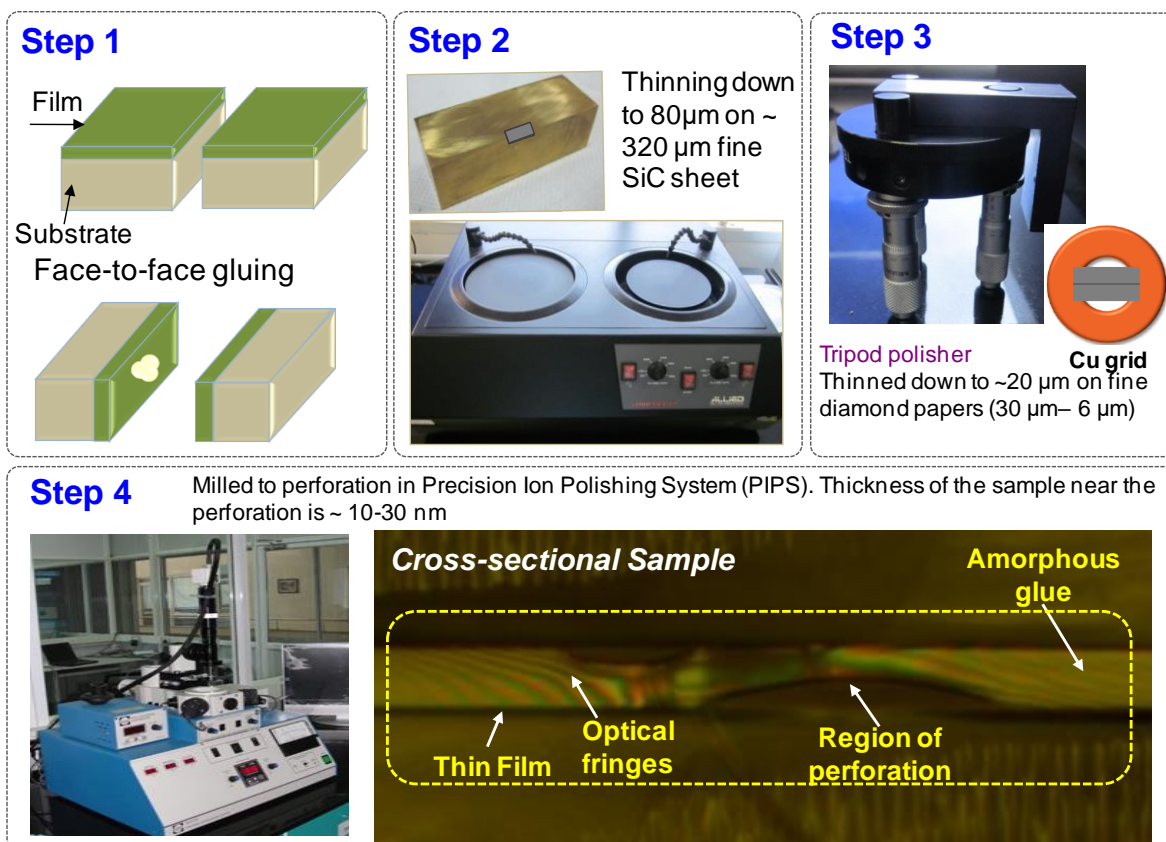


Figure 2.1. Step-by-step procedure for thin film TEM cross-sectional sample preparation. First two steps involve face-to-face gluing and mechanical polishing of the sample to thin down to $80\mu\text{m}$ and in the third step the sample is further thinned down to $<20\mu\text{m}$ using a hand held tripod polisher. In the last step, the sample is mounted on copper grid and milled to perforation in a Gatan Precision Ion Polishing System (PIPS) to obtain an electron transparent thin area.

HRTEM imaging was done in an aberration corrected FEI TITAN 80-300 kV TEM under negative C_s (third order spherical aberration coefficient) $\sim 35\mu\text{m}$ and a positive defocus $\Delta f \sim 8\text{ nm}$ to image atoms with white contrast for direct interpretation. HREELS spectra were collected with a gun monochromator with an energy resolution better than 0.18 eV. The acquisition and spectra analysis are performed as described in sections 1.3 and 1.4. An energy dispersion of 0.01 eV/channel was used with a collection semi-angle of $\sim 2.7\text{ mrad}$, sufficient to include all the

possible indirect transitions. Under these conditions, the site-to-site variation in optical band gaps have been measured from nanoscale regions of the sample.

Computational details and results

Electronic structure calculations are performed using density functional theory (DFT) based WIEN2k code on relaxed 56 atom unit cells of both NFO and CFO. Five different cases of interest for both NFO and CFO are considered. These are (i) inverse spinel, (ii) normal spinel, (iii) 50% normal-inverse spinel mixed/inversed structure, (iv) 50% A site cation vacancy, and (v) 100% A site cation vacancy. The spins of the octahedral ions (spins down or negative moment) are aligned antiferromagnetically to that of the tetrahedral ions (spins up or positive moment) in all the cases. The schematic diagrams of the various structures considered are given in figure 2.2 for NFO and 2.3 for CFO.

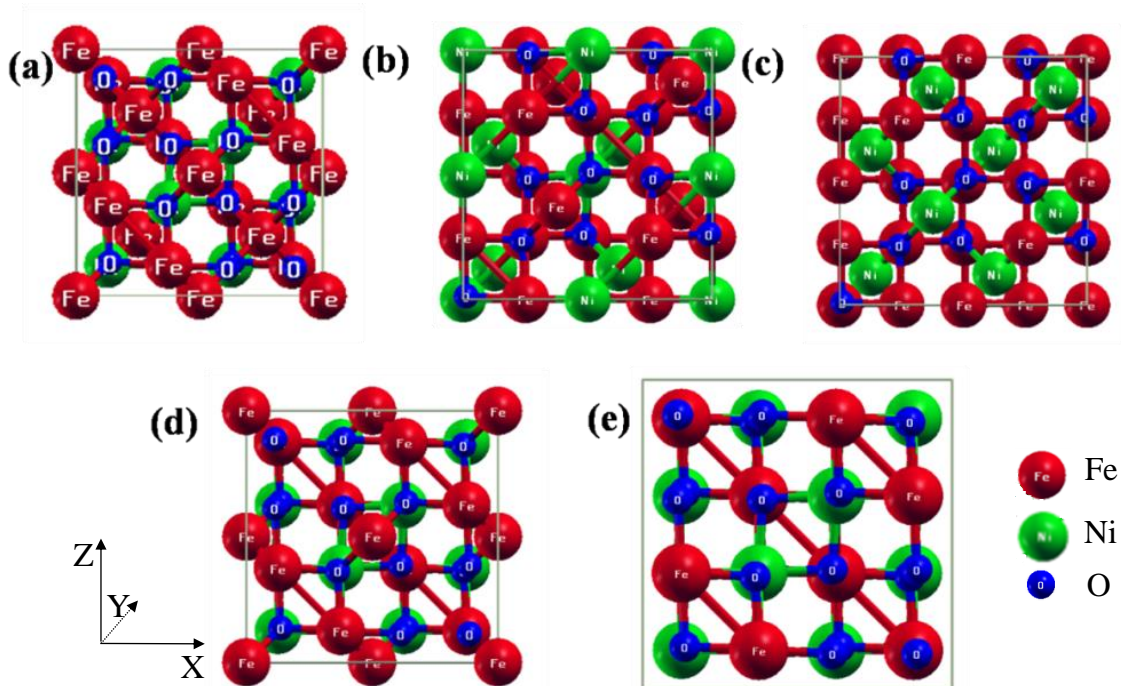


Figure 2.2. Schematics of simulated structures of NFO. (a) Inverse spinel structure, (b) 50% spinel-inverse spinel mixed structure, (c) normal spinel structure, (d) 50% A site cation vacancies and (e) 100% A site cation vacancies. The schematics are shown along $\langle 010 \rangle$. Copyright (2010) by American Institute of Physics [17].

The muffin tin radii (R_{MT}) for the atoms are chosen such that they do not overlap. K_{max} is chosen to be equal to $7.00/R_{MT(min)}$ where $R_{MT(min)}$ is the muffin tin radius of the smallest atom

(oxygen). The core and valence levels are separated by an energy value of -6 Ry. A Γ centered $14 \times 14 \times 14$ k-mesh is used. The lattice parameters are relaxed by GGA-PBE exchange correlation functional with self-consistent field cycles performed until energy and charge values converge to less than 0.0001 Ry and 0.001 electrons, respectively.

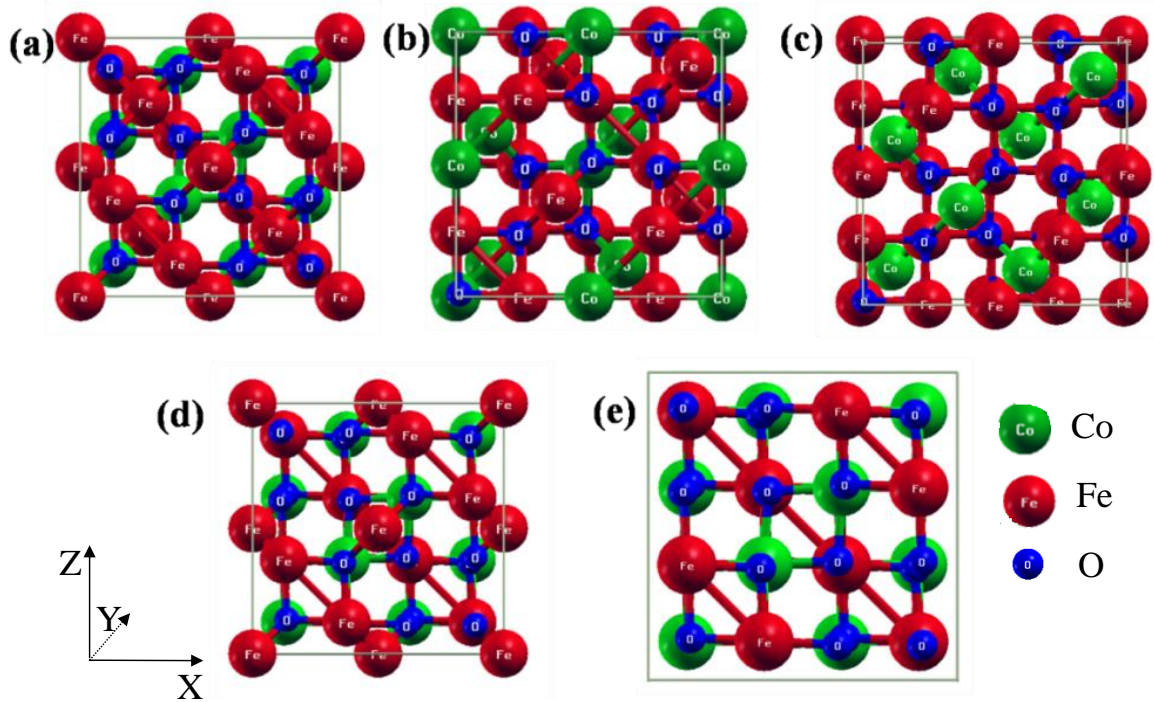


Figure 2.3. Schematics of simulated structures of CFO. (a) Inverse spinel structure, (b) 50% spinel-inverse spinel mixed structure, (c) normal spinel structure, (d) 50% A site cation vacancies and (e) 100% A site cation vacancies. The schematics are shown along $\langle 010 \rangle$. Copyright (2010) by American Institute of Physics [17].

The forces are minimized to values less than 1 mRy/Bohr. The exact excited state properties cannot be calculated using PBE functional, which results in either underestimated band gap values or metallic states for the various cases considered here. Alternatives like HSE or GW calculations are computationally expensive [14]. Another method to predict accurate excited state properties has been proposed by F. Tran and P. Blaha, known as the ‘modified Becke-Johnson’ exchange correlation potential (mBJGGA) [15]. This gives accurate band gap values, comparable to GW calculations, and is computationally economical. We have used this potential for calculation of the band gaps. An appropriate choice of the parameter ‘c’ in this potential is required for the accurate prediction of band gaps. We chose the ‘c’ value according to the ‘P-

semiconductor' scheme and this has already been tested successfully for the transition metal oxides [16].

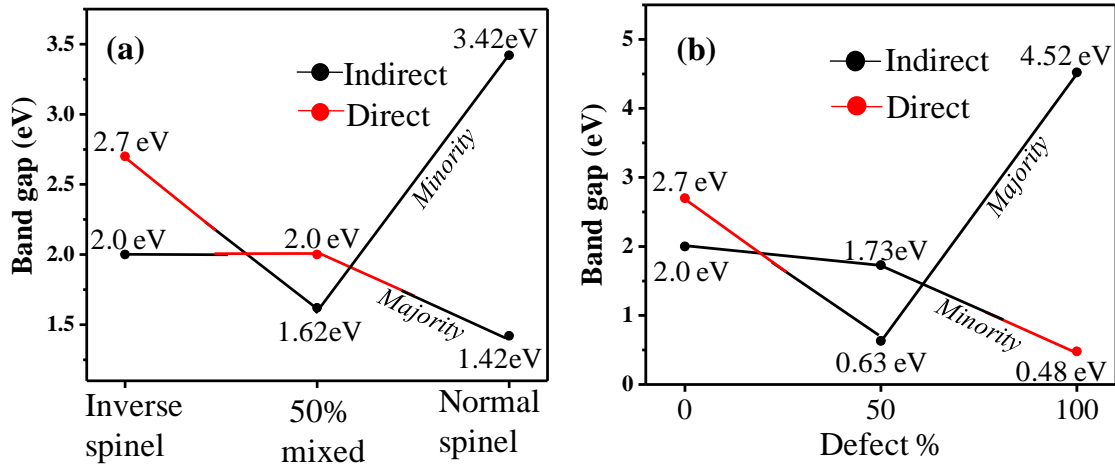


Figure 2.4. mBJ band gaps for NFO as a function of (a) different percentages of cation mixing and (b) different percentages A site cation vacancies. Copyright (2010) by American Institute of Physics [17].

Figure 2.4 summarizes the optical band gap values calculated by mBJLDA potential for the ideal structure, various percentages of cation mixing and A site cation vacancy defect considerations for NFO. The ideal inverse spinel NFO has a fundamental indirect band gap of 2 eV ($X \rightarrow \Gamma$), which is intermediate between the HSE06 and LSDA+ U calculated values reported earlier, [7] and a direct interband transition of 2.1 eV ($X \rightarrow X$) for the minority channel, and a direct band gap of 2.7 eV ($\Gamma \rightarrow \Gamma$) for the majority channel (figure 2.5 (a)).

50% A site cation vacancy introduces defect states in the gap, resulting in low band gap values of 0.63 eV in the majority channel ($\Gamma \rightarrow W$) and 1.73 eV in the minority channel ($\Gamma \rightarrow L$) (Figure 2.5 (b)). This very low band gap value in the majority channel of 50% A site cation vacancy is responsible for the very low band gap observed in experiment.

Figure 2.6 summarizes the mBJLDA calculated optical band gap values for various degrees of cation mixing and defect considerations in CFO. Ideal inverse spinel CFO has a direct band gap of 1.6 eV in the majority channel and an indirect band gap of 0.8 eV in the minority channel. The calculated band gap values through mBJLDA are the same as with GGA+ U , i.e. 1.6 eV, for the direct band gap and LSDA+ U (0.9 eV) for the indirect band gap. The most likely explanation for the experimentally observed higher values in both the direct and indirect band gap for CFO

are partial inversion of the inverse spinel structure (for indirect) and presence of 100% A site cation defects (for direct, see figure 2.6). Therefore, the as-deposited CFO films by DLI-CVD are considered to be in a partially inverted configuration along with presence of A site cation vacancy defects.

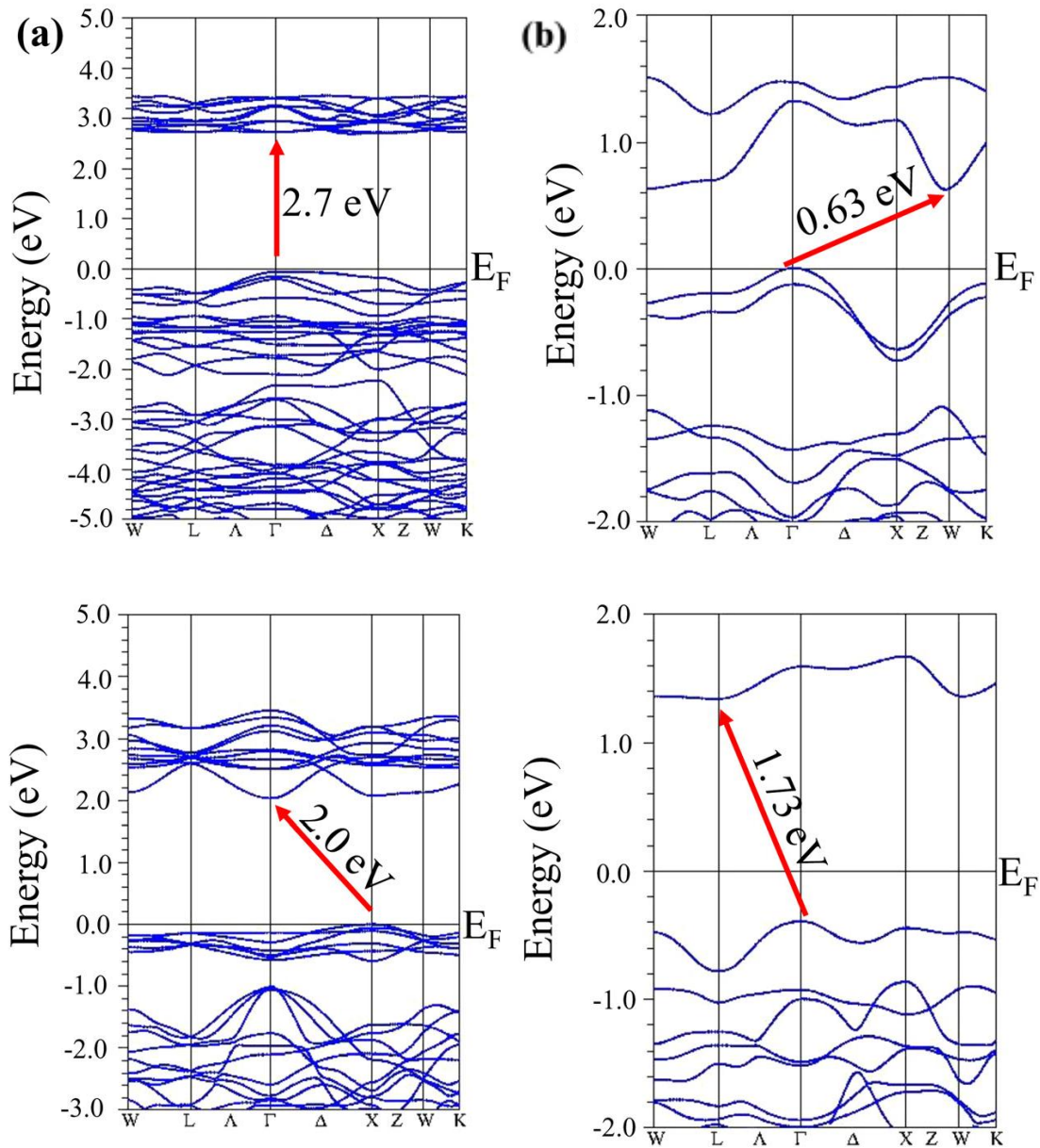


Figure 2.5. Band structures of NFO for majority and minority channels (top and bottom, respectively) show band gap types and values for (a) ferromagnetic structure and (b) 50% A site cation vacancies. Copyright (2010) by American Institute of Physics [17].

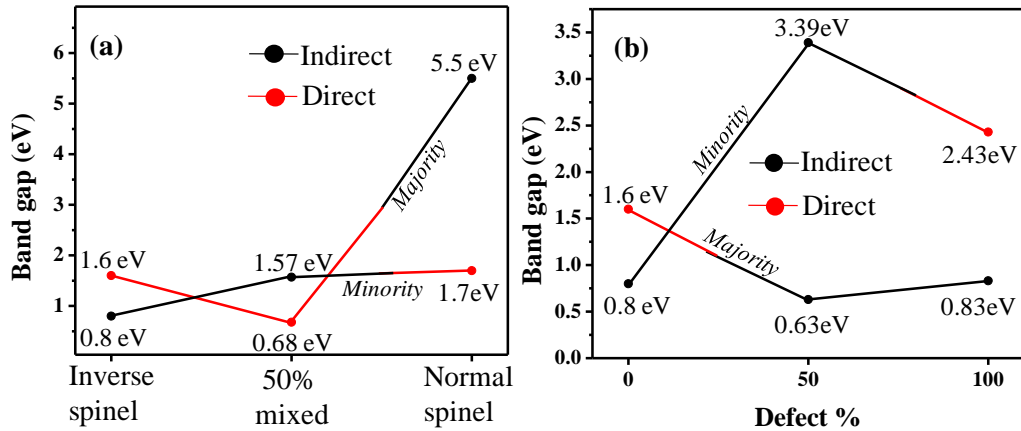


Figure 2.6. mBJ band gaps for CFO as a function of (a) different percentages of cation mixing and (b) different percentages A site cation vacancies. Copyright (2010) by American Institute of Physics [17].

2.3 Results of optical absorption spectroscopy at nanoscale in NiFe₂O₄

Figure 2.7 (a) presents example HRTEM images of NFO and CFO thin films grown on MAO by DLI-CVD method. HRTEM image shows nanoscale regions with ideal lattice arrangement (marked as Y) and A site cation vacancy regions (marked as X). HREELS in a TEM provides the unique opportunity to simultaneously image and acquire optical absorption spectra from A site cation vacancy regions as well as from the regular lattice structure area where any variation in band gap due to inversion from ideal lattice structure can also be acquired. This makes optical absorption spectroscopy at nanoscale by HREELS very important in this class of materials.

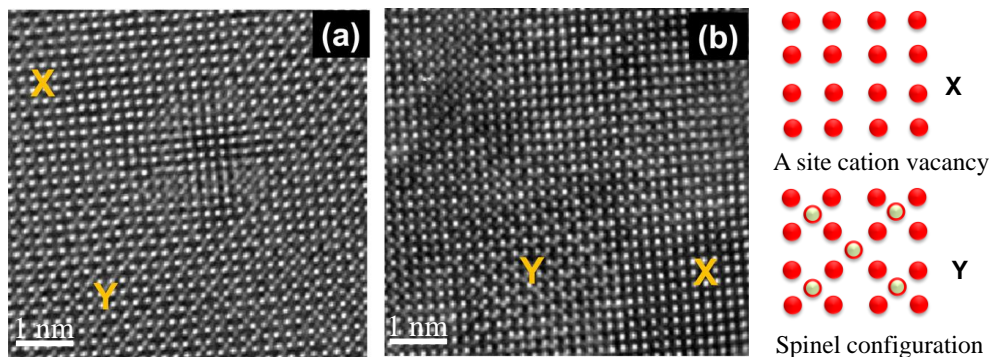


Figure 2.7. HRTEM images showing tetrahedral A site cation vacancy regions (marked with X) along with regular lattice structure (marked with Y) for (a) NFO and (b) CFO along the $\langle 100 \rangle$ Z.A. For regular periodicity, alternate tetrahedral sites are vacant (schematic below (a)) but for A site vacancy regions atoms are missing from the tetrahedral sites (schematic below (b)). Copyright (2010) by American Institute of Physics [17].

Figure 2.7 (a) presents example HRTEM images of NFO and CFO thin films grown on MAO by DLI-CVD method. HRTEM image shows nanoscale regions with ideal lattice arrangement (marked as Y) and A site cation vacancy regions (marked as X). HREELS in a TEM provides the unique opportunity to simultaneously image and acquire optical absorption spectra from A site cation vacancy regions as well as from the regular lattice structure area where any variation in band gap due to inversion from ideal lattice structure can also be acquired. This makes optical absorption spectroscopy at nanoscale by HREELS very important in this class of materials.

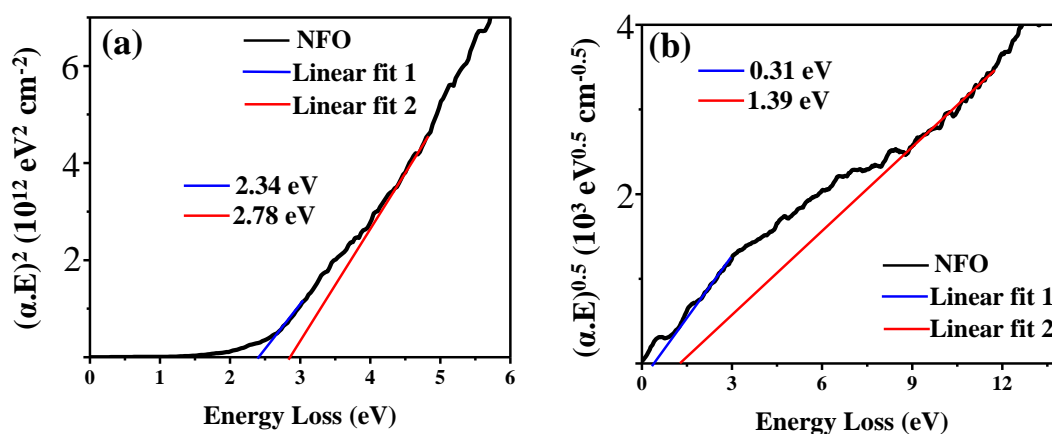


Figure 2.8. Example Tauc plots for (a) direct and (b) indirect band gaps of NFO Copyright (2010) by American Institute of Physics [17].

Figure 2.8 shows example Tauc plots (see section 1.4) for direct and indirect band gaps from NFO. We did not observe any appreciable variation in the experimental band gap values for NFO from different nanoscale regions of the sample by spatially resolved EELS, suggesting close to an ideal inverse spinel configuration. The site-to-site variation in band gap has been measured at nanoscale and the values that have been shown here are in the format ‘mean \pm standard deviation’. The experimental band gap values match closely with the corresponding theoretical calculation and earlier published reports [7]. The two direct band gaps at 2.3 and 2.74 eV and one indirect band gap at 1.52 ± 0.08 eV are due to the ideal inverse spinel structure of NFO (Figure 2.8 (a) and (b)). Musfeldt *et al.* reported two direct band gap of NFO at 2.4 and 2.8 eV (assigned to X \rightarrow X minority and $\Gamma\rightarrow\Gamma$ majority transitions, respectively), and one indirect band gap at 1.6 eV (assigned to X $\rightarrow\Gamma$, minority) from optical transmittance measurements [6]. Our

values are essentially the same as reported by them for both the direct and indirect band gaps. A very low value of the indirect band gaps of 0.46 ± 0.23 eV is recorded from the A site cation vacancy regions.

2.5 Results of optical absorption spectroscopy at nanoscale in CoFe_2O_4

Figure 2.9 shows example Tauc plots for direct and indirect band gaps from CFO. As opposed to NFO, the experimentally measured values of the band gap in the case of CFO are observed to vary significantly from location to location. The direct band gap values range between 2.03 and 2.74 eV, with a mean and standard deviation of 2.31 eV and 0.28 eV respectively (Figure 2.9 (a)). Also, the indirect band gap values vary between 1.08 eV and 1.7 eV, with a mean and standard deviation of 1.39 and 0.31 eV, respectively (Figure 2.9 (b)). The average direct and indirect band gap values of 2.31 eV and 1.3 eV, respectively, are almost the same as those reported by Musfeldt *et al.* based on macroscopic optical absorption measurements [6].

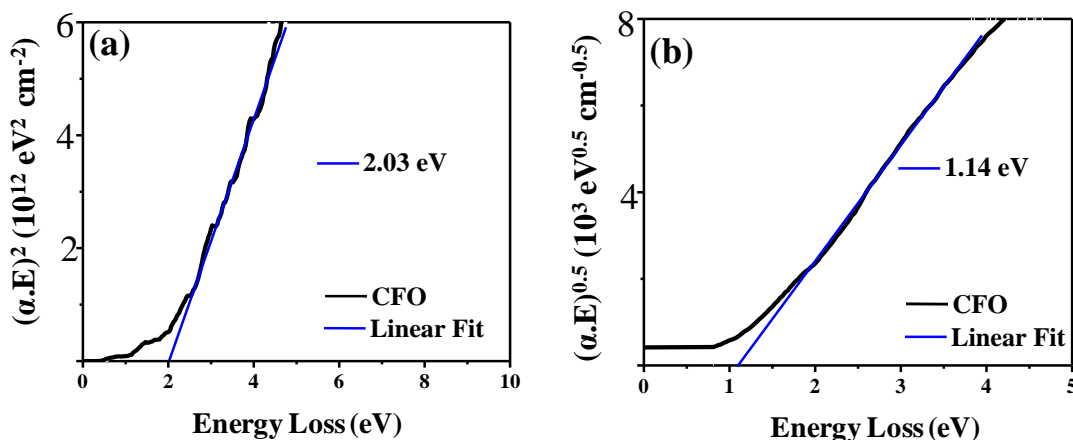


Figure 2.9. Example Tauc plots for (a) direct and (b) indirect band gaps of CFO. Copyright (2010) by American Institute of Physics [17].

2.6 Lattice parameters and energetics

Calculated lattice parameter values and cohesive energies of NFO for the different structural variations are listed Table 2.1. Cohesive energy values indicate the relative thermodynamic stability of the different configurations. For NFO, the most stable structure is found to be the 50% A site cation vacancy with a cohesive energy of 7.3236 eV/atom. Its abundance might be

restricted because of the large lattice parameter mismatch with the MAO substrate. The next most stable structure is the ideal inverse spinel structure with cohesive energy of 6.6355 eV/atom, which is followed by 100% A site cation vacancy, 50% mixed structure and normal spinel structure with cohesive energies of 6.2246, 6.1699 and 6.1294 eV/atom, respectively. The cohesive energy values supports the clear observation of many A site cation deficient regions along with the ideal inverse spinel configuration in the NFO films.

Table 2.1. Lattice parameters and cohesive energy values for NFO and CFO with various structural configurations.

		Inverse spinel	Normal spinel	50% Mixed	50% T _d vacancy	100% T _d vacancy
NiFe₂O₄	a (Å)	8.36	8.18	8.25	8.11	7.97
	Cohesive energy (eV/atom)	6.6355	6.1294	6.1699	7.3236	6.2246
CoFe₂O₄	a (Å)	8.32	8.15	8.21	8.04	7.95
	Cohesive energy (eV/atom)	6.6164	6.5783	6.6137	6.5253	6.3226

In CFO, unlike NFO, the difference in cohesive energy values is marginal between the various configurations, notably between inverse spinel (IS) and 50% mixed (the value is 2.7 meV), IS and spinel (the value is 38.1 meV) and IS-50% T_d defect (the value is 91.1 meV). This suggests that the CFO is much more amenable to structural variations in terms of cation mixing and A site cation defects than NFO. In fact the experimental results indicate significantly more variations in the local experimental band gap values in this system as compared to NFO, likely due to various percentages of A site cation mixing.

2.7 Magnetism

Additionally, the theoretical magnetic moment/formula unit for the different configurations show interesting results and can be very important for spintronic applications. The magnetic moment for individual atoms and the total moment per formula unit for various structural configurations are listed in table 2.2. All the ions show non integral magnetic moments, showing the universal charge mixing in this type of systems. Also, cation mixing in both these systems

results in higher magnetization. When cation mixing occurs Fe atom with a high magnetic moment is introduced into the octahedral channel in exchange for a Ni/Co atom with low magnetic moment resulting in an increase in the net magnetic moment in the octahedral channel. This is surprising as earlier report on high magnetization in NFO in the form of ultra-thin films has been ascribed to the possibility of a normal spinel structure. So, if one can engineer the cation mixing by controlling growth conditions, e.g., temperature, pressure, or the lattice parameter constraints, it may be possible to increase the magnetization of the system. This can be a prospect for the future work.

2.8 Conclusions

In conclusion, we have studied the optical band gap variations at the nanoscale for NFO and CFO films by spatially resolved HREELS and compared the result with first principle based band gap calculations using mBJGGA potential. Additionally, we have made direct measurements of the optical band gap from A site cation deficient regions, which is only possible by EELS technique combined with HRTEM. We find excellent agreement between experimentation and theory. While NFO films primarily display the inverse spinel configuration, CFO is found to be mostly in the partially inverted configuration, which is well supported by first principle calculations.

2.9 Bibliography

- [1] U. Lüders, A. Barthélemy, M. Bibes, K. Bouzehouane, S. Fusil, E. Jacquet, J.-P. Contour, J.-F. Bobo, J. Fontcuberta, and A. Fert, *Adv. Mater.* **18**, 1733 (2006).
- [2] M. G. Chapline and S. X. Wang, *Phys. Rev. B* **74**, 014418 (2006).
- [3] A. V. Ramos, M.-J. Guittet, J.-B. Moussy, R. Mattana, C. Deranlot, F. Petroff, and C. Gatel, *Appl. Phys. Lett.* **91**, 122107 (2007).
- [4] U. Lüders, M. Bibes, J. F. Bobo, M. Cantoni, R. Bertacco, and J. Fontcuberta, *Phys. Rev. B* **71**, 134419 (2005).

- [5] U. Lüders, G. Herranz, M. Bibes, K. Bouzehouane, E. Jacquet, J.-P. Contour, S. Fusil, J.-F. Bobo, J. Fontcuberta, A. Barthélémy, and A. Fert, *J. Appl. Phys.* **99**, 08K301 (2006).
- [6] B. S. Holinsworth, D. Mazumdar, H. Sims, Q.-C. Sun, M. K. Yurtisigi, S. K. Sarker, A. Gupta, W. H. Butler, and J. L. Musfeldt, *Appl. Phys. Lett.* **103**, 082406 (2013).
- [7] Q.-C. Sun, H. Sims, D. Mazumdar, J. X. Ma, B. S. Holinsworth, K. R. O'Neal, G. Kim, W. H. Butler, A. Gupta, J. L. Musfeldt, *Phys. Rev. B* **86**, 205106 (2012).
- [8] N. Li, S. Schafer, R. Datta, T. Mewes, T. M. Klein and A. Gupta, *Appl. Phys. Lett.* **101**, 132409 (2012).
- [9] L. Shen, M. Althammer, N. Pachauri, B. Loukya, Ranjan Datta, M. Iliev, N. Bao, A. Gupta, *J. Crys. Growth* **390**, 61 (2014).
- [10] Y. Chen, J. Snyder, C.R. Schwichtenberg, K.W. Dennis, R.W. McCallum, D. Jiles, *IEEE Trans. Magn.* **35**, 3652 (1999).
- [11] M.J. Carey, S. Maat, P. Rice, R.F.C. Farrow, R.F. Marks, A. Kellock, P. Nguyen, B.A. Gurney, *Appl. Phys. Lett.* **81**, 1044 (2002).
- [12] R.S. Hassan, N. Viart, C. Ulhaq-Bouillet, J. Loison, G. Versini, J. Vola, O. Crégut, G. Pourroy, D. Muller, D. Chateigner, *Thin Solid Films* **515**, 2943 (2007).
- [13] N. Li, Y.H.A. Wang, M.N. Iliev, T.M. Klein, A. Gupta, *Chem. Vap. Deposition* **17**, 261 (2011).
- [14] Arno Schindlmayr, *Phys. Rev. B* **87**, 075104 (2013)
- [15] F. Tran, P. Blaha, *Phys. Rev. Lett.* **102**, 226401 (2009).
- [16] D. Koller, F. Tran, P. Blaha, *Phys. Rev. B* **85**, 155109 (2012).
- [17] K. Dileep, B. Loukya, N. Pachauri, A. Gupta, and R. Datta, *J. Appl. Phys.* **116**, 103505 (2014).

Chapter 3

Probing optical band gaps at nanoscale from tetrahedral cation vacancy defects and variation of cation ordering in NiCo₂O₄ epitaxial thin films

This chapter presents results on probing the optical band gaps at the nanoscale in epitaxial NiCo₂O₄ (NCO) thin films with different structural order (cation/charge) using high resolution electron energy loss spectroscopy (HREELS). Nanoscale regions with unoccupied tetrahedral A site cations are additionally observed. Origin of rich variation in cation ordering in this system is also discussed.

*This work is published in Journal of Physics D: Applied Physics **47**, 405001 (2014).*

3.1 Introduction

NiCo_2O_4 (NCO) belongs to the family of magnetic spinel oxides with various potential technological applications such as fuel cell electrodes, oxygen catalysis, reduction in alkaline media, and water electrolysis [1-3]. NCO is a much less studied system particularly in thin film form in comparison to its close relatives, e.g., NiFe_2O_4 (NFO) and CoFe_2O_4 (CFO) [4-12]. This is partially because of the unavailability of NCO in the single crystalline form. Also, NCO in the powder form is reported to start to decompose at temperatures above 400 °C [2]. Recently, the growth of high quality epitaxial thin film for NiCo_2O_4 on MgAl_2O_4 substrate has been reported. Recent NCO epitaxial thin film studies have indicated rich variations in electrical and magnetic properties depending on the growth conditions, notably the temperature [1-3]. However, studies of changes in the optical properties with variation in cation arrangement and cation vacancy defects as well as any support from first principle based calculations are lacking in the literature in explaining the origin of such rich variation in structural order. We have used spatially resolved high resolution electron energy loss spectroscopy (HREELS) [13-18] to probe the optical band gap and its variation in NCO thin films grown at three different temperatures, namely 550, 350 and 250 °C, and direct measurements have also been made from localized regions with A site cation vacancy. The three samples will henceforth be referred to as NCO550, NCO350 and NCO250, respectively. DFT simulations in Wien2k software has been performed for nonmagnetic, ferromagnetic, cation mixed, cation vacancy cases. The system shows switching between direct and indirect band gap type behavior depending on the structural order. Moreover, introduction of vacant cations at the A sites significantly lowers the band gap of the system by introducing additional states inside the host band gap. Experimentally we observed small variation in band gap values for each sample as measured from different areas and this is due to the slight variation in cation ordering and the observation of very low values are from nanoscale A site cation vacancy regions. Cohesive energy is found to be comparable between various structural configurations, with entropy and lattice parameter likely playing a significant role in stabilizing specific configurations during film deposition. Our findings provide fundamental understanding of the optical properties of this interesting spinel system with variations in cation ordering as well as configurations with A site cation vacancy.

3.2 Magnetic and electrical properties of NiCo₂O₄ epitaxial film on MgAl₂O₄ substrate grown by PLD

The NCO films were grown on (100)-oriented MgAl₂O₄ (MAO) substrates by pulsed laser deposition technique at three different temperatures i.e, 250, 350 and 550 °C. Magnetic and electrical properties can be found in Ref. 1.

Films grown at higher temperature (> 450 °C) are non-magnetic and electrically insulating whereas films deposited at temperatures below 450 °C exhibit ferrimagnetic behavior with metallic conduction by hole carriers. The saturation magnetization (figure 3.1 (a)) and coercivity (figure 3.1 (b)) increased as a function of growth temperature for samples grown below 450 °C but decreases drastically for samples grown at 550 °C. Also, the Curie temperature is below the room temperature, so the samples show weak magnetic ordering at room temperature and strong magnetic ordering at low temperatures. The electronic structure/ band gap is extremely sensitive to such changes in magnetic ordering.

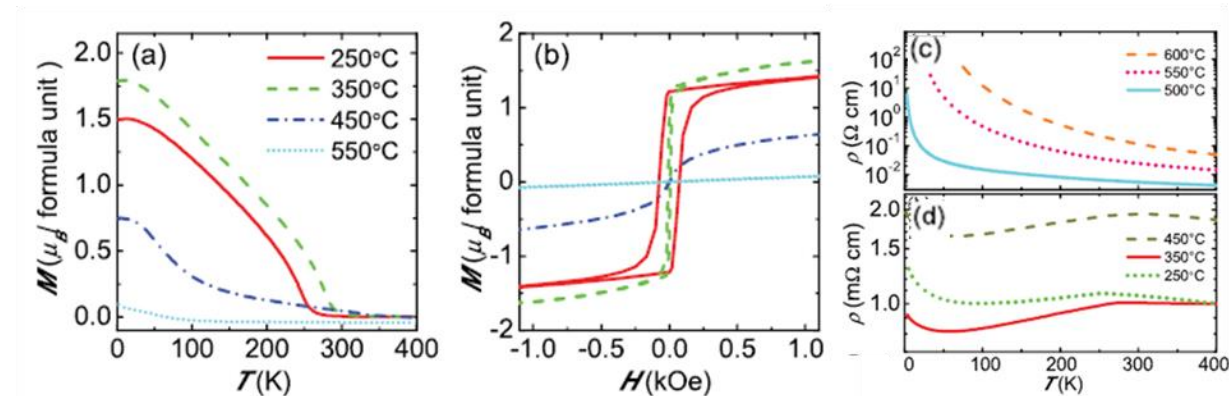


Figure 3.1 (a) Magnetization (M) vs. Temperature curves for samples grown at different temperatures, (b) M vs. Magnetic field (H) curves for the same set of samples. Resistivity (ρ) vs. T curves showing (c) insulating behavior for samples grown > 450 °C and (d) metallic behavior for samples grown < 450 °C Copyright (2012) by American institute of Physics [1].

3.3 Experimental details

Conditions for HRTEM imaging is described in section 2.2. HREELS acquisition and spectra analysis are performed as described in sections 1.4 to 1.6 and 2.2. HREELS measurements for the NCO samples were performed at two different temperatures, i.e. 90K and 300K using *Gatan Cooling Holder*.

3.4 Computational details and results

Electronic structure simulations were performed using Wien2k based density functional theory calculations on the relaxed 56 atoms NCO unit cells. In all the calculations, the spin moments in the *A* site cations of the spinel structure was aligned antiparallel to those in the *B* site cations. Calculations has been performed for the following six different configurations: (a) the ferrimagnetic inverse spinel structure (resulting magnetic moment of 2 $\mu\text{B}/\text{f. u.}$, f. u. stands for formula unit), (b) the non-magnetic inverse spinel structure (magnetic moment was forced to 0 $\mu\text{B}/\text{f. u.}$), (c) the normal spinel structure (magnetic moment of 2 $\mu\text{B}/\text{f. u.}$), (d) with a mixed spinel-inverse spinel structure where 25% and 50% of the *A* site Co atoms are swapped with *B* site Ni atoms (magnetic moment 2 $\mu\text{B}/\text{f. u.}$), (e) inverse spinel with 50% of *A* site atoms removed (magnetic moment of 1.5 $\mu\text{B}/\text{f. u.}$), and (f) all *A* site atoms are removed (magnetic moment of 1 $\mu\text{B}/\text{f. u.}$) from the unit cell. The schematic diagrams of the simulated structures are given in figure 3.2. The rest of the method and the calculation parameters used are as described in section 2.3

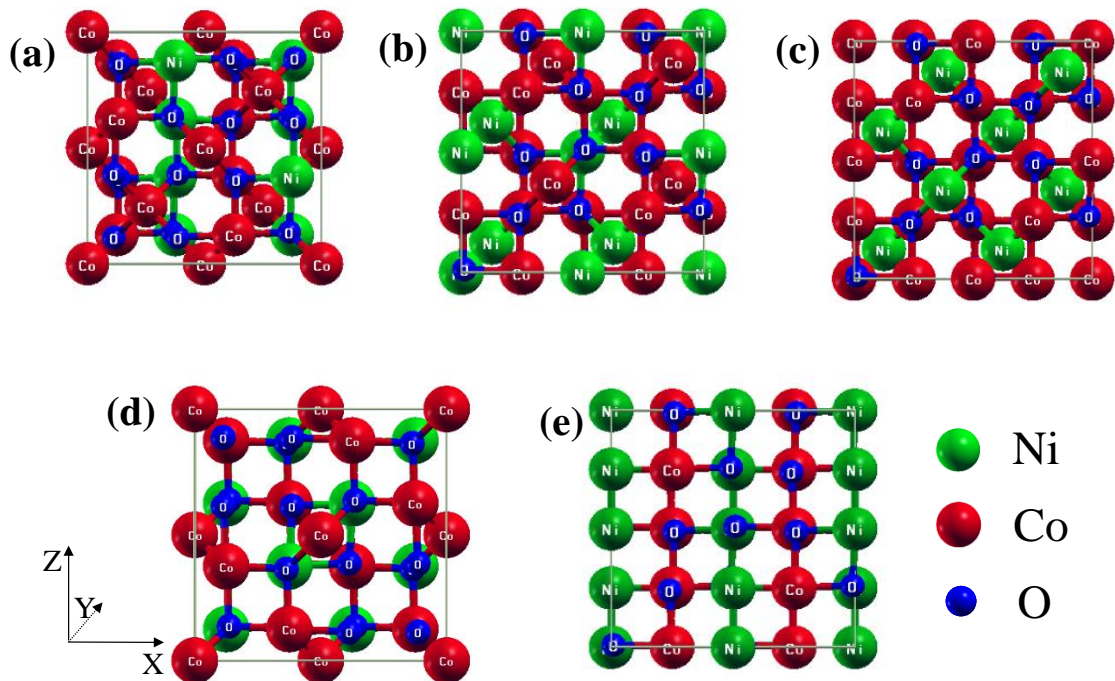


Figure 3.2. Schematics of various simulated structures. (a) Inverse spinel, (b) 50% spinel- Inverse spinel mixed, (c) normal spinel, (d) 50% A site cation vacancies and (e) 100% A site cation vacancies. Copyright (2014) by Institute of Physics [24].

Figure 3.3 summarizes the band gap values and their types (direct or indirect) obtained through mBJLDA calculation for the ideal inverse spinel structure, various degree of cation mixing and considering A site cation vacancies. Band gap due to the nonmagnetic phase of inverse spinel structure is also shown in figure 3.3 (a). The possible interband transitions from various structures considered are shown in table 3.1.

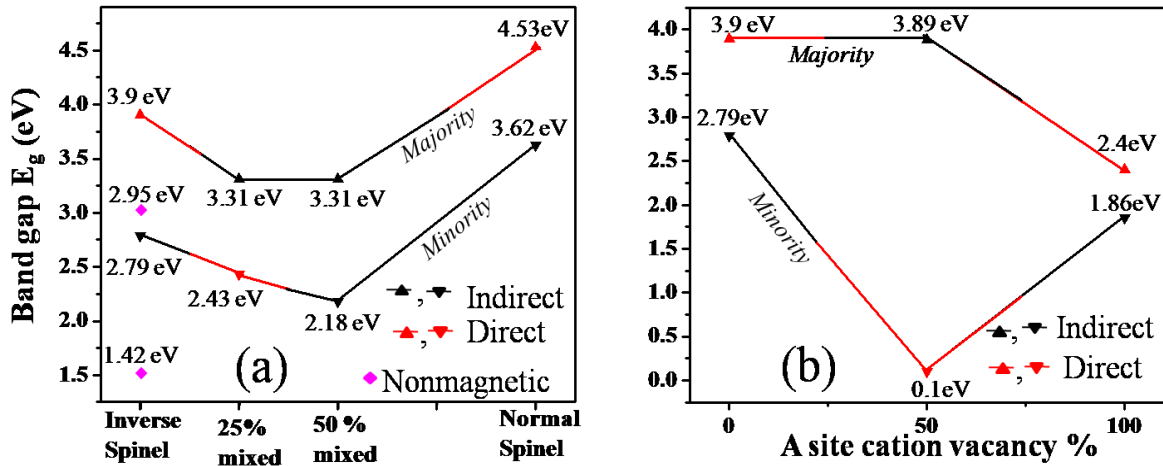


Figure 3.3. Band gap type and values of NiCo₂O₄ with (a) various percentage of structural inversion, and (b) consideration of A site cation vacancy defects. The fundamental band gap values along both majority and minority channels are joined by straight lines. A change from indirect to direct band gap is shown by a change from black to red color. Copyright (2013) by Institute of Physics [24].

Table 3.1. Possible interband transition for different structural configurations, values mentioned here are other than the band gap values already indicated in figure 3.3.

Configurations	Indirect (eV)	Direct (eV)
Inverse spinel NCO (ferrimagnetic)	4, 4.5	-
Inverse spinel NCO (nonmagnetic)	1.6, 1.8, 2.6, 3	1.46, 1.6, 1.8, 2.6, 3
Normal spinel NCO	-	-
50% mixed/inversion	3, 4, 4.6	2.98, 3.8, 4.8
50% T _d vacancy	1.05, 1.51, 2.9, 3.89, 4.49, 4.89	-
100% T _d vacancy	3.36, 3.4, 4.16	3.4

3.5 High resolution imaging of NiCo₂O₄

Figure 3.4 shows an example high resolution image from NCO film. It shows nanoscale regions with ideal lattice arrangement (marked as Y) and A site cation vacancy regions (marked as X). Therefore, it is of interest to understand the local (at nanoscale) electronic structure of such regions besides the effect of mixed charge/cation arrangement. Widely used optical characterization tools such as photoluminescence (PL), cathodoluminescence (CL), and optical absorption spectroscopy should be able to evaluate any signals indirectly from such regions; however, direct correlation is only possible by the combination of imaging and spectroscopy in a TEM. HRTEM can display these areas clearly and thus provides a unique opportunity to directly acquire low loss EELS locally with high signal intensity, unparalleled with other conventional techniques. This makes optical absorption spectroscopy at nanoscale by HREELS very important in this class of materials.

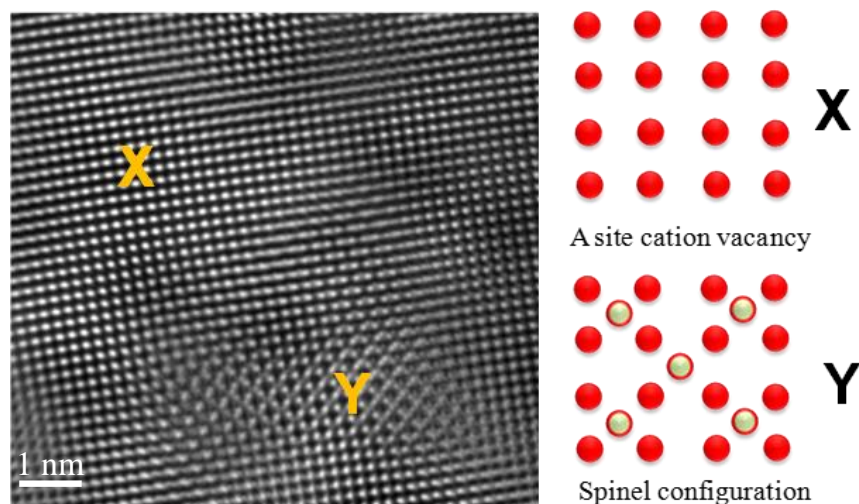


Figure 3.4. HRTEM image of NiCo₂O₄ film oriented along $\langle 100 \rangle$ zone axis. Area with A site cation vacancies is marked as X and region with ideal lattice structure is marked as Y. Schematic of X and Y type regions are shown. Copyright (2013) by Institute of Physics [24].

3.6 Results of optical absorption spectroscopy at nanoscale in NiCo₂O₄

Experimentally determined band gap values for three different samples, both at 300 K and 90 K are listed in Table 3.2. Example Tauc plots used to obtain the direct and indirect band gap information for the three different samples along with areas containing A site vacancy defects are given in figure 3.5.

Table 3.2. Experimental band gap values listed for three different NCO thin films grown at different temperatures. The values marked with the light color are the band edge absorption from A site vacancy regions, deep color are from the non-defective areas and the values without color marks are the inter band transitions.

Sample	300 K		90 K	
	Indirect	Direct	Indirect	Direct
NCO550	1.08±0.3	1.58±0.08	1.12±0.45	1.77±0.11
	2.88±0.26	3.1±0.27	3.62±0.33	2.86±0.18
	4.35±0.3		4.41±0.33	
NCO350	0.62±0.25	1.52±0.27	1.83	2.68±0.27
	1.43±0.34	2.45±0.31	2.95±0.06	3.38±0.1
		3.42±0.35		
NCO250	0.38±0.27	1.84±0.08	0.47±0.09	1.48±0.36
	1.42±0.27	2.76±0.14	2.37±0.24	2.64±0.27
		3.29±0.26		3.49±0.04

Observation of direct band gaps at 1.58 eV and 3.1 eV for NCO550 (figure 3.5 (a)) correspond well with the theoretical prediction for non-magnetic NCO (figure (3.3 (a))). However, presence of indirect transitions values at 2.6 eV and 3.37 eV are due to the interband transitions (Table 3.2). The indirect transitions at 1.08 and 4.35 eV are from the A site cation vacancy regions (figure 3.3 (b), see Table 3.1 for possible interband transitions). Almost the same values are obtained from the measurement at 90 K and this is because the NCO550 sample is in the non-magnetic state at this temperature and shows weak magnetic order only below 80 K, which is beyond the measurement limit of our liquid nitrogen-based cryogenic holder.

For the NCO350 (figure 3.5 (c) and (d)) and NCO250 (figure 3.5 (e) and (f)) samples, fundamental band gap is found to be indirect both at 300 K (i.e. 1.43 and 1.42 eV, respectively) and 90 K temperature (i.e. 2.95 and 2.37 eV, respectively). The band gap increases at the lower temperature 90 K temperature because of ferrimagnetic ordering. Theoretical calculations also indicate larger band gap values for the ferrimagnetic structure as compared to the non-magnetic counterpart. Direct band gap values around 3.3 eV for both the samples are due to interband transitions to states formed by B site Co, as in the case of ferrimagnetic inverse spinel. Some of the very low values of indirect band gaps for both the samples (<1 eV) are from vacant A site regions. The direct transition values at 1.52, 2.45 eV (300 K) and 2.68 eV (90 K) for NCO350

and at 1.84, 2.76 eV (300 K) and 1.48, 2.64 eV (90K) for 250NCO are attributed to interband transitions due to varying percentages of A site cation vacancy regions.

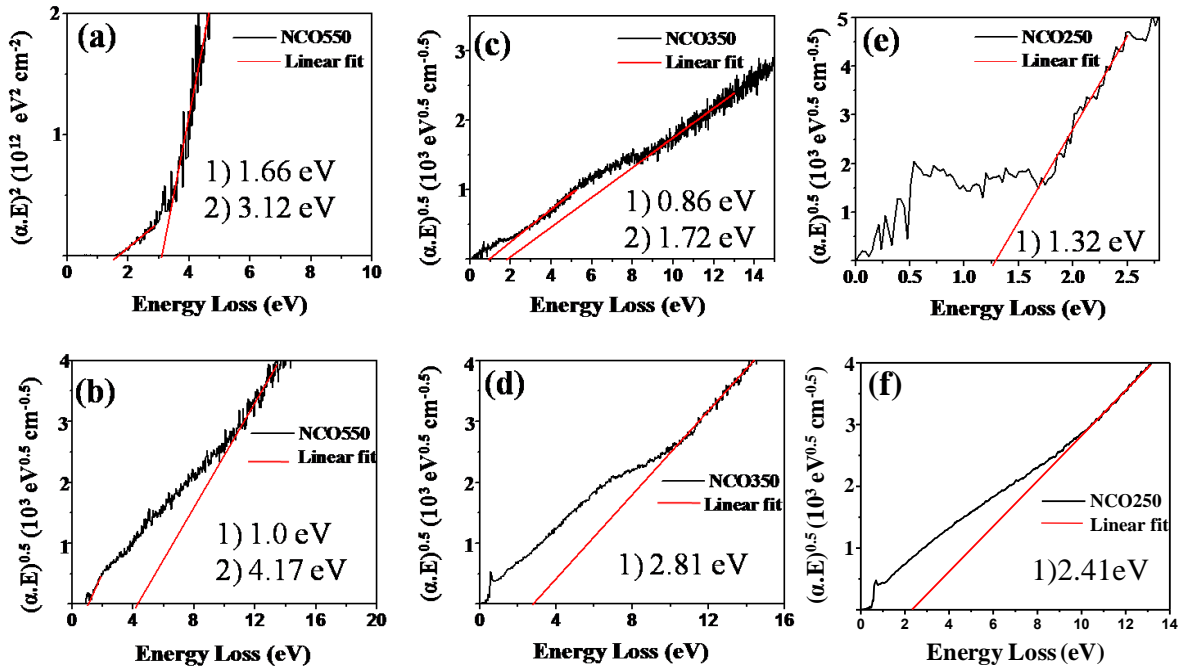


Figure 3.5. Example spectra showing direct band gap for NCO550 at (a) 300 K and (b) from A site cation defects. Indirect band gaps for NCO350 at (c) 300 K and (d) 90 K and NCO250 at (e) 300 K and (f) 90 K. Copyright (2013) by Institute of Physics [24].

3.7 Origin of variation of cation ordering

Table 3.3 compares the theoretical lattice parameters and cohesive energies of NCO with various cation arrangements. The relaxed a lattice parameter for ferrimagnetic inverse spinel NCO is 8.15 Å. In the non-magnetic inverse spinel, the a lattice parameter increases to 8.19 Å. This trend is in good agreement with the experimental observation of Iliev *et al.* that at higher deposition temperatures the magnetic moment decreases along with an increase in the lattice parameter [2]. The difference in cohesive energies of simulated structures (various cation arrangements) is comparable except in the case 25% mixing, indicating the possibility of their coexistence under equilibrium growth conditions. Moreover, experimentally we have observed A site cation vacancies (V_A) at various nanometer length scale regions in the thin film samples. When simulation is performed with 50% of T_d vacancy in the perfect inverse spinel structure, the lattice parameter decreases to 8.01 Å with cohesive energy of 5.1947 eV/atom. When all the T_d

atoms are removed, the lattice parameter further decreases to 7.87 Å with cohesive energy of 4.9171 eV /atom. Both the defect structures are energetically not favorable; however, the entropy and strain may be responsible for their formation in small pockets. Also, while the T_d ion vacancy may not be large, anything between zero and 50% is likely to cause difficulty in imaging atoms at A site atomic column (will appear like vacant A site regions) and the cohesive energy may then be comparable to regular configurations. The experimentally observed decrease in lattice parameter with lower growth temperature is likely due to deviations from the ideal inverse spinel structure towards stable mixed cations in the film [2]. As the difference in cohesive energy values are very small between various structural configurations, the entropy and lattice parameter (through deposition temperature and substrate) both play a significant role in the magnetic order as well as the cation mixing in this system and thus explains the discrepancy between the theoretical minimum energy structure (ferrimagnetic inverse spinel) and the experimental observation of non-magnetic inverse spinel structure at higher deposition temperature. Theoretically, lattice parameter dependent inversion in the case of CoFe₂O₄ structure has previously been reported in the literature [22].

Table 3.3. Theoretical lattice parameters and cohesive energy values for various cation ordering and A site vacancy defects in NCO.

NiCo ₂ O ₄	IS	NS	Mixed		NM	T _d vacancy	
			50%	25%		50%	100%
a (Å)	8.15	8.09	7.95	8.14	8.19	8.01	7.87
Cohesive energy (eV/atom)	5.3443	5.3498	5.3116	6.2137	5.3103	5.1947	4.9171

IS= Inverse Spinel; NS= Normal Spinel; NM= Non-magnetic.

3.8 Influence of A-site cation vacancies in magnetization in the system

The observation of a magnetization of < 2 μ_B/ formula unit (f. u.) has been previously explained based on charge mixing and cation mixing [1]. But we have found that cation/charge mixing cannot result in total magnetic moment < 2 μ_B/ f. u (refer to table 3.4) but A site cation

vacancy can. So, based on DFT results we conclude that A site cation vacancies are responsible for the observed magnetic moment $< 2 \mu_B/\text{f. u.}$ With the introduction of A site cation vacancy, net moment per formula unit decreases to $1.5 \mu_B/\text{f. u.}$ for the 50% defect case and to $1 \mu_B/\text{f. u.}$ for the 100% defect case [1].

Table 3.4. Atom specific magnetic moments obtained from theoretical calculation. Net moment per formula unit is mentioned in the text for each case.

	Magnetic moment (μ_B/atom)					
	Inverse spinel (ferrimagnetic)	Inverse spinel (nonmagnetic)	Normal spinel	50% mixed/inversio n	50% T _d vacancy	100% T _d vacancy
A site Co	2.95	2.64	-	2.77	2.85	
A site Ni	-	-	1.97	1.94	-	
B site Ni	-1.48	-2.35	-	-1.33	-1.2	0.53
B site Co	0.03	0.08	-0.16	0.02	-0.01	-1.42
O	0.11	-0.16	0.11	0.05	0.2	-0.02
Total/f.u/	2	0	2	2	1.5	1

3.9 Coexistence of two extreme classes of transition metal oxide semiconductor

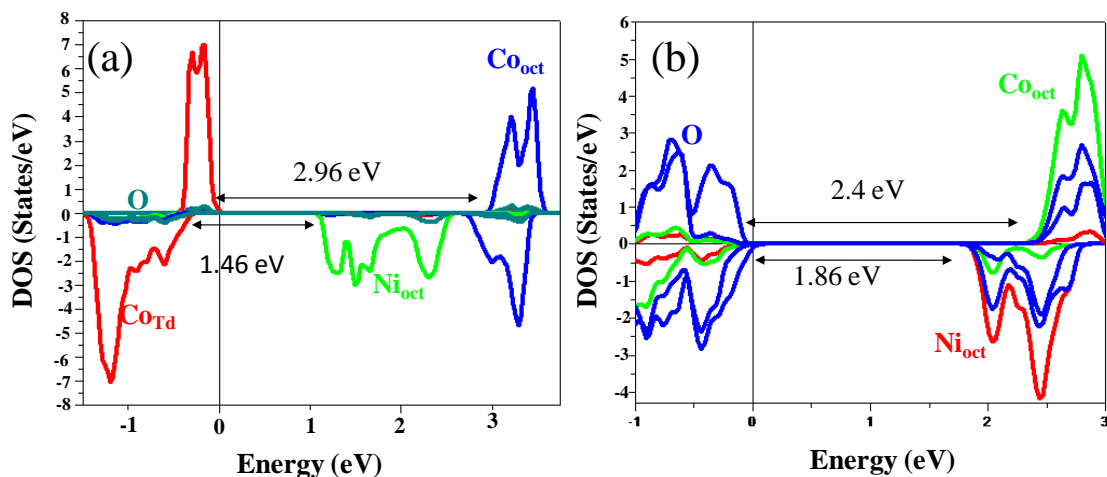


Figure 3.6. Example of (a) a Mott-Hubbard type insulator (nonmagnetic inverse spinel) and (b) a charge transfer type insulators (ferrimagnetic inverse spinel structure with 100% A site cation vacancy). Copyright (2013) by Institute of Physics [24].

Zaanen-Sawatzky-Allen diagram classifies insulating materials into two extreme limits as charge transfer type (CT) ($U > \Delta > W$) and Mott-Hubbard (MH) ($\Delta > U > W$) type [23], where U is the on-site Coulomb repulsion, Δ is the ligand to metal charge transfer and W is the bandwidth. An insulating oxide system is predicted either to be CT or MH by directly considering the partial O p and the metal d density of states. If the O p DOS is dominant at the top of the valence band near the Fermi level over the metal d states, then the system is a CT type. If metal d -states dominate over O p states at the top of the valence band, then the system is a Mott-Hubbard type. The nonmagnetic inverse spinel is a Mott-Hubbard type insulator and the structure with 100% A site cation vacancies is of charge transfer type (figure 3.6) and found to coexist in NCO thin films.

3.10 Conclusion

In conclusion, first principle based theoretical and experimental comparison of optical band gaps of spinel NiCo₂O₄ with different cation configurations and vacant A site defects is presented and they are found to be in good agreement. A unique finding of this study is the universal mixed charge state for both the A (Co) and B (Ni) site cations in this system for the various cation configurations. The cohesive energy values are comparable for the different structural arrangements and therefore the entropy and lattice parameter likely play a significant role in stabilizing a specific cation configuration for a particular growth temperature and substrate lattice parameter. The NCO spinel oxides with A site cation vacancy is commonly observed and have significantly lower band gap and magnetic moment values compared to the defect-free cases.

3.11 Bibliography

- [1] P. Silwal, L. Miao, I. Stern, X. Zhou, J. Hu, and D. H. Kim, Appl. Phys. Lett. **100**, 032102 (2012).
- [2] M. N. Iliev, P. Silwal, B. Loukya, R. Datta, D. H. Kim, N. D. Todorov, N. Pachauri, and A. Gupta, J. Appl. Phys. **114**, 033514 (2013).

- [3] P. Silwal, L. Miao, J. Hu, L. Spinu, D. H. Kim, and D. Talbayev, *J. Appl. Phys.* **114**, 103704 (2013).
- [4] N. Li, S. Schäfer, R. Datta, T. Mewes, T. M. Klein, and A. Gupta, *Appl. Phys. Lett.* **101**, 132409 (2012)
- [5] Q.-C. Sun, H. Sims, D. Mazumdar, J. X. Ma, B. S. Holinsworth, K. R. O'Neal, G. Kim, W. H. Butler, A. Gupta, and J. L. Musfeldt, *Phys. Rev. B* **86**, 205106 (2012).
- [6] D. Meier, T. Kuschel, L. Shen, A. Gupta, T. Kikkawa, K. Uchida, E. Saitoh, J.-M. Schmalhorst, and G. Reiss, *Phys. Rev. B* **87**, 054421 (2013).
- [7] L. Shen, M. Althammer, N. Pachauri, B. Loukya, R. Datta, M. Iliev, N. Bao, and A. Gupta, *J. Cryst. Growth* **390**, 61 (2014).
- [8] Z. Szotek, W. M. Temmerman, D. Ködderitzsch, A. Svane, L. Petit, and H. Winter, *Phys. Rev. B* **74**, 174431 (2006).
- [9] D. Fritsch and C. Ederer, *Phys. Rev. B* **82**, 104117 (2010).
- [10] D. Fritsch and C. Ederer, *Phys. Rev. B* **86**, 014406 (2012).
- [11] A. V. Ravindra, P. Padhan, and W. Prellier, *Appl. Phys. Lett.* **101**, 161902 (2012).
- [12] K. Dileep, B. Loukya, N. Pachauri, A. Gupta and R. Datta, *J. Appl. Phys.* **116**, 103505 (2014).
- [13] R. Datta, S. Kanuri, S. V. Karthik, D. Mazumdar, J. X. Ma and A. Gupta, *Appl. Phys. Lett.* **97**, 071907 (2010).
- [14] R. Datta, B. Loukya, N. Li and A. Gupta, *J. Cryst. Growth* **345**, 44 (2012).
- [15] Q. M. Ramasse, C. R. Seabourne, D. M. Kepaptsoglou, R. Zan, U. Bangert, and A. J. Scott, *Nano Lett.* **13**, 4989 (2013).

- [16] W. Zhou, M. D. Kapetanakis, M.P. Prange, S.T. Pantelides, S. J. Pennycook, and J. C. Idrobo, *Phy. Rev. Lett.* **109**, 206803 (2012).
- [17] R. Sahu, K. Dileep, B. Loukya and R. Datta, *Appl. Phys. Lett.*, **104**, 051908 (2014).
- [18] K. Venu, S. Kanuri, K. Raidongia, K.P.S.S. Hembram, U. V. Waghmare and R. Datta, *Sol. State Comm.* **150**, 2262 (2010).
- [19] K. Dileep, L. S. Panchakarla, K. Balasubramanian, U. V. Waghmare, and R. Datta, *J. Appl. Phys.* **109**, 063523 (2011).
- [20] K. Dileep, and R. Datta, *J. Alloys and Compounds* **586**, 499 (2014).
- [21] P. D. Battle, A. K. Cheetam, and J. B. Goodenough, *Mat. Res. Bull.* **14**, 1013 (1979).
- [22] D. Fritsch and C. Ederer, *Appl. Phys. Lett.* **99**, 081916 (2011).
- [23] J. Zaanen, G. A. Sawatzky, and J. W. Allen, *Phys. Rev. Lett.* **55**, 418 (1985).
- [24] K.Dileep, B. Loukya. P.Silwal, A. Gupta, and R. Datta, *J. Phys. D: Appl. Phys.* **47**, 405001 (2014).

Chapter 4

Layer specific optical band gap measurement at nanoscale in MoS₂ and ReS₂ van der Waals compounds by high resolution electron energy loss spectroscopy

This chapter presents results on layer specific optical absorption spectroscopy from MoS₂ and ReS₂ van der Waals compounds and a distinction is made from analyzing the optical absorption spectra from simple system like ZnO. Indirect to direct crossover is observed in MoS₂ going from bilayer to monolayer while no such transition is observed in ReS₂. The spin-orbit split K-point twin exciton peaks have been observed for monolayer MoS₂.

*This work is published in Journal of Applied Physics **119**, 114309 (2016).*

4.1 Introduction

In modern information and computation technology, there is a demand for continuous miniaturization of the electronic devices. One way to achieve atomically thin devices is through utilizing the two-dimensional materials like graphene and transition metal dichalcogenides (TMDs). Monolayer TMDs have promising optoelectronic, energy and novel device applications. One of the important features of many TMDs is that they undergo a crossover from indirect band gap in the bulk to direct band gap in the monolayer form [1-9]. The existence of a direct band gap and a very high exciton binding energy (1.1 eV) is a major advantage over graphene for practical device applications [10]. This allows emitting light efficiently in the monolayer forms and constructing field effect transistor devices at extremely small length scale [6, 8]. The crossover from indirect to direct band gaps has been explained based on strong interlayer coupling and confinement effects [9]. While the monolayer properties of TMDs are unique, they may be elusive while fabricating practical devices because of unavoidable electronic packaging and the property changes in close proximity of foreign substance due to electronic coupling and van der Waals interaction [10]. Therefore, there is an urge to embed such novel properties arising from the monolayer in the interface or stabilizing the same in the bulk form. With this goal there is a candidate material already reported in the family, which is distorted $1T_d$ - ReS_2 , where the interlayer van der Waals coupling is extremely weak i.e. 18 meV compared to 460 meV of MoS_2 [11]. ReS_2 was reported to exhibit monolayer behavior in the bulk form and shows direct band gap in the range of 1.5-1.6 eV. This also offers exploring the 2-D physics of TMDs in 3-D form. Though there are many reports based on this class of materials, however, so far it is mostly photoluminescence technique (with enhanced intensity) combined with first principle based calculation was used to interpret the crossover between indirect to direct band gap in these systems. To best of our knowledge no direct layer specific absorption spectroscopy measurement has been done in these systems previously and the details of the optical response in terms of energy loss function. Therefore, we have exploited high resolution electron energy loss spectroscopy (HREELS) to probe layer specific optical band gap in both MoS_2 and ReS_2 . HREELS technique to measure optical band gap is equivalent to optical absorption spectroscopy but with the advantage of selected area information at the nano and atomic scale [12, 13]. In addition to this, the high energy electrons (300 kV in the present case)

has much larger momentum than equivalent photon and transfer both energy and momentum to the crystal electrons during an inelastic event thus allowing measurement of both direct and indirect transitions.

4.2 Experimental Details

TEM samples were prepared by liquid phase exfoliation of bulk MoS₂ powder (Sigma Aldrich) and bulk ReS₂ powder followed by drop casting on a holey carbon grid. Rhenium disulfide was synthesized by directly heating small pieces of elemental rhenium cut from a wire (1.0 mm diameter, 99.97%, Alfa Aesar) and sulfur (powder, -325 mesh, 99.5%, Alfa Aesar) in the stoichiometric ratio (1:2) in an evacuated (10^{-5} mbar pressure) quartz tube to 200 °C in 15 h followed by annealing at that temperature for 2 h. This step involving very slow heating to a low temperature was necessary in order to avoid any possibility of explosion due to high vapor pressure of sulfur. Next the temperature was increased stepwise to 400 °C and finally to 900 °C over the course of 10 and 24 hours, respectively. The sample was kept at this temperature for 120 hours to ensure proper homogeneity. The final product was a fine black powder. Conditions for HRTEM imaging is described in section 2.2. HREELS acquisition and spectra analysis are performed as described in sections 1.4 to 1.6 and 2.2 wherever applicable.

However, careful analysis is required to confirm if Tauc plots (see section 1.6) can be applied to obtain direct and indirect band gaps in quasi two dimensional TMDs. In a material like ZnO, where band dispersion is steep parabolic for a wide range of energy and momentum values, competing transitions are absent near the band gap onset (figure 4.1 (a)) and the density of states is devoid of Van Hove singularities till 8 eV (figure 4.1 (b)), the system approximates very well to a three-dimensional electron gas problem and Tauc plots give linear fitting through large number of data points over a large energy range and accurate band gap values can be measured (figure 4.1 (d)). Previously, a step function fitting along with JDOS for direct band gap and phonon assisted absorption function for indirect band gap was used for MoS₂ which approximates the system to the ideal 2D electron gas where DOS is typically independent of energy [2]. However, in quasi 2D systems like MoS₂ and ReS₂ the DOS is not energy independent, have several Van Hove singularities very near the offsets, parabolic bands are shallow and competing transitions could be present near the onset. So, the analysis of absorption

spectra is complicated. The difference between the theoretical and experimental energy loss function and Tauc plot is that the probability of transitions is selected phenomenologically for the latter case and helps finding the most probable direct or indirect band gap; whereas the theoretical calculations consider all possible transitions including phonon assisted inter-band transitions integrated over the Brillouin zone. However, if one of them is dominating then the determination of another type of band gap becomes difficult through usual linear extrapolation if the energy difference is small. This is the case for MoS₂ bilayer and will be demonstrated while presenting the experimental data. For ReS₂, no such difficulty is encountered as there are no competing transitions existing either theoretically or experimentally though bands are shallower. This is because of only a pair of band minima is present in the entire momentum space.

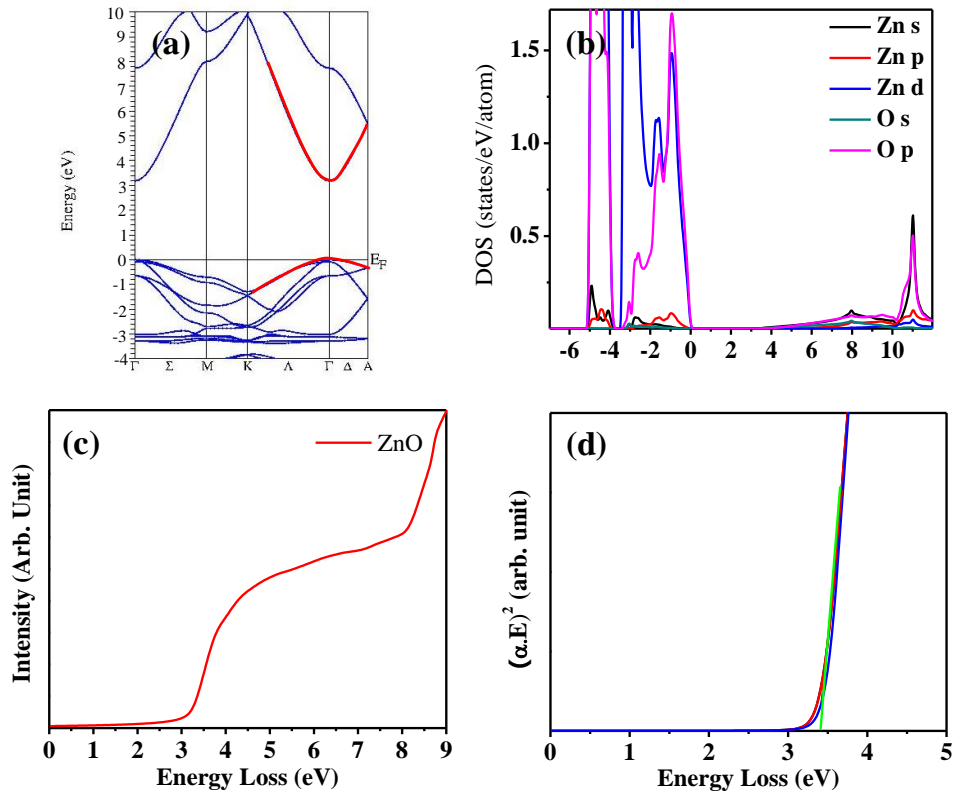


Figure 4.1. (a) Band structure of ZnO along high symmetry points in the Brillouin zone, (b) density of states of ZnO (c) energy loss function shows $(E-E_g)^{1/2}$ type of behavior till ~ 8 eV and (d) the corresponding Tauc plot.

The thickness of the materials under investigation was extremely thin i.e. one unit cell thickness for monolayer (3.14 Å for monolayer MoS₂ and ~ 3.3 Å for monolayer ReS₂) and its

multiples depending on the number of layers. Therefore, at such very low thicknesses, the effect of Cherenkov radiation, on the energy loss spectra will be absent [14, 15].

4.3 Theoretical electronic structure and optical property calculation using WIEN2k code

Electronic structure calculations were performed using density functional theory based WIEN2k code. The code uses linearized augmented plane waves as basis and considers all electrons into the calculation. Following structures were considered for the theoretical calculation: (a) bulk 2H-MoS₂, (b) monolayer 2H-MoS₂, (c) distorted bulk 1T_d-ReS₂, and (d) distorted monolayer 1T_d-ReS₂. The schematic of the simulated structures are given in figure 4.2. A Γ centered $30 \times 30 \times 18$ and $30 \times 30 \times 1$ k-point mesh were used for a unit cell containing two formula units Bernal stacked (2H-poly type) along *c*-direction for the bulk and a single formula unit per unit cell for monolayer calculations, respectively, and the number was reduced proportionally for the larger supercell. For bulk 2H-MoS₂ calculation, a unit cell consisting of two MoS₂ formula units with Bernal stacking along the *c*-direction was considered. The dispersion correction due to van der Waal interaction was included according to DFTD3 method [16]. Zero damping method was used in the van der Waal's energy expression. The dispersion interaction was cutoff at 95 Bohr and the forces were calculated numerically. For monolayer calculation a vacuum of 16 Å was created between the layers in order to prevent interlayer interactions. Lattice parameters were optimized using Perdew-Burke-Ernzerhof (PBE) functional within generalized gradient approximation (GGA). The relaxed lattice parameters of bulk MoS₂ are $a = 3.1858$ Å and $c = 12.8540$ Å, respectively. The interlayer distance (the S-S distance) perpendicular to the '*c*' plane is 3.28 Å. The relaxed *a* lattice parameters of monolayer MoS₂ is 3.1917 Å.

In distorted 1T_d ReS₂ structure, four Re atoms together forming Re₄ cluster creating a 2×2 superstructure (figure 4.2 (d)). 1T_d-ReS₂ is simulated by triclinic unit cell consisting of four ReS₂ units (figure 4.2 (f)). The relaxed lattice parameter of the bulk ReS₂ are $a = 6.4112$ Å, $b = 6.4714$ Å, $c = 6.4213$ Å, $\alpha = 91.32^\circ$, $\beta = 105.49^\circ$, and $\gamma = 119.03^\circ$. Interlayer S-S distance in this case is 2.62 Å. The relaxed lattice parameters for monolayer ReS₂ are $a = 6.4308$ Å, $b = 6.4912$ Å, and $\gamma = 119.03^\circ$. The rest of the method and the calculation parameters used for SCF cycle are as described in section 2.3.

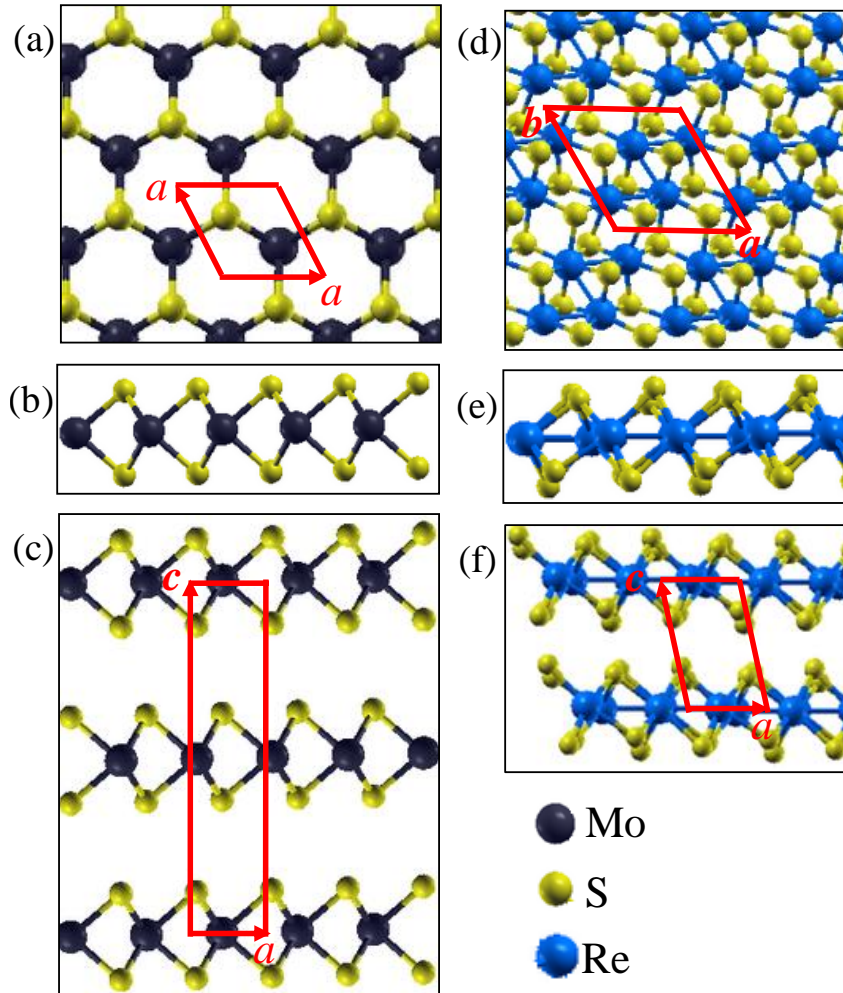


Figure 4.2. Schematic structure of (a) monolayer 2H-MoS₂ along $\langle 0001 \rangle$, (b) along $\langle 11-20 \rangle$, (c) Bernal stacking for bulk 2H-MoS₂ along $\langle 11-20 \rangle$, (d) 1T_d monolayer ReS₂ along $\langle 0001 \rangle$, (e) along $\langle 11-20 \rangle$ and (f) Bernal stacking for bulk 1T_d along $\langle 11-20 \rangle$. Unit cell and in plane lattice vectors are shown.

The energy loss function (ELF) for monolayer and bulk MoS₂ and ReS₂ are calculated using OPTIC program in WIEN2k [17]. Calculation of ZnO is also carried out to compare the difference between the systems. The momentum matrix elements are calculated with the same dense k-point mesh chosen for the SCF cycles. The imaginary part of the dielectric function is calculated by combining both the momentum matrix elements and the interband transitions summed over the Brillouin zone along different polarization directions. The real part of the dielectric function and energy loss function are then calculated by Kramers-Kronig transformation. The results obtained from the theoretical calculations are compared with the experimental energy loss functions.

4.4 High resolution imaging of MoS₂ and ReS₂

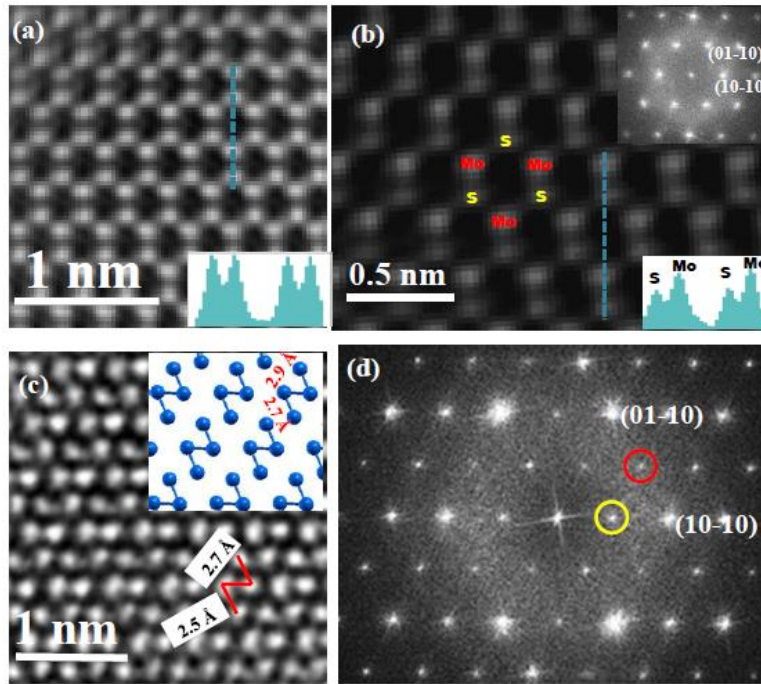


Figure 4.3. HRTEM images of (a) multilayer 2H-MoS₂ along <0001>. The intensity profile across the columns is shown in the lower right inset, Intensity from Mo and S columns are almost same in this case. (b) monolayer 2H-MoS₂. Mo and S atoms are marked. The FFT is shown in the upper right inset, the intensity profile across columns is shown in lower right inset and intensity line trace gives higher signal for Mo compared to S. HRTEM of (c) monolayer distorted 1T-ReS₂. The 'diamond shaped' shaped Re₄ cluster is highlighted. The DFT calculated Re₄ clusters are shown in upper right inset. (d) FFT of distorted 1T-ReS₂. The superstructure spots are marked with the yellow circle.

HRTEM image of few layers MoS₂ along <0001> Z.A shows the 2H poly-type structure (figure 4.3 (a)). Because of the Bernal stacking in few layer MoS₂, Mo and S atomic potentials overlap along the projection direction, resulting in almost equal intensities in all the atomic columns. Whereas for monolayer the intensity line trace shows higher signal from Mo atoms compared to S atoms under negative C_s imaging condition (figure 4.3 (b)) and this is because of higher atomic number of Mo (42) compared to S (16) [1, 18]. MoS₂ shows regular hexagonal diffraction pattern corresponding to 2H structure (inset FFT of (figure 4.3 (b))), where in projection image three S atoms will appear surrounding one Mo atom. No superstructure is observed either by imaging or diffraction. In ReS₂ the most stable structure is Peierls distorted 1T_d associated with the periodic modulation involving clustering of four Re atoms forming a Re₄

‘diamond unit’ and coupling between such units give rise to ‘diamond chains’ (figure 4.3 (c)). This distortion has the origin in minimization of the energy of electrons due to the presence of large number of states at the E_F by opening a gap at half way in the Brillouin zone and the gain in energy is more than the elastic energy cost on the formation of Re_4 diamond unit [7, 11, 19]. The dimensions as indicated in (figure 4.3 (c)) of the Re_4 clusters are measured to be $2.5 \text{ \AA} / 2.7 \text{ \AA}$ and $2.7 \text{ \AA} / 2.9 \text{ \AA}$ from atomic resolution imaging and DFT calculation, respectively. Figure 4.3 (d) is the FFT of ReS_2 HRTEM image. The (10-10) and (01-10) diffraction spots are marked. The diffraction pattern of 1T_d structure is different than 2H counterpart with extra spots appearing along $\langle 11-20 \rangle$ (marked with red circles) due to rotation of one of the S hexagons by 30° with respect to rest of the hexagons corresponding to Re and S atoms in a unit cell [18]. The superstructure spots corresponding to the Re_4 clusters are marked with yellow circles having periodicity of $g = \frac{1}{2}\langle 01-10 \rangle$.

4.5 Layer specific band gap measurement by HREELS

The fundamental band gap of monolayer MoS_2 is direct (figure 4.4 (a)). Competing transitions are absent very near to the absorption onset value. Tauc plot for direct band gap ($(\alpha \cdot E)^2$ vs. E) shows a sharp onset (figure 4.4 (b)) and a direct band gap value of 1.98 eV is obtained. The Tauc plot corresponding to indirect band gap shows poor linear behavior owing to the absence of any significant phonon assisted transition in monolayer MoS_2 .

In multilayer MoS_2 , the fundamental band gap is indirect (figure 4.4 (d)). Figure 4.4 (f) is the Tauc plot for indirect band gap in multilayer MoS_2 which shows a steep linear behavior. An indirect band gap value of 1.27 eV has been obtained which is very close to the band gap (1.29 eV) found for bulk MoS_2 [2, 20]. The Tauc plot for direct band gap (figure 4.4 (e)) is dominated by indirect transitions and only the direct transition peak can be identified at 1.75 eV. This occurs because of two different transitions having almost similar probability unlike in the case of monolayer where only direct transition is significant. This is due to the significant difference in exciton binding energy between monolayer (1.1 eV) and bulk (0.1 eV). From bilayers (figure 4.6 (a)) and three layers (figure 4.6 (b)) region an indirect band gap of 1.8 and 1.39 eV are obtained, respectively. The band gap is plotted as a function of number of layers of MoS_2 has been plotted

in figure 4.6 (c). Direct to indirect band gap transition is observed going from monolayer to bilayer in MoS₂.

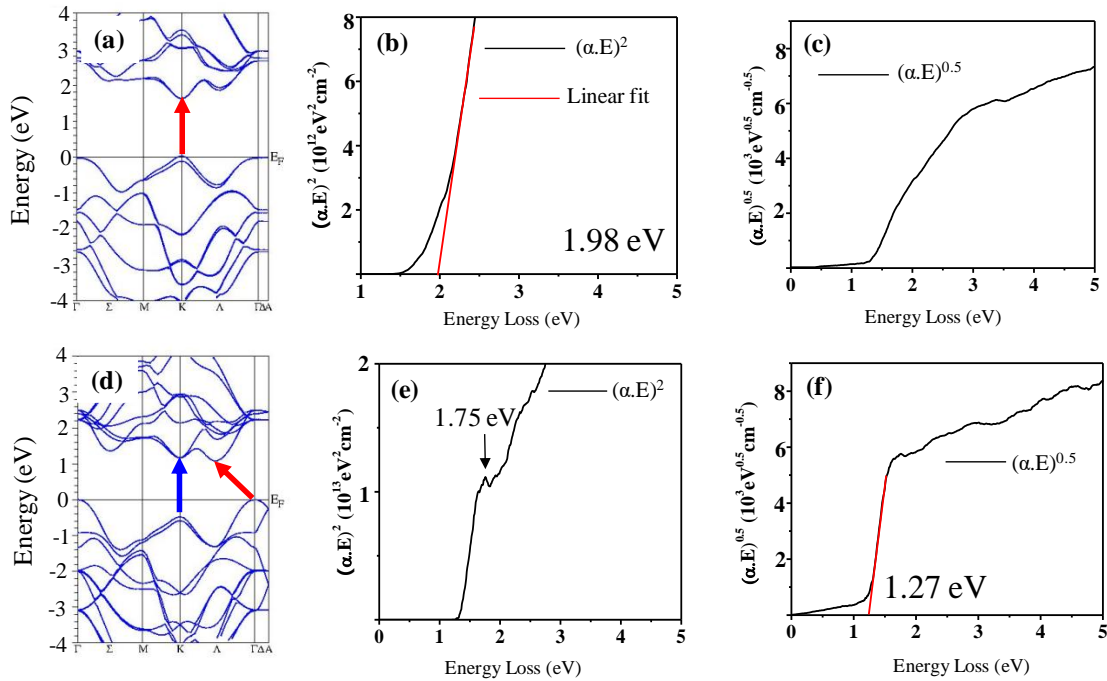


Figure 4.4 (a) Band structure plot, Tauc plot, (b) for direct and, (c) indirect band gap for monolayer MoS₂. (d) Band structure plot, Tauc plot (e) for direct and (f) indirect band gap for multilayer MoS₂.

The fundamental band gap for both monolayer and multilayers ReS₂ is direct. Tauc plots for monolayer and multilayers ReS₂ are given in figure 4.5 (b) & (c) and figure 4.5 (e) & (f) respectively. For multilayers, the Tauc plot for indirect band gap does not show any linear segment, while the Tauc plot for direct band gap gives a value of 1.42 eV. For monolayer the Tauc plots show similar behavior and a direct band gap of 1.52 eV is obtained (figure 4.5 (e)). It was already reported that for ReS₂ both monolayer and many layers will show direct band gap due to weak interlayer coupling and van der Waals interaction. The EELS has the advantage in this case compared to the reported very broad PL emission from monolayer ReS₂ probably cross signals coming from neighboring regions with varying number of layers [11].

From bilayers (figure 4.6 (d)) and three layers (figure 4.6 (e)) region a direct band gap of 1.46 and 1.42 eV are obtained, respectively. Figure 4.6 (f) plots the layer number dependent band gap values and the type for ReS₂. Unlike MoS₂, no direct to indirect crossover is observed in ReS₂.

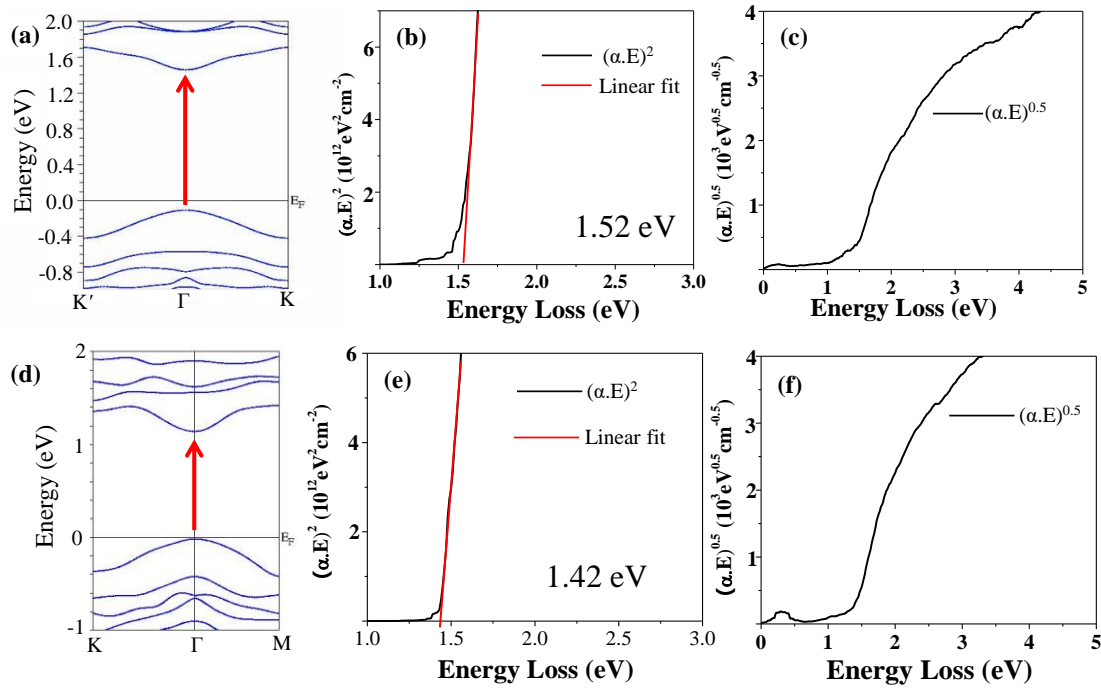


Figure 4.5 (a) Band structure plot, Taucplot (b) for direct and (c) indirect band gap for monolayer $1T_d$ - ReS_2 . (d) Band structure plot, Taucplot (e) for direct and (f) indirect band gap for multilayer $1T_d$ - ReS_2 .

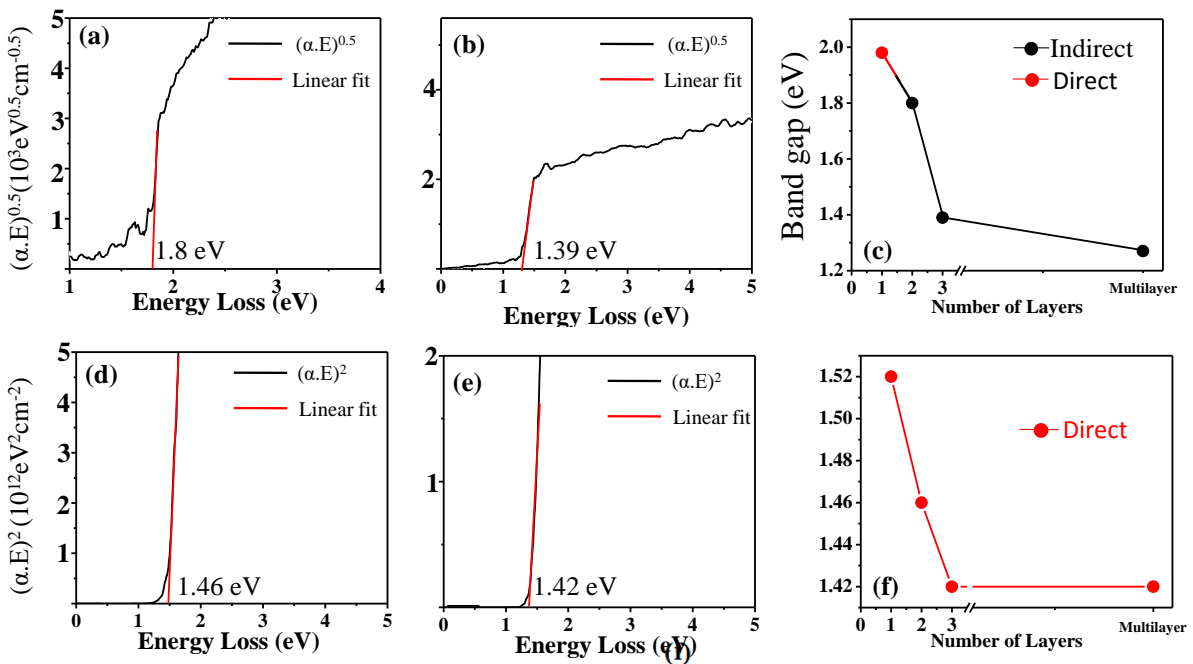


Figure 4.6. The Tauc plot for (a) indirect band gap of two layer MoS_2 , (b) indirect band gap of three layer MoS_2 . (c) Layer specific plots of band gaps and their types for MoS_2 . (d) Direct band gap of two layer ReS_2 and (e) direct band gap of three layer ReS_2 . (f) Layer specific plots of band gaps and their types for ReS_2 .

4.6 Calculated and experimental energy loss function

Figure 4.7 (a) & (b) show the theoretical and experimental energy loss function (ELF) of monolayer MoS₂, respectively. The spin-orbit split twin exciton peaks at the K point of the Brillouin zone are marked as A and B and experimentally appear at 1.8 and 1.95 eV, respectively. Similar experimental peak is observed based on optical absorption spectroscopy with slight difference in the peak positions [21]. The difference in peak position between theory (1.67 and 1.82 eV) and experiment could be due to inaccuracy in calculating exact form of the excited states in the system. The three transitions peaks A, B and C identified in both theoretical and experimental energy loss function of monolayer MoS₂ have been correlated with the Van Hove singularities in the corresponding DOS plot (figure 4.7 (c)). Peak A and B at the onset in the energy loss function are the spin orbit split d_z^2 to d_z^{2*} (VBM to CBM) transitions. The peak at 3 eV corresponds to Mo d_z^2 to Mo $d_{x^2-y^2}$ transition. Note that the $\Delta l \neq 1$ transitions are allowed because of hybridization between the states. ELF along with DOS for bulk MoS₂ is shown in figure 4.7 (d)-(f). Peak A' at the onset and peak B' at 3 eV are marked and have the same origin as mentioned above.

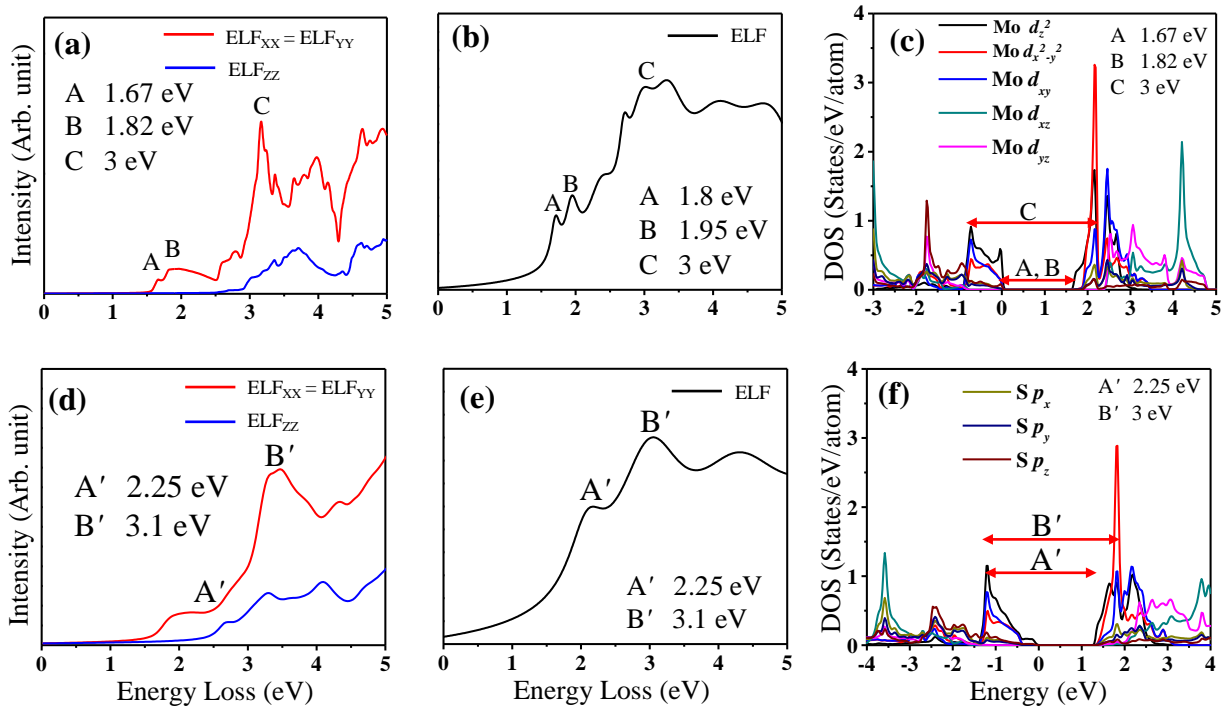


Figure 4.7. (a) & (d) Theoretical, (b) & (e) experimental energy loss functions and (c) & (f) DOS for monolayer and bulk 2H-MoS₂, respectively. The transitions associated with sharp features are marked and correlated with DOS.

The theoretical and experimental ELF for monolayer distorted $1T_d$ ReS₂ is shown in figure 4.8 (a) & (b). The peaks at 2 and 3 eV (A and B) are indicated. Peak A is the transition from d_{yz} to $d_{x^2-y^2}$. Peak B is due to d_z^2 to d_z^2 * transition (figure 4.8 (c)). After the onset ELF is flat because of almost flat p - d hybridized bands on both sides of the Fermi level and the presence of states at higher energy range. Figure 4.8 (d) & (e) shows the ELF from multilayer distorted $1T_d$ ReS₂. It shows rather abrupt onset and can be explained by the steep valence band offset and conduction band onset of DOS compared to monolayer. After the onset the ELF in this case is also flat because of delocalized d state hybridized with S - p states forming flat DOS on both sides of the Fermi energy (Figure 4.8 (f)). The anisotropic electronic structure of ReS₂ can be engineered by the application of strain along different directions with respect to the Re₄ diamond chain [19, 22]. It was also reported that formation of S vacancy is energetically favorable in this system and formation of vacancy Re gives rise to magnetism [23]. The anisotropic absorption obtained by experiment in this system is in the range of 0.05 eV [24] and 0.025 eV with respect to the axis system used in this manuscript which is consistent in terms of no significant difference in the absorption onset of ELF calculated in the present report but differs largely with the theoretical calculation reported in Ref. 22.

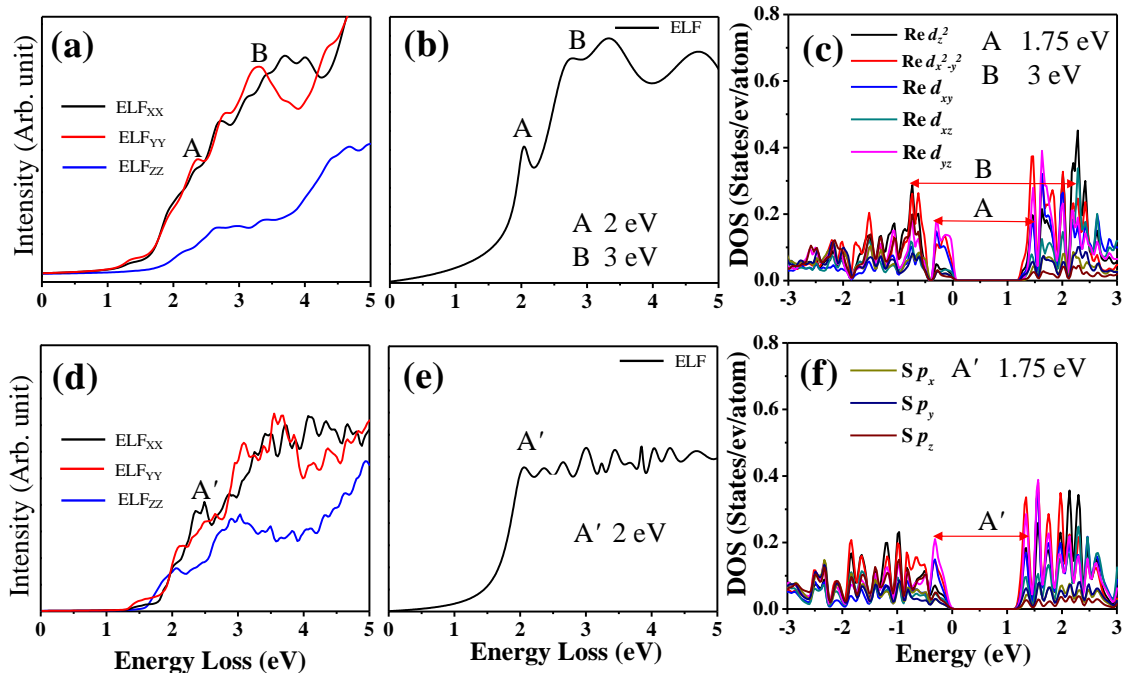


Figure 4.8. (a) & (d) Theoretical, (b) & (e) experimental energy loss functions and (c) & (f) DOS for monolayer and bulk $1T_d$ -ReS₂, respectively. The transitions associated with sharp features are marked and correlated with DOS.

4.7 Conclusions

We have studied the layer specific optical band gaps at the nanoscale of mono to a few layers of 2H-MoS₂ and distorted 1T-ReS₂ by spatially resolved HREELS technique. An indirect band gap of 1.27 eV and a direct band gap of 1.98 eV are obtained for multilayer and monolayer MoS₂, respectively. The spin orbit split K-point exciton has been observed for the monolayer MoS₂. A direct to indirect band gap cross over is observed between monolayer to bilayers MoS₂. ReS₂ showed direct band gaps of 1.52 eV and 1.42 eV for mono and multilayers, respectively. The chemically synthesized 1T-ReS₂ is found to be in a Peierls distorted Re₄ cluster configuration. The results demonstrate the power of HR-EELS technique as a nanoscale optical absorption spectroscopy tool where no other alternative exist in terms of simultaneous imaging and spectroscopy at the atomic and nanometer length scale.

4.8 Bibliography

- [1] H. S. S. R Matte, A Gomathi, A. K Manna, D. J Late, R. Datta, S. K Pati, and CNR Rao, *Angew. Chem. Int. Ed.* **49**, 4059 (2010).
- [2] K. Mak, C. Lee, J. Hone, J. Shan, and T. F. Heinz, *Phys. Rev. Lett.* **105**, 136805 (2010).
- [3] A. Splendiani, L. Sun, Y. Zhang, T. Li, J. Kim, C-Y Chim, G. Galli, and F. Wang, *Nano Lett.* **10**, 1271(2010).
- [4] Q. H. Wang, K. Kalantar-Zadeh, A. Kis, J. N. Coleman, and M. S. Strano, *Nat. Nano* **7**, 699 (2012).
- [5] M. Chhowalla, H. S. Shin, G. Eda, L-J Li, K. P. Loh, and H. Zand, *Nat. Chem.* **5**, 263 (2013).
- [6] D. Jariwala, V. K. Sangwan, L. J. Lauhon, T. J. Marks, and M. C. Hersam, *ACS Nano* **8**, 1102 (2014).
- [7] S. N. Shirodhkar and U. V. Waghmare, *Phys. Rev. Lett.* **112**, 157601 (2014).
- [8] B. Radisavljevic, A. Radenovic, J. Brivio V. Giacometti, and A. Kis, *Nat. nanotech* **6**, 147 (2011).
- [9] A. Kuc, N. Zibouche, and T. Heine, *Phys. Rev. B* **83**, 245213 (2011).
- [10] H-P. Komsa and A. V. Krashennnikov, *Phys. Rev. B* **86**, 241201 (2012).

- [11] S. Tongay, H. Sahin, C. Ko, A. Luce, W. Fan, K. Liu, J. Zhou, Y-S Huang, H. Ching-Hwa , J. Yan, D. F. Ogletree, S. Aloni, J. Ji, S. Li, J. Li, F.M. Peeters, and J. Wu, *Nat. Comm.* **5**, 3252 (2014).
- [12] K. Dileep, B. Loukya, N. Pachauri, A. Gupta, and R. Datta, *J. Appl. Phys.* **116**, 103505 (2014).
- [13] K.Dileep, B. Loukya. P.Silwal, A. Gupta, and R. Datta, *J. Phys. D: Appl. Phys.* **47**, 405001 (2014).
- [14] M. Stoger-Pollach, H. Franco, P. Schattschneider, S. Lazar, B. Schaffer, W. Grogger, H.W. Zandbergen, *Micron* **37**, 396 (2006).
- [15] L. Gu, V. Srot, W. Sigle, C. Koch, P. van Aken, F. Scholz, S. B. Thapa, C. Kirchner, M. Jetter, and M. Rühle, *Phy. Rev. B* **75**, 195214 (2007).
- [16] S. Grimme, J. Antony, S. Ehrlich, and H. Krieg, *J. Chem. Phys.* **132**, 154104 (2010).
- [17] C. Ambrosch-Draxl and J. O. Sofo, *Comp. Phys. Comm.* **175**, 1 (2006).
- [18] U. Maitra, U. Gupta, M. De, R. Datta, A. Govindaraj, and C. N. R. Rao, *Angew. Chem. Int. Ed.***52**, 13057 (2013).
- [19] S. Yang, C. Wang, H. Sahin, H. Chen, Y. Li, S-S Li, A. Suslu, F. M. Peeters, Q. Liu, J. Li, and S. Tongay, *Nano Lett.* **15**, 1660 (2015).
- [20] Gmelin, *Gmelin handbook of inorganic and organometallic chemistry* (Springer-Verlag, Berlin, 1995).
- [21] J. N. Coleman, M. Lotya, A. O'Neill, S. D. Bergin, P. J. King, U. Khan, K. Young, A. Gaucher, S. De, R. J. Smith, I. V. Shvets, S. K. Arora, G. Stanton, H. Y. Kim, K. Lee, G. T. Kim, G. S. Duesberg, T. Hallam, J. J. Boland, J. J. Wang, J. F. Donegan, J. C. Grunlan, G. Moriarty, A. Shmeliov, R. J. Nicholls, J. M. Perkin, E. M. Grieverson, K. Theuwissen, D. W. McComb, P. D. Nellist, and V. Nicolosi, *Science* **331**, 568 (2011).
- [22] H-X Zhong, S. Gao, J-J. Shi, and Li Yang, *Phys. Rev. B* **92**, 115438 (2015).
- [23] S. Horzum, D. Çakır, J. Suh, S. Tongay, Y.-S. Huang, C.-H. Ho, J. Wu, H. Sahin, and F. M. Peeters, *Phys. Rev. B* **89**, 155433, 2014.
- [24] C. -H. Ho, *Cryst. Struct. Theory Appl.* **2**, 65 (2013).

Chapter 5

Understanding and diagnosis of native point defects in ZnO by HR-EELS

In this chapter, first, an attempt was made to understand green luminescence by core-loss EELS. Later it was realized that measurement of band gap through low-loss EELS in combination of theory calculation by mBJGGA method is more sensitive to correctly identify a particular native defect. The latter approach helped us to correctly assign the green luminescence to Schottky type-I defect.

*This work has been published in Journal of Applied Physics **109**, 063523 (2011), Physica Status Solidi (b) **252**, 1743 (2015) and Journal of Crystal Growth **410**, 69 (2015).*

5.1 Introduction

Wide band gap compound semiconductors e.g., GaN and ZnO show defect related secondary emission other than the band edge primary emission if the stoichiometry is not maintained during synthesis [1, 2]. This reduces the radiative efficiency of the devices [3]. For example, besides the usual UV emission from ZnO, defect related green emission has also been reported. Chemically synthesized ZnO nanocrystals exhibited broad and intense green luminescence in addition to the UV emission [4]. Green emission was reduced with increasing annealing temperature under oxygen atmosphere and explained in terms of reduction in oxygen vacancy defects (V_O) [5]. In literature, the assignment of the secondary emissions to a particular type of native point defect has been arbitrary [6-13]. The system may contain a single type of point defect or combination of point defects forming complex systems [13]. We need a set of tools to identify exact nature of defects and their relationship with the secondary emission. We are still addressing this issue in *our group* by combination of core-loss EELS, valence EELS, cathodoluminescence along with theoretically calculated band gap and electronic structure for possible set of point defect systems for the assignment. To begin with we have taken three different ZnO nanocrystal systems. Nanocrystals synthesized at room temperature, shows strong green emission peak. Green emission intensity reduces substantially when annealed at 200 °C and 400 °C in O environment (figure 5.1 (a)). We started the work with the core-loss spectroscopy/ELNES by HR-EELS. We wanted to see how the core loss spectra are different in three different systems and see if we can fingerprint the fine structure to a particular native defect type with the help of DFT calculation. So, our first job was to acquire both $O K$ and $Zn L_{3,2}$ edges from three different samples.

ELNES and its X-ray based counterpart, XANES have been used to study point defects in ZnO. Hsu *et al.* has reported appearance of pre-edge peaks in Zn K XANES in a Co doped ZnO annealed under Ar/H₂ atmosphere and assigned this pre-edge peaks to V_O , supported by FEFF based multiple scattering theory calculations [14]. Muller *et al.* reported that the $O K$ edge absorption peak and associated fine structures wash out with an increasing amount of V_O in SrTiO₃ thin film [15]. EELS has the advantage over XANES for its simplicity of acquisition. Also, experimentation can be easily performed at localized regions (down to a single atomic column) in a transmission electron microscope.

Later, it has been found out that the assignment of the correct point defect by core-loss EELS might not be conclusive and low-loss EELS is more sensitive to correctly identify a particular native defect along with the help of accurate band gap calculation by mBJGGA potential within Wien2k. The type of band gaps i.e. direct or indirect and the corresponding values of the green luminescence can be measured by experimental low-loss EELS band gap measurement and compared to the type and value calculated accurately by mBJGGA within Wien2k. This approach helped us to correctly assign the green luminescence to Schottky type-I defect. Additionally V_O is found to give blue luminescence at 2.78 eV [16].

5.2 Experimental details

ZnO nanocrystals were synthesized by a procedure already described in the literature [4]. As synthesized particles were annealed at 200 and 400 °C in oxygen flow of 500 SCCM (where SCCM denotes cubic centimeters per minute at standard temperature and pressure) for 10 h. The photoluminescence spectra of the nanocrystals were recorded with a Perkin–Elmer LS55 luminescence spectrometer. ELNES were acquired using a gun monochromator (both in image and diffraction mode) in a FEI-TITAN³™ 80–300 kV transmission electron microscope operating at 300 kV with an energy resolution better than 0.18 eV. In order to improve the signal over noise ratio, camera length and energy dispersion scale were reduced to 73 mm and 0.03 eV/pixel respectively. A Gatan imaging filter entrance aperture size of 1 mm was chosen which ensured high energy resolution during spectra acquisition. A near edge structure up to ~ 50 eV from the absorption edge for both $O K$ and $Zn L_{3,2}$. Low-loss HR-EELS acquisition and analysis were done as described in sections 1.4-1.6.

5.3 Calculation details

We calculated the density of states, band structure and ELNES (with TELNES2 program in Wien2k) with a full potential linear augmented plane wave basis to study the change in density of states with oxygen vacancy concentrations and respective ELNES spectra both for $O K$ and $Zn L_{3,2}$ edges. The generalized gradient approximation was employed with the Perdew-Burke-Ernzenhof (PBE) functional. Five cases were studied; (i) ZnO with no vacancies, (ii) 25% O vacancies simulated with a super cell of ZnO (four Zn, four O, $2 \times 1 \times 1$ unit cell) with one O atom removed, (iii) 12.5% O vacancies simulated with a super cell of ZnO (eight Zn, eight O, $2 \times 2 \times 1$

unit cell) with one O atom removed, (iv) 6.25% O vacancies simulated with a super cell of ZnO (16 Zn, 16 O, $2 \times 2 \times 2$ unit cell) with one O atom removed and (v) 6.25% Schottky defect simulated with a super cell of ZnO (16 Zn, 16 O, $2 \times 2 \times 2$ unit cell) with one Zn atom and one O atom removed. We used wurtzite structure with space group $P6_3mc$ generated with lattice parameters of $a = 3.2973 \text{ \AA}$ and $c = 5.2824 \text{ \AA}$ and atomic positions given by Zn ($2/3, 1/3, 0$) and O ($2/3, 1/3, u$), where $u = 0.3775$. The rest of the calculation parameters are as described in section 2.3.

The Zn $L_{3,2}$ ELNES is also simulated by FEFF 9.05 code for all possible types point defects and defect complexes [V_O , Zinc vacancy (V_{Zn}), Zinc interstitial (Zn_i), Oxygen interstitial (O_i), Oxygen antisite (O_{Zn}), Schottky type I defect ($V_{Zn}+V_{O-I}$; both vacancies in nearest neighbor), Zinc Frenkel defect ($V_{Zn}+Zn_i$) and Oxygen Frenkel defect (V_O+V_{Zn})] in ZnO. FEFF code is based on the Green function theory of multiple scattering. It is a real space calculation and is much faster than DFT. For FEFF calculation, the Hedin-Lundquist (HL) exchange correlation potential was used. The core hole was treated according to the ‘Final State rule’. A spherical cluster of 10 \AA radius was used for all calculation with absorbing atom at the center. The optimized ZnO lattice parameters from the Wien2k calculation were used for FEFF calculations.

5.4 Preliminary results based on core-loss EELS/ELNES

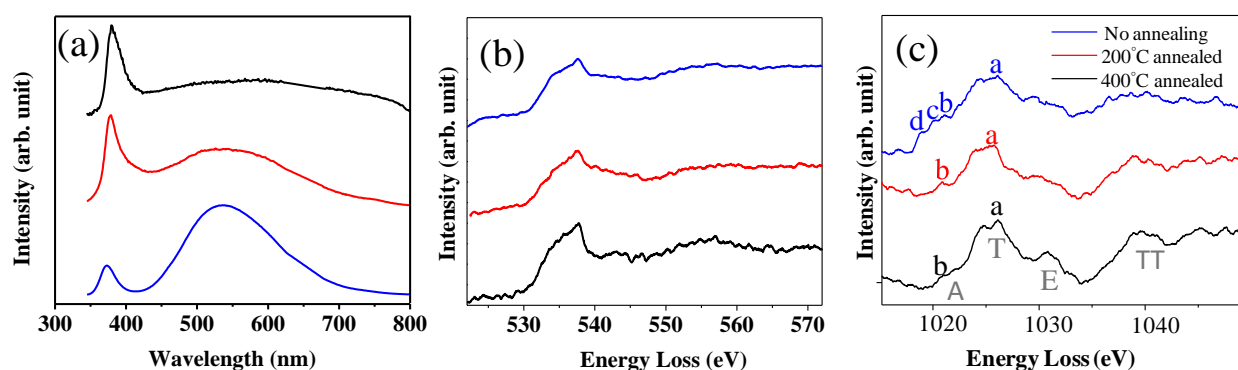


Figure 5.1. (a) Photoluminescence spectra of as synthesized (no annealing) ZnO nanocrystals and annealed at different temperatures (b) experimental O K ELNES and (c) experimental Zn $L_{3,2}$ ELNES. Copyright (2011) by American Institute of Physics [5].

We started the work with the core-loss spectroscopy/ELNES by HREELS. From the photoluminescence of three different ZnO nanocrystals (see figure 5.1 (a)), one can clearly

observe that green emission is quite intense and broad for an as-synthesized ZnO sample compared to the sample annealed at 200 °C. Whereas green emission disappeared significantly for the sample annealed at 400 °C in oxygen, this suggested that green emission may be related to oxygen deficiency in ZnO and quenched significantly by annealing that might have replenished oxygen in the ZnO lattice.

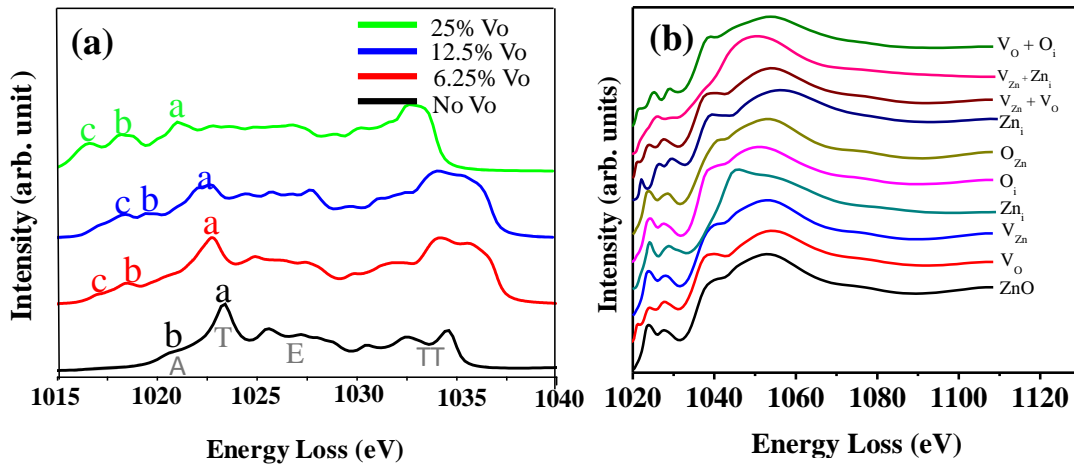


Figure 5.2. (a) DFT calculated ELNES by Wien2k for different percentages of V_o (Copyright (2011) by American Institute of Physics [5]) and (b) multiple scattering theory calculations by FEFF code for all types of native point defects in ZnO. 'Tick mark' is shown against the spectra showing pre-edge peaks.

In experimental ELNES spectra of $O K$ edge and $Zn L_{3,2}$ edge for three different samples are given in figure 5.1 (b) and figure 5.1 (c). In the $O K$ spectra, there are no appreciable changes at pre-edge features as a function of different annealing temperatures, but smearing of the fine features is observed for as synthesized sample. The absence of prominent pre-edge peaks is because the O atoms come only in the second co-ordination shell of any O vacancy and ELNES probes the local unoccupied density of states of the absorbing atom. In contrast, there are clear pre-edge features for the three samples in the $Zn L_{3,2}$ spectra. The four main expected peaks of ZnO are labeled A, T, E, and TT in figure 5.1 (c) according to molecular orbital theory [17]. The peak A is the transition to the unoccupied Zn $4s$ band. Peaks T and TT are transition to unoccupied Zn t_{2g} band hybridized with Zn $4p$. The peak E is the transition to the unoccupied e_g band. In addition to this, defect related pre-edge peaks (labeled as b, c etc.) appear for all the three nanocrystals. The relative peak height of b to a is increasing with increasing intensity of

green luminescence. There are also extra peaks like *c* and *d* etc. that come up for the as synthesized sample.

We have compared our experimental spectra with theoretical ELNES to get better insight into change in pre-edge structure with increasing oxygen vacancy defects in terms of change in the electronic density of states. Figure 5.2 (a) shows the theoretical ELNES spectra calculated by Wien2k of the *Zn L_{3,2}* edge of ZnO with different oxygen vacancy concentrations (i.e., no vacancy, 6.25%, 12.5%, and 25%) which shows the appearance of pre-edge peaks, whose number and intensity increased as a function of V_O concentrations. Therefore, we first assigned these pre-edge peaks to oxygen vacancies. Later, when we performed *Zn L_{3,2}* spectra for all types of possible native point defects and defect complexes in ZnO by multiple scattering theory calculations within the FEFF code (see figure 5.2 (b)), we learnt that this result might not be conclusive because there are four types of defects that can give similar pre-edge features in Zn *L_{3,2}*; (i) V_O , (ii) $V_{Zn}+V_{O-I}$, (iii) Zn_O and (iv) V_O+O_i . But previous calculations based on DFT have shown that Zn_O and V_O+O_i have very high formation energy and can be ruled out [8, 13]. Now, it is between one of V_O and $V_{Zn}+V_{O-I}$ which could be responsible for green luminescence. But core-loss spectroscopy/ELNES, which was the technique of first choice, fails to conclusively assign a particular type of native defect. This led to exploring other alternatives to address the issue.

5.5 Accurate assignment of the defect responsible for green luminescence by low-loss EELS

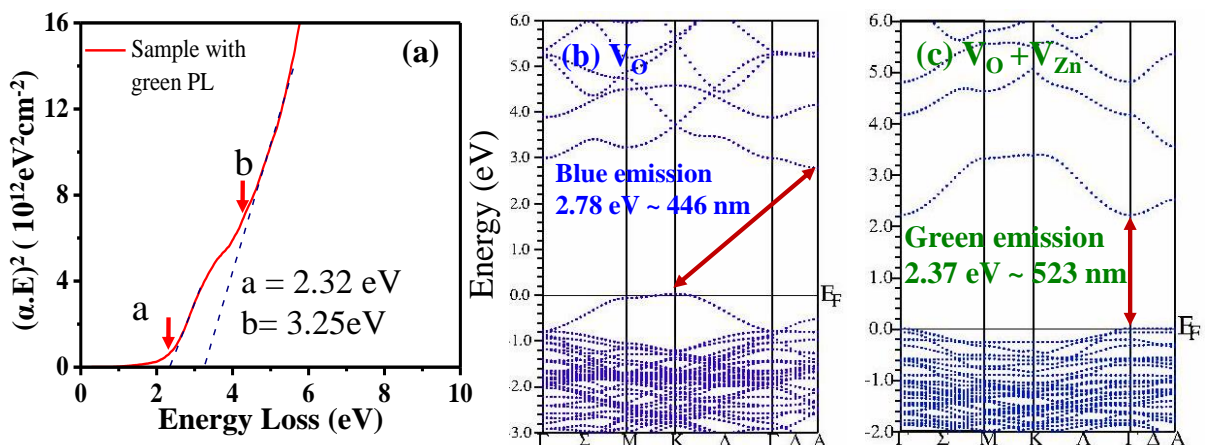


Figure 5.3. (a) Tauc plot from low-loss EELS for the sample with green luminescence (Copyright (2015) by Elsevier [18]), band structure calculated by mBJGGA for (b) V_O and (c) $V_{Zn}+V_{O-I}$ (Copyright (2015) by Wiley [16]).

We have taken a different approach, where the accurate type (direct or indirect) and energy value of the transition corresponding to the secondary emission can be measured by low-loss EELS and it can be compared with the accurate type (direct or indirect) and energy value of the transition calculated by mBJGGA potential within Wien2k. This method has the advantage over the method described in section 5.4 that we are comparing the numbers/values of band gap here, while the former method relies on pattern matching/finger printing. The Tauc plot for direct band gap ($(\alpha \cdot E)^2 \propto E$) for a sample with green luminescence is shown in figure 5.3 (a), which shows a direct transition corresponding to green luminescence (2.32 eV). Accurate band gap calculation by mBJGGA for 6.25% V_O shows that it is indirect band gap type and the transition corresponds to blue luminescence (2.78 eV) (see figure 5.3 (b)). But mBJ calculated transition for 6.25% V_{Zn+V_O-I} is direct type and corresponds to green luminescence (2.37 eV) (see figure 5.3 (c)) [16]. From this, we drew the conclusion that it is Schottky type I defect which is responsible for the green luminescence in ZnO.

5.6 Conclusions

In conclusion, we have learnt from our experience that measurement of optical band gaps and their types by low-loss EELS is a more sensitive and effective tool to identify the types of various point defects and related complexes in ZnO compared to core-loss EELS/ELNES which was the technique of first choice. This novel approach helped us to correctly assign the green luminescence to Schottky type-I defect and emission related to V_O at 2.78 eV.

5.7 Bibliography

- [1] U. Kaufmann, M. Kunzer, H. Obloh, M. Maier, Ch. Manz, A. Ramakrishnan, and B. Santic, *Phys. Rev. B* **59**, 5561 (1999).
- [2] S. Shionoya and W. H. Yen, *Phosphor Handbook* by Phosphor Research Society (Boca Raton, FL: CRC Press, 1997).
- [3] S. Nakamura and S. F. Chichibu, *Nitride Semiconductor Blue Lasers and Light Emitting Diodes* (Boca Raton, FL: CRC Press, 2000).
- [4] L. S. Panchakarla, Y. Sundarayya, S. Manjunatha, A. Sundaresan, and C. N. R. Rao, *Chem. Phys. Chem.* **11**, 1673 (2010).

- [5] K. Dileep, L. S. Panchakarla, K. Balasubramanian, U. V. Waghmare, and R. Datta, *J. Appl. Phys.* **109**, 063523 (2011).
- [6] D.C. Reynolds, D.C. Look, B. Jogai, J.E. Van Nostrand, R. Jones, and J. Jenny, *Solid State Commun.* **106**, 701 (1998).
- [7] A. F. Kohan, G. Ceder, D. Morgan, and C. G. Van de Walle, *Phys. Rev. B* **61**, 15019 (2000).
- [8] A. Janotti and C.G. Van de Walle, *Phys. Rev. B* **76**, 165202 (2007).
- [9] K. Vanheusden, C.H. Seager, W.L. Warren, D.R. Tallant, J. Caruso, M.J. Hampden-Smith, and T.T. Kostas, *J. Lumin.* **75**, 11 (1996).
- [10] K. Vanheusden, W. L. Warren, C. H. Seager, D. R. Tallant, J. A. Voigt, and B. E. Gnade, *J. Appl. Phys.* **79**, 7983 (1996).
- [11] F.H. Leiter, H.R. Alves, A. Hofstaetter, D.M. Hofmann, and B.K. Meyer, *Phys. Status Solidi b* **226**, R4 (2001).
- [12] F. Leiter, H. Alves, D. Pfisterer, N.G. Romanov, D.M. Hofmann, and B.K. Meyer, *Physica B* **340**, 201 (2003).
- [13] R. Vidya, P. Ravindran, H. Fjellvåg, B. G. Svensson, E. Monakhov, M. Ganchenkova, and R. M. Nieminen, *Phys. Rev. B* **83**, 045206 (2011).
- [14] H. S. Hsu, J. C. A. Huang, Y. H. Huang, Y. F. Liao, M. Z. Lin, C. H. Lee, J. F. Lee, S. F. Chen, L. Y. Lai, and C. P. Liu, *Appl. Phys. Lett.* **88**, 242507 (2006).
- [15] D. A. Muller, N. Nakagawa, A. Ohtomo, J. L. Grazul, and H. Y. Hwang, *Nature* **430**, 657 (2004).
- [16] R. Sahu, K. Dileep, D. S. Negi, K. K. Nagaraja, and R. Datta, *physica status solidi (b)* **8**, 1743 (2015).
- [17] T. Mizoguchia, M. Yoshiyaa, J. Lia, F. Obaa, I. Tanakab, and H. Adachia, *Ultramicroscopy* **86**, 363 (2001).
- [18] R. Sahu, K. Dileep, D. S. Negi, K. K. Nagaraja, S. Shetty, and R. Datta, *J. Cryst. Growth* **410**, 69 (2015).

Chapter 6

Valence band engineering of ZnO by S alloying

In this chapter we provide details on the epitaxial single phase thin film containing 17 at. % S can be grown on sapphire substrate using ZnO buffer layer. Valence band offset is raised by ~0.2 eV for this composition. The films are phase separated with more S content under the present growth condition. A band gap bowing parameter of 5.03 eV is obtained ZnO_{1-x}S_x alloy. ELNES of S L_{3,2} edge confirms that the S atoms substituted the O position in ZnO lattice. Li K and Ag M_{5,4} core loss spectra confirm that the dopants are incorporated both in the interstitial and substitutional positions thus preventing the film from p-type conductivity.

*This work is published in Journal of Alloys and Compounds **586**, 499 (2014) and Journal of Crystal Growth **402**, 124 (2014).*

6.1 Introduction

One of our strategies towards solving p-type doping problem in ZnO is via valence band engineering by S alloying as described in section 1.8. However, it is extremely difficult to retain S in ZnO and no report exists on the phase purity, crystallinity of the alloy along with acceptor dopants and their location in the lattice in thin film form; particularly by PLD. Among published literature on S:ZnO, Yoo et al. reported homogeneous solution only up to $x = 0.03$ by using two alternating pellets of ZnO and ZnS deposited by pulsed laser deposition (PLD) [1]. The deposition was done at 700 °C on *c*-plane sapphire substrate. Phase separation can be observed in terms of ZnS (0002) peak beyond this composition. Persson et al [2] studied the valence and conduction band offset as a function of S content and the corresponding ionization energy of N_O acceptor. ZnS_xO_{1-x} alloys were grown by atomic layer deposition (ALD) technique on glass substrate at 120 °C with varying S composition. Sample with $x = 0.48$ was weakly crystalline and had an amorphous background. Sample with $x = 0.71$ was completely amorphous. Optical characterization, ultraviolet photoelectron spectroscopy (UPS) and density functional calculations showed that the valence band offset increases strongly and conduction band increases weakly for low S concentration and this reverses for large S content. Single phase $ZnO_{1-x}S_x$ alloys in the composition range 0.05 - 0.9 are reported by spray pyrolysis method [3]. But the structure changes from wurtzite to cubic beyond $x = 0.44$. This chapter contains results based on our attempt to grow single phase epitaxial ZnS_xO_{1-x} and $(Ag, Li)_{0.01}:Zn_{0.99}S_xO_{1-x}$ alloy films by PLD. We observe that epitaxial single phase thin film containing up to 17 at. % of S has been grown on sapphire substrate by employing ZnO buffer layer grown at low temperature (400 °C). The phase separation can be controlled and S content can be improved by growing $ZnO_{1-x}S_x$ on the ZnO buffer layer. A band gap bowing parameter of 5.03 eV is obtained, which is comparable to the bowing parameter, 4.93 eV, calculated by mBJGGA in Wien2k. ELNES of $L_{3,2}$ confirms that S atoms substituted in the O position in ZnO lattice. *Li K* and *Ag M_{5,4}* core-loss spectra confirm that the dopants are incorporated both in the interstitial and substitutional positions forming donor-acceptor complexes preventing the doped films from stable p-type conductivity. We found later the off-stoichiometric BN_{1-x} is good dopant compared to Ag and Li in terms of formation of donor-acceptor complexes [4].

6.2 Experimental details

ZnO and ZnS powders were mixed together for the $\text{ZnO}_{1-x}\text{S}_x$ alloy target pellet. A second alloy (Li,Ag): $\text{ZnO}_{1-x}\text{S}_x$ target pellet was prepared by mixing Ag_2O and Li_2O together with ZnO and ZnS. The pellets were vacuum sealed and sintered for 6 hours at 720 °C. We sintered the pellets in a vacuum sealed tube because they were found not to retain any S if sintered under ambient pressure. KrF excimer laser with wavelength of 248 nm and an energy fluence of 1.5 J cm^{-2} was used to ablate the target pellets. Pellet to substrate (*c*-plane sapphire, miscut $\pm 0.5^\circ$, MTI corporation), distance was set to be ~5 cm. The growth scheme was according to a three step growth described in section 1.9. The temperature of the final step growth was reduced from 800 °C to 600 °C which prevented escape of S from the film. All the samples were grown under resistive type growth condition where oxygen partial pressure was 0.1 Torr throughout the growth except during film deposition where pressure is kept at 10^{-5} Torr, in order to ensure a two dimensional growth.

TEM samples are prepared as described in section 2.2. The electron diffraction patterns and the TEM bright field images were recorded in a FEI TECNAI 200kV transmission electron microscope. Energy dispersive spectroscopy (EDS) was performed in a TEM for the films to check for S and other impurity incorporation. The HREELS spectra were recorded in a FEI TITAN³™ 80-300kV transmission electron microscope as described in section 1.4 to 1.6.

6.3 Calculation methods

Theoretical calculation of the density of states and electronic structure of ZnO, ZnS, intermediate alloys and the alloy doped with Ag and Li were carried out using WIEN2k code. Super cells are created and simulated corresponding to various composition of $\text{ZnO}_{1-x}\text{S}_x$ (with $x = 0, 0.125, 0.25, 0.5, 0.75, 0.875, 1$) as well as for doped $\text{Ag}_{0.0625}\text{Zn}_{0.935}\text{O}_{0.75}\text{S}_{0.25}$ and $\text{Li}_{0.0625}\text{Zn}_{0.935}\text{O}_{0.75}\text{S}_{0.25}$ alloys. The relaxed lattice parameters for ZnO were $a = 3.2973 \text{ \AA}$ and $c = 5.2824 \text{ \AA}$. For ZnS they were $a = 3.8624 \text{ \AA}$ and $c = 6.2659 \text{ \AA}$. The k-mesh was $12 \times 12 \times 6$ for ZnO and ZnS and it was reduced proportionally for larger super cells. The lattice parameters were relaxed for the alloys as well. The rest of the parameters for calculations are already provided in section 2.3.

The *Ag M_{5,4}* EXELFS (Extended Energy Loss Fine Structure) and *Li K* ELNES were calculated by FEFF 9.05 code. FEFF code is based on the Green function theory of multiple scattering. It is a real space calculation unlike DFT. It can calculate EXELFS spectra which correspond to the energy losses above 50 eV from the absorption edge. Electron in a crystal with kinetic energy more than 50 eV behaves like a free electron. Weak oscillations in the spectra can arise from interference between outgoing spherical waves with the reflected waves from the neighboring atoms. This is directly correlated with the radial distribution function. Depending on the position of the absorbing atom (substitutional and interstitial Ag atoms in ZnO crystal) the ripples in the spectra will be different. We studied *Li K* using FEFF code because in Wien2k all the 3 electrons in Li are treated as valence electron with the energy separation of -6 Ry between core and valence level (which is required for ZnO). This makes the core-hole effect (this is required for the proper matching with the experimental spectra) consideration impossible. For FEFF calculation, the Hedin-Lundquist (HL) exchange correlation potential was used. The core hole was treated according to the ‘Final State rule’. A spherical cluster of 10 Å radius was used for all calculation with absorbing atom at the center. We simulated the O rich phase by replacing only one of the O atoms by S in the first co-ordination shell of the absorbing atom. The optimized ZnO lattice parameters from the Wien2k calculation were used for FEFF calculations.

6.4 Results and discussions

Our ultimate aim is to grow single phase, epitaxial ZnO_{1-x}S_x alloy along with Ag, Li dopants. We started the growth with a targeted composition of ZnO_{0.7}S_{0.3} directly grown on sapphire substrate (Sample S1). The schematic of the growth schedule, TEM bright field image with $g = 0002$ and the large area diffraction pattern along $\langle 01-10 \rangle$ zone axis of sapphire for sample S1 have been shown in figure 6.1 (a) – (c), respectively.

The surface of the sample S1 is very smooth as seen in cross sectional TEM image. TEM diffraction pattern shows streaks instead of spots and this is due to the tilts of different crystals with respect to the c -axis of sapphire. There are four distinguishable intensity streaks from the sample along the c direction. The four streaks correspond to four different phases of ZnS_xO_{1-x} having wurtzite structure. The lattice parameters (d_{0002}) of these four different phases have been determined with respect to sapphire d_{0006} . From this lattice parameter information, Vegard’s law

has been applied to determine the composition of these phases and their relative volume fractions from the intensity [5]. The ideal c lattice parameters of ZnO and ZnS were taken as 5.203 Å and 6.2605 Å, respectively [6, 7]. The predominant phase for this sample is found to be $\text{ZnO}_{0.83}\text{S}_{0.17}$ with a volume fraction $\sim 52\%$. This gives the indication that $x = 0.17$ may be the upper limit to grow epitaxial single crystalline alloy under the growth condition we employed. The average composition was found to be $\text{ZnO}_{0.79}\text{S}_{0.31}$ which closely matches with TEM-EDS compositional analysis.

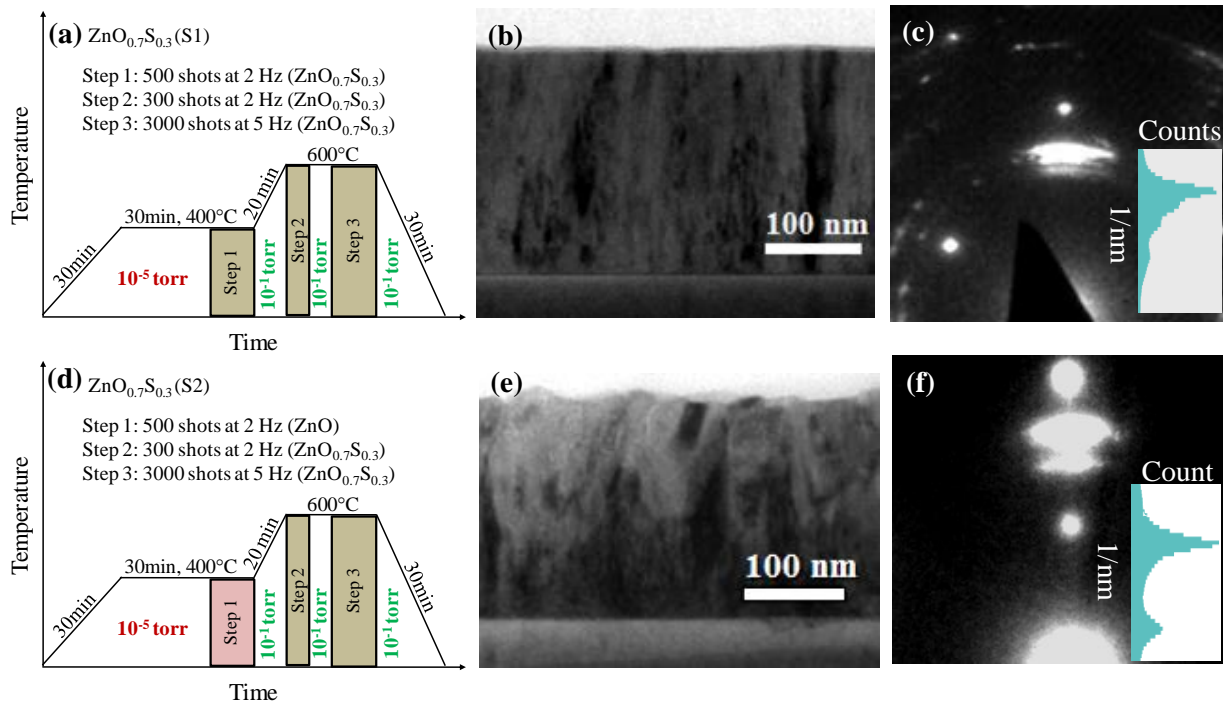


Figure 6.1. (a) and (d) Schematic of the growth schedule, (b) and (e) are TEM bright field images under two beam condition and. (c) and (f) are the electron diffraction pattern along $\langle 11-20 \rangle$ zone axis for samples S1 and S2 respectively. Insets show the intensity profiles along $\langle 0002 \rangle$ reciprocal vector. (Copyright (2014) by Elsevier [15]).

In order to study the effect of buffer layer on the phase separation of ZnO_{0.7}S_{0.3} alloy a film (sample S2) is grown on top of a ~ 8 nm thick ZnO layer. The growth scheme is given in figure 6.1 (d). But it is observed that the film showed two streaks in diffraction pattern (figure 6.1 (f)) corresponding to two phases, one O-rich (ZnO_{0.88}S_{0.12}) and another S-rich (ZnO_{0.11}S_{0.89}) phase. Therefore it is evident that the epitaxial single phase ZnO_{0.7}S_{0.3} alloy cannot be grown either directly on sapphire or on top of a ZnO template in PLD under the growth condition we employed.

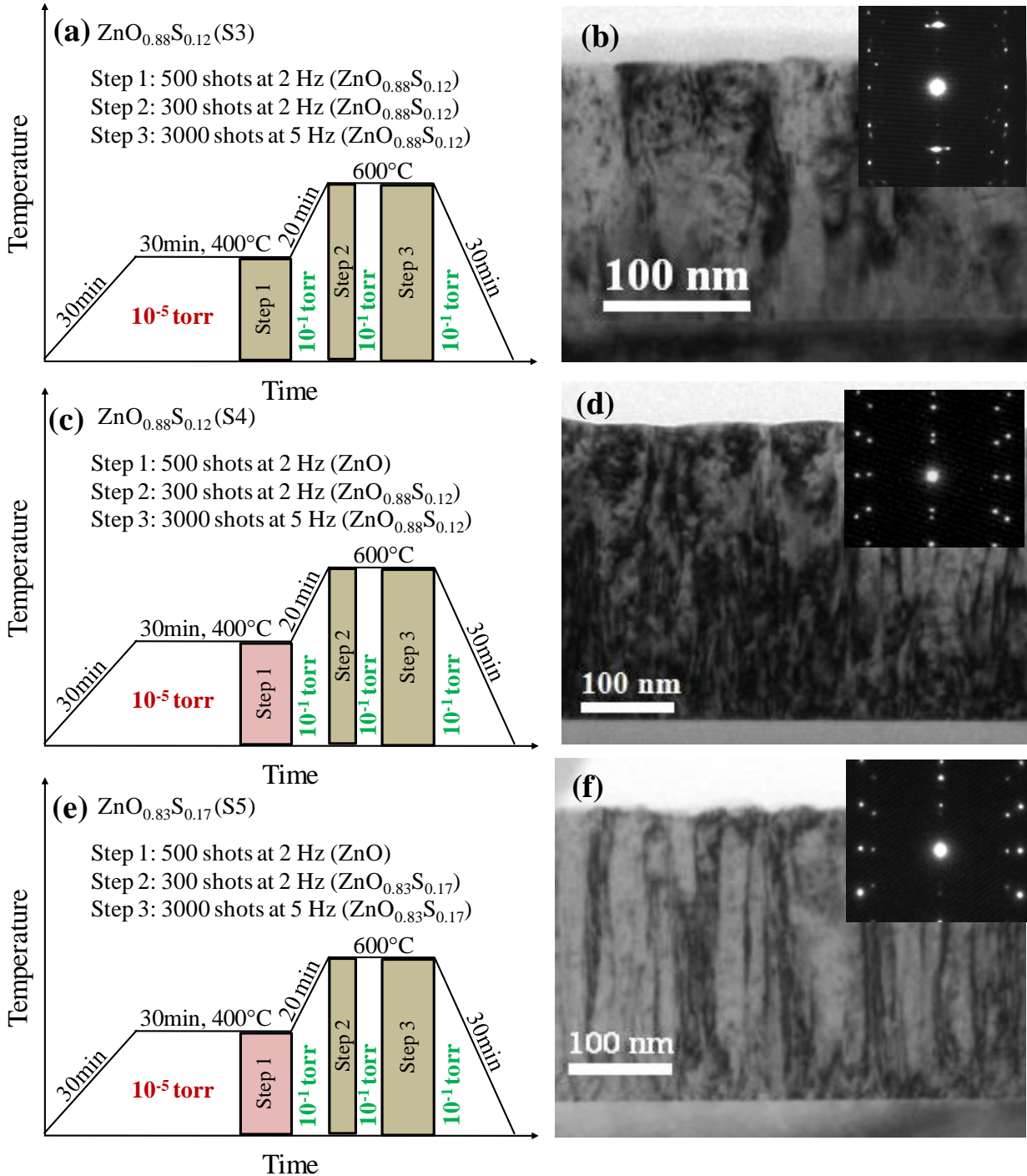


Figure 6.2. (a), (c) and (e) Schematic of the growth schedule of samples S3, S4 and S5, (b), (d) and (f) are TEM bright field images under two beam conditions of samples S3, S4 and S5, insets show the corresponding diffraction pattern along $\langle 11-20 \rangle$ of ZnO. (Copyright by Elsevier [16]).

In order to investigate the limit on S concentration at which we can obtain epitaxial film (or single crystalline film) without any observable tilt in diffraction pattern, systematic experiment

on growth, structural and optical characterizations were performed for $\text{ZnO}_{1-x}\text{S}_x$ for $x=0.12, 0.17$ with and without using ZnO as buffer layer. $\text{ZnO}_{0.88}\text{S}_{0.12}$ film directly grown on sapphire (S3) shows a single phase but with tilted grains with respect to 0001 direction (figure 6.2 (b)). The S content measured from EDS is just 2%, much below the targeted content. The c -lattice parameter measured from diffraction pattern shows the same value as that of ZnO ($\sim 5.2 \text{ \AA}$). The same alloy, $\text{ZnO}_{0.88}\text{S}_{0.12}$ when grown on a ZnO buffer, the film was obtained to be epitaxial single phase without any tilt (sample S4, figure 6.2 (d)). The sulfur content measured by Vegard's law and EDS spectroscopy are 7% and 5%, respectively, which indicates higher incorporation of S compared to direct growth on sapphire. $\text{ZnO}_{0.83}\text{S}_{0.17}$ alloy grown on ZnO template (S5) is also shown to be epitaxial single phase without any tilt (figure 6.2 (f)). The alloy composition obtained by Vegard's law and EDS spectroscopy is $\text{ZnO}_{0.87}\text{S}_{0.13}$ and $\text{ZnO}_{0.84}\text{S}_{0.16}$ respectively.

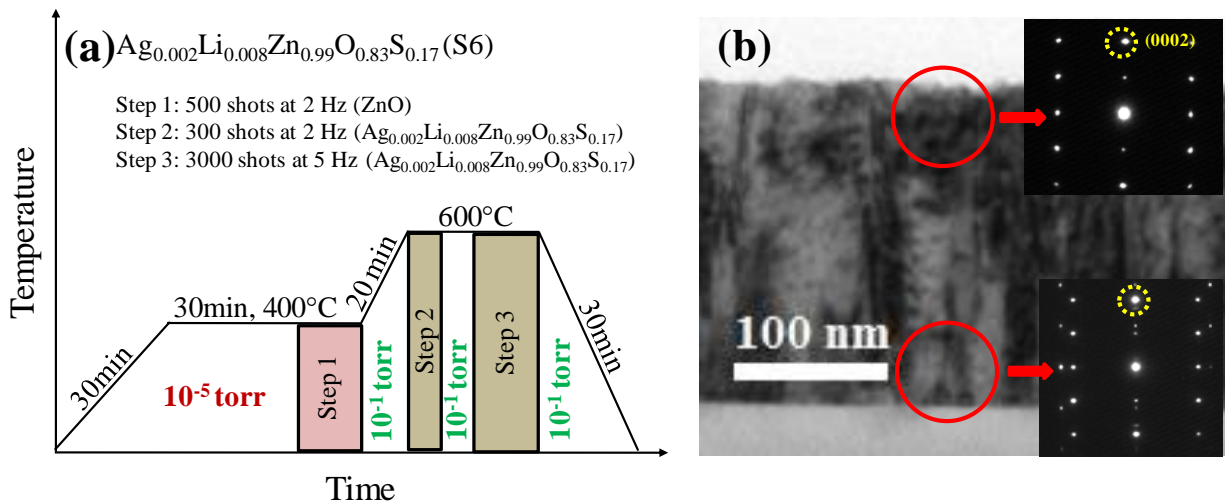


Figure 6.3. (a) Schematic of the growth schedule of samples S6 (b) TEM bright field images under two beam conditions of samples S6, Insets show the corresponding diffraction pattern along $\langle 11-20 \rangle$ of ZnO. (Copyright (2014) by Elsevier [16]).

Effect of addition of acceptor dopants on the epitaxy and phase separation has also been investigated. We present here the effect of acceptor dopants on the phase separation of one S composition (17 at. %). We have observed that the $\text{ZnO}_{0.83}\text{S}_{0.17}$ film when grown on ZnO buffer layer with 1% of (0.2 % Ag, and 0.8 % Li) dopants (Sample S5), a S rich phase was formed ($\text{ZnO}_{0.18}\text{S}_{0.82}$) near the interface between the ZnO:S film and the ZnO buffer but a single crystalline film $\text{ZnO}_{0.88}\text{S}_{0.12}$ is formed above that (figure 6.3 (b)).

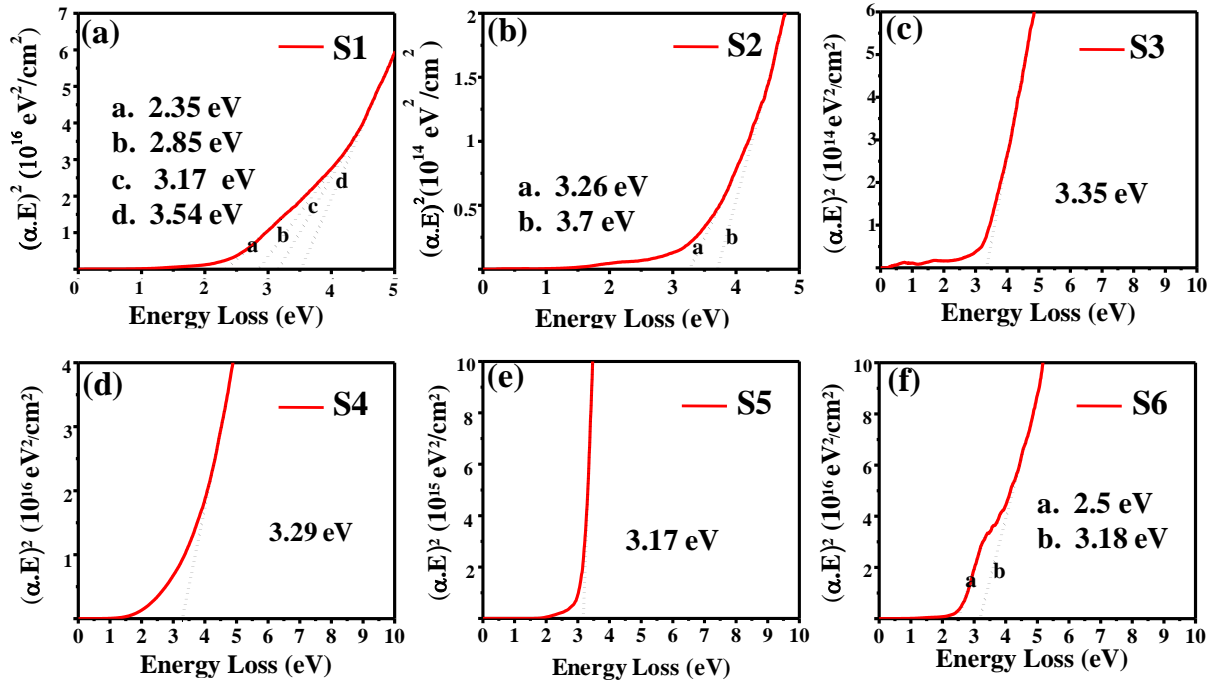


Figure 6.4. (a)-(f) The band gap of samples S1 to S6 obtained by low loss EELS respectively. The values obtained from each sample are shown in the respective figures. (Copyright (2014) by Elsevier [16]).

The band gap of various samples S1 to S6 (shown in figure 6.4 (a) to (f) respectively) have been measured by using high resolution electron energy loss spectroscopy. The procedure for band gap measurement is as described in sections 1.4 to 1.6. The band gap value measured from the four phases of sample S1 are 3.17 eV, 2.85 eV, 2.35 eV, and 3.54 eV from the $\text{ZnO}_{0.83}\text{S}_{0.17}$, $\text{ZnO}_{0.72}\text{S}_{0.28}$, $\text{ZnO}_{0.51}\text{S}_{0.49}$ and $\text{ZnO}_{0.15}\text{S}_{0.85}$ phases respectively. The sample S2 shows two band gaps at 3.26 eV for the O rich phase ($\text{ZnO}_{0.88}\text{S}_{0.12}$) and 3.7 eV for the S rich phase ($\text{ZnO}_{0.11}\text{S}_{0.89}$). Sample S3 shows a band gap at 3.35 eV, corresponding to the $\text{ZnO}_{0.98}\text{S}_{0.02}$ phase. Sample S4 shows band edge absorption at 3.29 eV (From the $\text{ZnO}_{0.93}\text{S}_{0.07}$ phase). Sample S5 shows single band gap absorption at 3.17 eV, the absorption by $\text{ZnO}_{0.83}\text{S}_{0.17}$ alloy. Applying Vegard's law for band gap for all the alloys in these samples, one obtains a band bowing parameter of ~ 5 eV. Sample S6 shows band gap absorption at 3.18 eV and another one is found at 2.5 eV. This later value must be the effect of 1% (Ag, Li) dopants in the film. The film is found to be phase separated into two phases at the interface between towards the film – template interface.

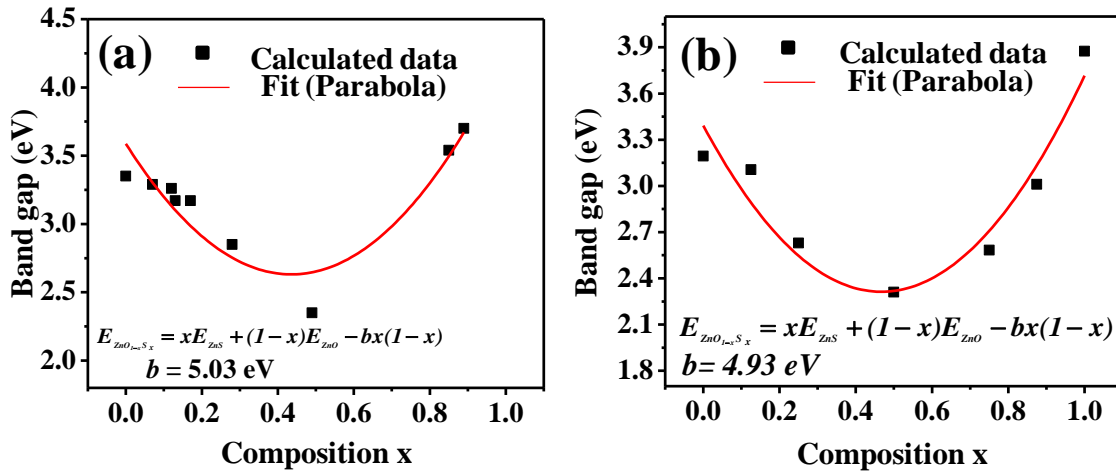


Figure 6.5. The composition of sulfur content from each samples plotted against their band gap (a) for experimental band gap value and (b) for calculated band gap values. The data points are fit with parabolic curve. (Copyright (2014) by Elsevier [15]).

From this data set one can calculate band gap bowing parameter according to Vegard’s law (figure 6.5); [5]

$$E_g (ZnO_{1-x}S_x) = xE_g (ZnS) + (1-x)E_g (ZnO) - b(1-x)x$$

Where E_g is the band gap, x is in at. % and b is the bowing parameter. The extreme values of band gaps corresponding to $E_g (ZnO)$ and $E_g (ZnS)$ were taken as 3.44 eV and 3.86 eV respectively [8, 9].

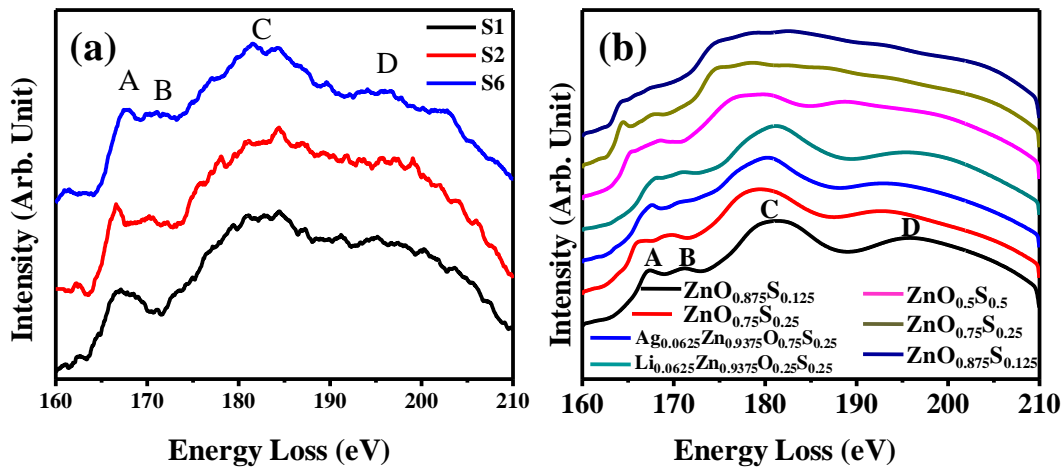


Figure 6.6. S $L_{3,2}$ spectra for samples S1 S2 and S3. S when substitute O in the ZnO lattice has 4 characteristic peaks which are well reproduced by different $ZnO_{1-x}S_x$. (a) The experimental spectra are well supported by (b) theoretical ELNES spectra. (Copyright (2014) by Elsevier [15]).

Figure 6.6 displays the experimental spectra of $S L_{3,2}$ together with calculated spectra for the alloys. Theoretical $S L_{3,2}$ spectra for $ZnO_{1-x}S_x$ (O substituted with S) matched well with experimental spectra. Core hole effect consideration was found not necessary for comparison with experimental spectrum for $S L_{3,2}$. This shows that S has in fact substituted O in the phases and no other phases like ZnS, SO_2 and sulphates are present. $S L_{3,2}$ peak showed four peaks indicating S has substituted O in the lattice.

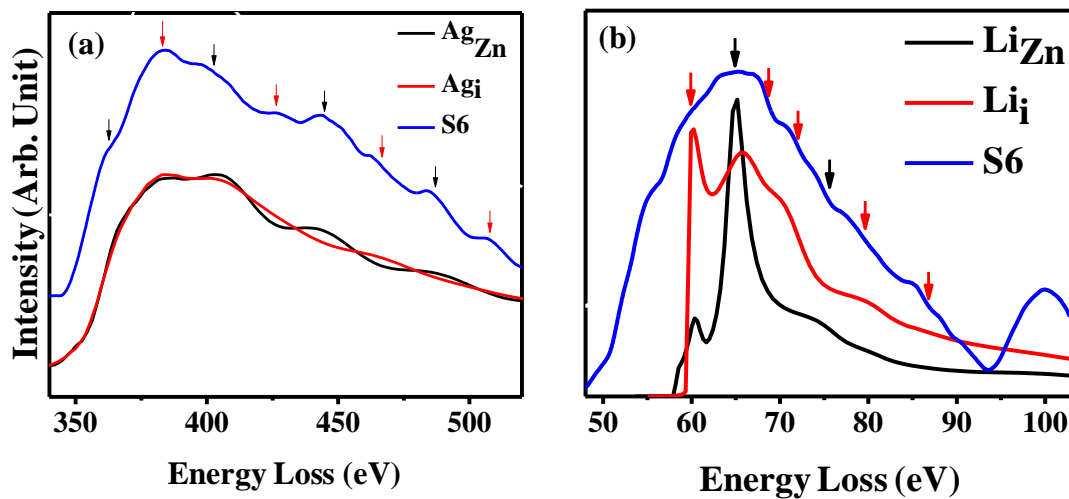


Figure 6.7. (a) The experimental (a) Ag $M_{5,4}$ EXELFS (b) Li K ELNES for samples S6. The appearance all peaks (indicated by arrows) is well reproduced only when Ag $M_{5,4}$ EXELFS and Li K ELNES spectra respectively calculated by FEFF 9.05 for substitutional and interstitial positions are superimposed.

The Ag $M_{5,4}$ ELNES spectra were recorded (in the first 50 eV from the absorption edge) for samples S6 and S3. They are broad and devoid of distinguishable fine structures. So we studied the Extended Energy Loss Fine Spectra (EXELFS). The spectra are given in figure 6.7 (a). The spectra show eight distinguishable peaks. We simulated the Ag $M_{5,4}$ EXELFS spectra in FEFF 9.05 code both with Ag in the substitutional (Ag_{Zn}) and Ag in the octahedral interstitial (Ag_i) position. Ag_{Zn} is tetrahedrally coordinated and Ag_i is octahedrally coordinated to O atom. When both spectra, with Ag_{Zn} and Ag_i , are superimposed, it gave one to one correspondence with the eight peaks in the experimental spectra (figure 6.7 (a)). This gives us the indication that Ag partially occupies substitutional and interstitial positions. Previous reports based on DFT calculations show that the formation energy of Ag_i donors in ZnO is very high (3eV and 4.5 eV in 2 different reports) and the compensation of p -type carriers will be inefficient [10, 11]. Huang et al, [12] by DFT calculations, found that both Li_i and Ag_i , once they are introduced in ZnO

lattice, are very stable. Channeling effect experiments of β^- particles emitted from radioactive Ag^+ ions implanted in ZnO show that Ag occupies Ag_{Zn} position after implantation [13]. But the Ag atoms moved to a quasi-interstitial position with a displacement of 0.2 to 0.5 Å from ideal Ag_{Zn} position following a vacuum annealing at 600 °C. Except for these, to the best of our knowledge, there are no experimental reports suggesting identification of Ag_i in ZnO or $\text{ZnO}_{1-x}\text{S}_x$ alloy. Also, EXELFS spectra were calculated for Ag_{Zn} and Ag_i in combination with the most dominant native point defects (V_O , V_{Zn} and Zn_i) in the first co-ordination shell. None of these spectra gave one to one agreement with the experimental spectra obtained.

Li K ELNES spectra analysis also indicates that Li occupies both interstitial and substitutional position in the lattice as well (figure 6.7 (b)). Also there is experimental report showing the simultaneous presence of Li_{Zn} and Li_i in ZnO lattice [14]. The experimental spectrum is matched best when calculated spectra (Fig. 9(b)) for both interstitial and substitutional Li in O-rich phase were superimposed.

The above results show that the PLD growth technique might pose a limit on S content (i.e. ~ 17 at. %) for which one can obtain a single phase and single crystalline film. We tried to incorporate high amount of Ag, Li dopants with the aim to overcome any self-compensation effect by native point defects. But it is found that with this high amount of dopants, incorporation occurs both in the substitutional and interstitial position.

6.5 Conclusion

In conclusion, we have found that epitaxial single crystalline thin film containing up to 17 at. % S can be grown on sapphire substrate using ZnO template layer which allowed the valence band offset to be raised by ~0.2 eV. The phase separation can be controlled and S content can be improved by growing $\text{ZnO}_{1-x}\text{S}_x$ layer on ZnO template layer. A band gap bowing parameter of 5.03 eV is obtained. For $\text{ZnO}_{1-x}\text{S}_x$ alloy. ELNES of *S L*_{3,2} confirms that S atoms substituted in the O position in ZnO lattice. *Li K* and *Ag M*_{5,4} core-loss spectra confirm that the dopants are incorporated both in the interstitial and substitutional positions forming donor-acceptor complexes, rendering Ag and Li not ‘good dopants’ for obtaining stable *p-type* conductivity in ZnO. Later we found out that the off-stoichiometric BN_{1-x} is a good dopant for stable *p-type* conductivity in ZnO [4]. The details of this work can be seen in chapter 7.

6.6 Bibliography

- [1] Y. Z. Yoo, Z. W. Jin, T. Chikyow, T. Fukumura, M. Kawasaki, and H. Koinuma, *Appl. Phys. Lett.* **81**, 3798 (2002).
- [2] C. Persson, C. P. Bjorkman, J. Malmstrom, T. Torndahl, and M. Edoff, *Phys. Rev. Lett.* **97**, 146403 (2006).
- [3] R. R. Thankalekshmi and A. C. Rastogi, *J. Appl. Phys.* **112**, 063708 (2012).
- [4] R. Sahu, H. B. Gholap, G. Mounika, K. Dileep, B. Vishal, S. Ghara, and R. Datta, *Phys. Status Solidi B*, 1–5 (2015)/ DOI 10.1002/pssb.201552625.
- [5] B. K. Meyer, A. Polity, B. Farangis, Y. He, D. Hasselkamp, T. Krämer, and C. Wang, *Appl. Phys. Lett.* **85**, 4929 (2004).
- [6] R. R. Reeber, *J. Appl. Phys.* **41**, 5063 (1970).
- [7] R. R. Reeber and G. W. Powell, *J. Appl. Phys.* **38**, 1531 (1967).
- [8] A. S. Mohammadi, S. M. Baizae, and H. Salehi, *World Appl. Sci. J.* **14**, 1530 (2011).
- [9] M. Oshikiri and F. Aryasetiawan, *Phys. Rev. B* **60**, 10754 (1999).
- [10] C. H. Park, S. B. Zhang, and S. Wei, *Phys. Rev. B* **66**, 073202 (2002).
- [11] O. Volnianska, P. Boguslawski, J. Kaczkowski, P. Jakubas, A. Jezierski, and E. Kaminska, *Phys. Rev. B* **80**, 245212 (2009).
- [12] G. Huang, C. Wang, and J. Wang, *J. Phys.: Condens. Matter* **21**, 345802 (2009).
- [13] U. Wahl, E. Rita, J.G. Correia, T. Agne, E. Alves, and J.C. Soares, *The ISOLDE Collaboration, Superlattices and Microstructures* **39**, 229 (2006).
- [14] Z. Zhang, K. E. Knutsen, T. Merz, A. Y. Kuznetsov, B. G. Svensson, and L. J. Brillson, *Appl. Phys. Lett.* **100**, 042107 (2012).
- [15] K. Dileep, and R. Datta, *J. Alloys. Compd.* **586**, 499 (2014).
- [16] K. Dileep, R. Sahu, K. K. Nagaraja, and R. Datta, *J. Cryst. Growth* **402**, 124 (2014).

Chapter 7

Conclusions and future perspectives

This chapter provides notes on the important conclusions drawn from the present thesis along with an overview on the future of HR-EELS as a powerful tool and our future focus towards improving p-type carrier concentration and mobility in ZnO by combining valence band engineering with non-stoichiometric BN_{1+x} co-doping.

7.1 Future of HR-EELS

Future of HR-EELS is extremely bright with ever increasing focus on nano and near atomic scale exploitation of materials functionalities. There have been recent developments in (1) monochromator design, (2) an ultra-bright cold field emission electron gun, aberration-corrected optics and a monochromator design which together maximized the intensity of the monochromated electron probe and (3) increasing the energy dispersion of the spectrometer to 1 meV per channel, and developing operating modes that minimize ZLP tails due to aberrations and stray scattering which allowed an energy resolution as good as 9 meV (figure 7.1) [1, 2]. With this high resolution, not only the fine features of the optical absorption spectra but also vibrational spectroscopy can be performed. Or in other words, phonon modes will also be accessible at atomic and near atomic scale. For example, single particle specific or a single point/line defect specific vibrational spectroscopy can also be performed. This opens a new avenue to understand the materials at atomic and nanoscale. The observation of vibrational peaks due to hydrogen in TiH_2 is very interesting. In TiH_2 , hydrogen is mobile and bound only weakly, which results in the relatively low vibrational energy of 147 meV for hydrogen. Ultra high resolution provided by the new design also enabled to observe the peak due to this vibration (see figure 7.2 (d)) [2].

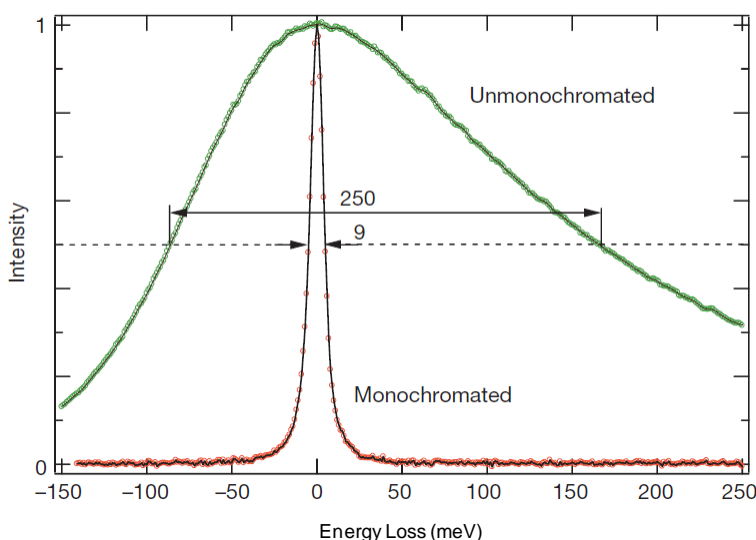


Figure 7.1. Monochromated zero loss peak (ZLP) with a resolution of 9 meV wide (full-width at half-maximum, FWHM) compared to the energy distribution of an unmonochromated beam produced by the system's cold field emission electron gun. Copyright (2014) by Nature Publishing Group [2].

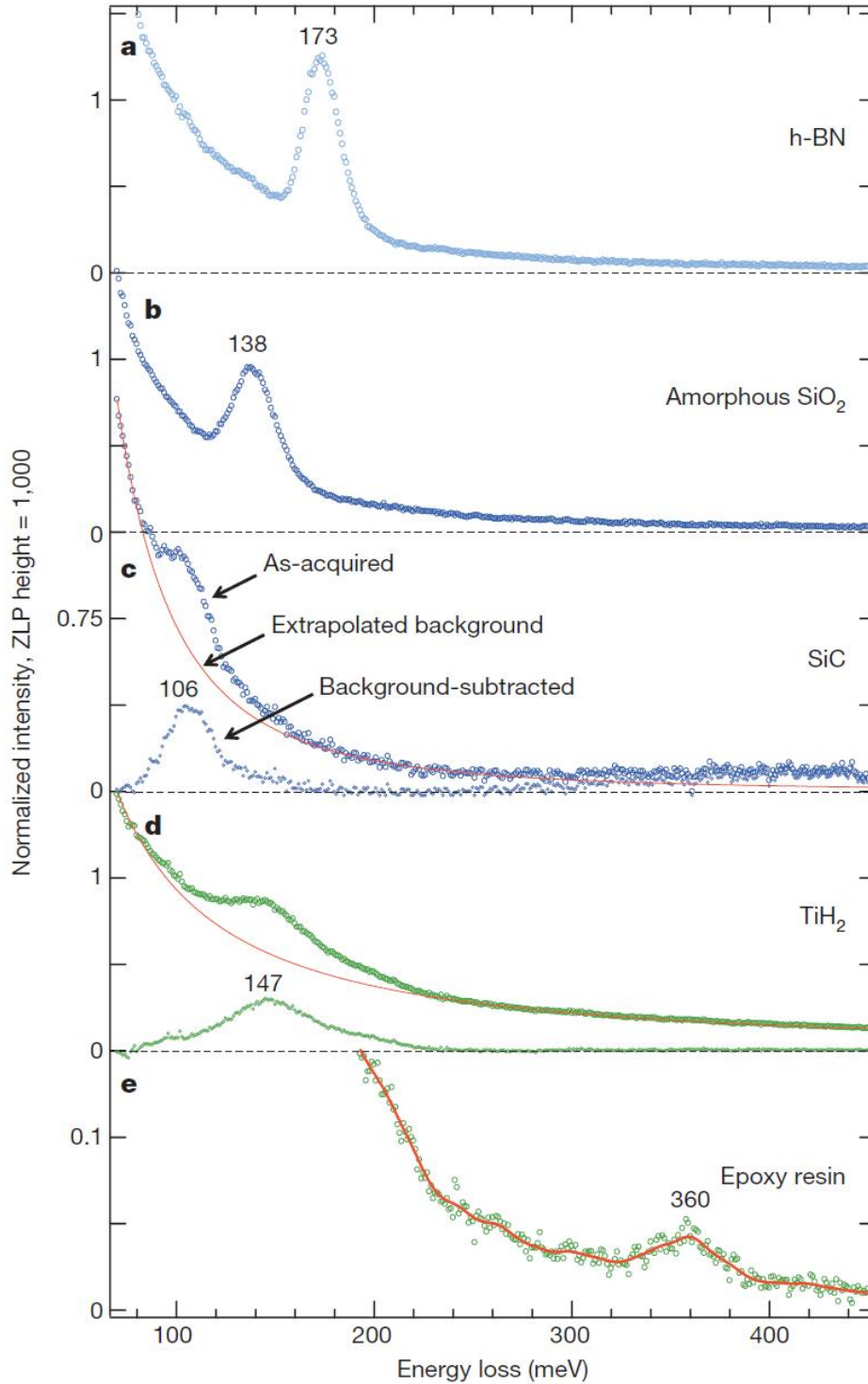


Figure 7.2. Vibrational spectra measured by low-loss EELS from various materials like (a) h-BN, (b) amorphous SiO₂, (c) SiC, (d) TiH₂ and (e) epoxy resin. Copyright (2014) by Nature Publishing Group [2].

7.2 Preliminary success in *p*-type doping of ZnO

Preliminary success in *p*-type doping of ZnO has been achieved in *our laboratory* by off-stoichiometric B and N *co-doping* in ZnO by PLD by following the *r-type* growth scheme described in section 1.9 [3]. A carrier concentration of $\sim 3 \times 10^{16} \text{ cm}^{-3}$ and a mobility of $10 \text{ cm}^2/\text{V.s}$ have been achieved (figure 7.3 (a)). The intensity of the peaks due to defect emission reduced significantly for the *p*-conducting sample. The *p*-type conductivity is found to be stable and the results could be reproduced even nine months after the growth. We have found that B and N are incorporated in Zn and O sites respectively but in a *non-stoichiometric* (BN_{1+x}) fashion, which resulted in stable *p*-type conductivity.

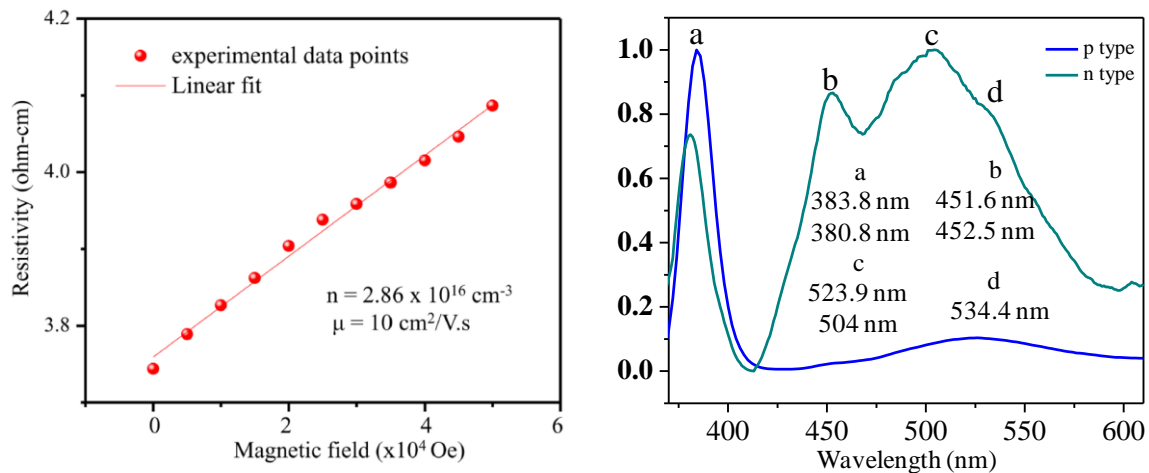


Figure 7.3. (a) Resistivity *v* magnetic field plot shows a positive slope indicating *p*-type conductivity. (b) Cathodoluminescence spectra for both *p*-type and *n*-type samples show significant reduction in defect emission peaks in the *p*-type sample. (Copyright (2015) by Wiley [3]).

DFT calculations also show that B, N *co-doping* is more stable in ZnO lattice than acceptor-donor complex formation or incorporation as individual dopants (see table 7.1). So BN is a ‘good dopant’ for stable *p*-type conductivity in ZnO. But B and N incorporation in a *stoichiometric* fashion does not lead to *p*-type conductivity. Accurate band gap calculations show that BN in a *non-stoichiometric* fashion can lead to *p*-type conductivity and has cohesive energy comparable to *stoichiometric* BN *co-doping* (see table 7.1).

Table 7.1. Different configurations of B and N dopants in ZnO and their corresponding cohesive energies and band gaps.

Dopant/ dopant complex	Cohesive energy (eV/atom)	Band gap (eV)
B _{Zn}	4.38	<i>n</i> -type metallic
B _i	4.23	<i>n</i> -type metallic
N _O	4.39	2.86
B _{Zn} +N _O	4.57	2.14
B _{Zn} +N _{2(O)}	4.55	<i>p</i> -type metallic

Our future focus will be combining both valence band engineering by S and Te doping and BN *non-stoichiometric co-doping* to improve carrier concentration and mobility in ZnO.

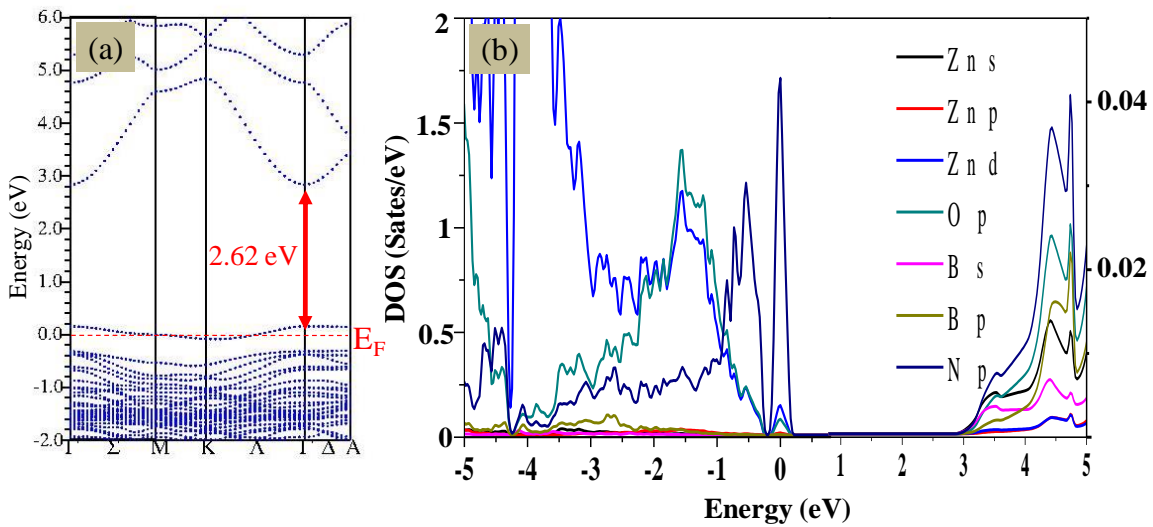


Figure 7.4. (a) Band structure and (b) density of states of BN₂:ZnO. (Copyright (2015) by Wiley [3]).

7.3 Summary of the thesis

We have successfully used HR-EELS for obtaining both direct and indirect optical band gaps at nanoscale from A-site cation vacancy regions, deviations from ideal inverse spinel configurations and the effect of magnetic order on optical band gaps in various magnetic spinel oxide systems.

For MoS₂ and ReS₂, layer specific band gap measurement has been performed. Twin exciton peak as well as direct to indirect cross-over has been observed for monolayer MoS₂.

We also have learnt from our experience that low-loss EELS/optical band gap measurement is a much more sensitive and effective tool to identify the types of various point defects and related complexes in ZnO when compared to core-loss EELS/ELNES, which is the technique of first choice.

Also, so far we could incorporate 17 at. % S in ZnO as single phase epitaxial thin film which gives a valence band shift of ~0.2 eV. We also found that Ag and Li are ‘not good dopants’ but *off-stoichiometric* BN_{1+x} is found to be a good dopant and resulted in *p*-conductivity in ZnO.

Further work needs to be focused on valence band engineering along with *off-stoichiometric* BN *co-doping* in order to improve the carrier concentration and mobility to fabricate any device.

7.4 Bibliography

- [1] O. L. Krivanek, T. C. Lovejoy, N. Dellby, and R. W. Carpenter, *Microscopy* **62**, 3 (2013).
- [2] O. L. Krivanek, T. C. Lovejoy, N. Dellby, T. Aoki, R. W. Carpenter, P. Rez, E. Soignard, J. Zhu, P. E. Batson, M. J. Lagos, R. F. Egerton, P. A. Crozier, *Nature* **514**, 209 (2014).
- [3] R. Sahu, H. B. Gholap, G. Mounika, K. Dileep, B. Vishal, S. Ghara, and R. Datta, *Phys. Status Solidi B*, 1–5 (2015)/ DOI 10.1002/pssb.201552625.